อิทธิพลของพารามิเตอร์การปลูกผลึกต่อคุณสมบัติเชิงโครงสร้างและเชิงแสงของโครงสร้างนาโนชนิดแกลเลียมแอนติโมไนด์ที่ปลูกด้วยวิธีดรอปเล็ทอิพิแทกซี

นายเมธี คุณรักษา

วิทยานิพนธ์นี้เป็นส่วนหนึ่งของการศึกษาตามหลักสูตรปริญญาวิศวกรรมศาสตรดุษฎีบัณฑิต
สาขาวิชาวิศวกรรมไฟฟ้า ภาควิชาวิศวกรรมไฟฟ้า
คณะวิศวกรรมศาสตร์ จุฬาลงกรณ์มหาวิทยาลัย
ปีการศึกษา 2557

EFFECT OF GROWTH PARAMETERS ON STRUCTURAL AND OPTICAL PROPERTIES OF GALLIUM ANTIMONIDE NANOSTRUCTURES GROWN BY DROPLET EPITAXY

Mr. Maetee Kunrugsa

A Dissertation Submitted in Partial Fulfillment of the Requirements
for the Degree of Doctor of Philosophy Program in Electrical Engineering
Department of Electrical Engineering
Faculty of Engineering
Chulalongkorn University
Academic Year 2014

Thesis Title	EFFECT OF GROWTH PARAMETERS ON STRUCTURAL AND OPTICAL PROPERTIES OF GALLIUM ANTIMONIDE NANOSTRUCTURES GROWN BY DROPLET EPITAXY
By	Mr. Maetee Kunrugsa
Field of Study	Electrical Engineering
Thesis Advisor	Associate Professor Somchai Ratanathammaphan, D.Eng.
Thesis Co-Advisor	Chantal Fontaine, Ph.D.

Accepted by the Faculty of Engineering, Chulalongkorn University in Partial Fulfillment of the Requirements for the Doctoral Degree

....Dean of the Faculty of Engineering
(Professor Bundhit Eua-arporn, Ph.D.)

THESIS COMMITTEE
....Chairman
(Associate Professor Banyong Toprasertpong, Dr.Ing.)
....Thesis Advisor
(Associate Professor Somchai Ratanathammaphan, D.Eng.)
....Thesis Co-Advisor
(Chantal Fontaine, Ph.D.)
....Examiner
(Professor Somsak Panyakaew, D.Eng.)
....Examiner
(Chanin Wissawinthanon, Ph.D.)
....External Examiner
(Associate Professor Choompol Antarasena, Dr.Ing.)

เมธี คุณรักษา : อิทธิพลของพารามิเตอร์การปลูกผลึกต่อคุณสมบัติเชิงโครงสร้างและเชิงแสงของโครงสร้างนาโนชนิดแกลเลียมแอนติโมไนด์ที่ปลูกด้วยวิธีดรอปเล็ทอิพิแทกซี (EFFECT OF GROWTH PARAMETERS ON STRUCTURAL AND OPTICAL PROPERTIES OF GALLIUM ANTIMONIDE NANOSTRUCTURES GROWN BY DROPLET EPITAXY) อ.ที่ปรึกษาวิทยานิพนธ์หลัก: รศ. ดร.สมชัย รัตนธรรมพันธ์, อ.ที่ปรึกษาวิทยานิพนธ์ร่วม: ดร.ชองทาล ฟงเทน, 107 หน้า.

วิทยานิพนธ์ฉบับนี้มุ่งเน้นไปที่การศึกษาอิทธิพลของพารามิเตอร์การปลูกผลึกต่อคุณสมบัติเชิงโครงสร้าง และเชิงแสงของโครงสร้างนาโนชนิดแกลเลียมแอนติโมไนด์ที่ปลูกด้วยวิธีดรอปเล็ทอิพิแทกซีบนแผ่นฐานแกลเลียมอาร์เซไนด์ (001) รูปร่างของโครงสร้างนาโนถูกตรวจสอบด้วยกล้องจุลทรรศน์แรงอะตอม ส่วนคุณสมบัติเชิงแสงของโครงสร้างนาโนชนิดแกลเลียมแอนติโมไนด์ที่ฝังอยู่ในเมตริกซ์แกลเลียมอาร์เซไนด์ถูกตรวจสอบด้วยการวัดโฟโตลูมิเนสเซนซ์ ซึ่งทำให้ทราบถึงพลวัตของพาหะ และลักษณะเฉพาะของการเรียงตัวของแถบพลังงานแบบ type II ในแง่ของการปลูกผลึก เนื่องจากขีดจำกัดทางเทคนิคของแหล่งกำเนิดลำโมเลกุลของแอนติโมนีที่ให้ความเข้มฟลักซ์ค่อนข้างต่ำ ดังนั้น โครงสร้างนาโนชนิดแกลเลียมแอนติโมไนด์ที่ได้ส่วนใหญ่จึงมีลักษณะเป็นวงแหวน เพราะว่าอะตอมแกลเลียมสามารถแพร่ออกจากหยดแกลเลียมเหลวได้ วิทยานิพนธ์ฉบับนี้ยังได้กล่าวถึงการติดตามวิวัฒนาการของหยดแกลเลียมเหลวในกระบวนการทำให้เป็นผลึกด้วยลำโมเลกุลของแอนติโมนีจนกระทั่งกลายเป็นโครงสร้างควอนตัมริงชนิดแกลเลียมแอนติโมไนด์ นอกจากโครงสร้างควอนตัมริงแล้ว โครงสร้างควอนตัมดอตชนิดแกลเลียมแอนติโมไนด์มีแนวโน้มที่จะเกิดขึ้นเมื่อเพิ่มปริมาณแกลเลียม โครงสร้างควอนตัมริงที่ถูกล้อมรอบด้วยควอนตัมดอตโมเลกุลที่เรียงตัวเป็นวงแหวนสามารถก่อตัวขึ้นได้เมื่อใช้อัตราการพ่นแกลเลียมและอุณหภูมิการทำให้เป็นผลึกที่เหมาะสม การเพิ่มอุณหภูมิในขณะขึ้นรูปหยดแกลเลียมเหลวส่งผลให้เกิดโครงสร้างที่มีทั้งควอนตัมริงและควอนตัมดอตอยู่ด้วยกัน แบบจำลองอย่างง่ายจึงถูกนำเสนอเพื่ออธิบายกลไกการก่อตัวของโครงสร้างนาโนเหล่านี้ให้ชัดเจนยิ่งขึ้น ความเครียดอันเกิดจากความแตกต่างของค่าคงตัวผลึกระหว่างแกลเลียมแอนติโมไนด์และแกลเลียมอาร์เซไนด์ ยังเข้ามามีบทบาทสำคัญต่อรูปร่างของโครงสร้างนาโนด้วย โครงสร้างนาโนชนิดแกลเลียมแอนติโมไนด์ที่ปลูกด้วยวิธีดรอปเล็ทอิพิแทกซีมักก่อตัวขึ้นพร้อมกับชั้นผลึกแกลเลียมแอนติโมไนด์ ซึ่งทำหน้าที่เป็นช่องทางการถ่ายโอนพาหะระหว่างโครงสร้างนาโน และทำให้ความสามารถในการกักโฮลของโครงสร้างนาโนชนิดแกลเลียมแอนติโมไนด์ลดลง อย่างไรก็ตาม การปลูกโครงสร้างควอนตัมริงชนิดแกลเลียมแอนติโมไนด์ที่ปราศจากชั้นผลึกแกลเลียมแอนติโมไนด์ สามารถทำได้โดยการใช้อุณหภูมิการทำให้เป็นผลึกที่ต่ำมาก

ภาควิชา วิศวกรรมไฟฟ้า
สาขาวิชา วิศวกรรมไฟฟ้า
ปีการศึกษา 2557

ลายมือชื่อนิสิต ....
ลายมือชื่อ อ.ที่ปรึกษาหลัก ....
ลายมือชื่อ อ.ที่ปรึกษาร่วม ....

5471435821 : MAJOR ELECTRICAL ENGINEERING

KEYWORDS: GALLIUM ANTIMONIDE / NANOSTRUCTURES / MOLECULAR BEAM EPITAXY / DROPLET EPITAXY / PHOTOLUMINESCENCE

MAETEE KUNRUGSA: EFFECT OF GROWTH PARAMETERS ON STRUCTURAL AND OPTICAL PROPERTIES OF GALLIUM ANTIMONIDE NANOSTRUCTURES GROWN BY DROPLET EPITAXY. ADVISOR: ASSOC. PROF. SOMCHAI RATANATHAMMAPHAN, D.Eng., CO-ADVISOR: CHANTAL FONTAINE, Ph.D., 107 pp.

This dissertation is dedicated to the intensive study of the effect of growth parameters on structural and optical properties of GaSb nanostructures grown by droplet epitaxy on GaAs (001) substrates. The nanostructure morphology is investigated by atomic force microscopy. Photoluminescence measurements are employed for the optical characterization of GaSb nanostructures buried in the GaAs matrix, and provide a lot of information about the carrier dynamics and the signatures of type-II band alignment. As a consequence of a technical limit of equipment, Sb flux intensity can be adjusted only in the low regime. Most of the obtained GaSb nanostructures are therefore ring-shaped due to the outward diffusion of Ga atoms from the Ga droplets. The tracking of the evolution of Ga droplets into GaSb quantum rings is included in this dissertation. Apart from the quantum rings, GaSb quantum dots tend to take place at high Ga amounts. The quantum ring surrounded by ring-shaped quantum dot molecules can be observed for some proper Ga deposition rate and crystallization temperature. Increasing the Ga deposition temperature results in the appearance of quantum ring-with-dot structures. Simple descriptive models are proposed to elucidate the formation mechanisms of such nanostructures. Strain caused by a lattice mismatch between GaSb and GaAs also plays a role in the shape derivation. For droplet epitaxy, the GaSb nanostructures are often formed along with a GaSb layer which acts as a carrier transfer channel between the nanostructures and thus degrades the hole confinement ability of the GaSb nanostructures. However, the growth of GaSb quantum rings without the GaSb layer is demonstrated by applying very low crystallization temperature.

Department:	Electrical Engineering	Student's Signature	....
Field of Study:	Electrical Engineering	Advisor's Signature	....
Academic Year:	2014	Co-Advisor's Signature	....

ACKNOWLEDGEMENTS

My dissertation would not have been done without the intense encouragement from my parents all the time. Words cannot express my gratitude to them. My sincere thanks go to my advisor, Assoc. Prof. Dr. Somchai Ratanathammaphan, as well as my co-advisor, Dr. Chantal Fontaine, for their tremendous suggestions. I am deeply grateful to Dr. Poonyasiri Boonpeng and Asst. Prof. Dr. Suwit Kiravittaya for giving me a lot of knowledge and enlightening me when I encountered the problems. It seems that there are a number of unpredictable things in my research. One of those is that I met Dr. Kar Hoo Patrick Tung by chance at the 7th International Conference on Materials for Advanced Technologies (ICMAT 2013). Latterly, he helped me to perform the photoluminescence measurement, and the results became the backbone of my dissertation. His benevolence will be everlastingly remembered. Prof. Dr. Somsak Panyakaew, Assoc. Prof. Dr. Banyong Toprasertpong, Assoc. Prof. Dr. Choompol Antarasena, and Dr. Chanin Wissawinthanon are kindly acknowledged as the dissertation committee members. Furthermore, I would like to give special thanks to the Semiconductor Device Research Laboratory (SDRL) staff, and my great collaborators, in particular Ms. Patchareewan Prongjit, Ms. Kamonchanok Khoklang, and Ms. Nattapa Prapasawad, for their assistance and making my serious research become enjoyable. My dissertation could not be successful without the financial support from Thailand Research Fund through the Royal Golden Jubilee Ph.D. Program (Grant no. PHD/0026/2554), Thailand Research Fund (DPG5380002), National Nanotechnology Center (NANOTEC), Higher Education Research Promotion and National Research University Project of Thailand, Office of the Higher Education Commission (EN264A), Ratchadaphiseksomphot Endowment Fund of Chulalongkorn University (RES560530079-EN), and Asian Office of Aerospace Research and Development (FA2386-14-1-4081). Finally, I would like to thank myself that has been strong enough to do the experiments for a long time and firmly believed in everything I do.

CONTENTS

Chapter 1

Introduction

1.1 Background and motivation

It is generally known that charge carriers (electrons and/or holes) in bulk semiconductors can move in all three spatial dimensions and behave like the free particles which their energy levels and density of states are continuous. If any of the structural dimensions is squeezed to be comparable to the de Broglie wavelength of the carrier or the exciton Bohr radius, the motion of charge carriers becomes restricted in the corresponding direction, leading to the quantum confinement effect at which the carrier energy levels and density of states are decided by the structural size. Therefore, the electronic and optical properties are entirely different from the bulks. This is a starting point of the study of low-dimensional structures or nanostructures. The low-dimensional structures are often categorized by the confinement dimension into three types: one-, two-, and three-dimensional confinements which are referred to quantum well (QW), quantum wire (QWR), and quantum dot (QD), respectively. In addition to these structures, quantum ring (QR) is a kind of nanostructure with three-dimensional confinement. Unlike the QD, the ground state energy of a carrier moving along the QR becomes periodic when a magnetic flux threads the inner part of the QR. This is called Aharonov-Bohm type oscillations. Such a periodic ground state energy also gives rise to a persistent current [1].

III-V compound semiconductor nanostructures have been of interest for a long time not only in the fundamental physics but also in the novel applications. According to the three-dimensional confinement of the QDs, the delta-like density of states and discrete energy levels for the carriers are obtained. For this reason, QDs can be seen as artificial atoms. With such unique properties, the integration of QDs into semiconductor devices can improve the performance, for instance, low-threshold-current QD lasers [2] and long-storage-time QD flash memories [3]. Semiconductor nanostructures can be fabricated by top-down and bottom-up approaches. The top-down approach is based on micro- and nanofabrication technologies such as chemical etching, lithography, and ion beam milling. Although the controllable size and arrangement can be achieved, the nanostructures produced by this method frequently contain defects and contaminants due to the fabrication process, degrading the device performance. To overcome these limitations, the bottom-up approach or self-assembly which utilizes the epitaxial growth techniques has been introduced as an efficient way to create the nanostructures. Self-assembled nanostructures contain very low defect density or even no defects, resulting in good electronic, electrical, and optical properties. That is why the self-assembled nanostructures gain more attraction from new generation applications in optoelectronic devices and quantum information technologies.

Stranski-Krastanov (SK) method is a well-known self-assembly technique for the growth of semiconductor nanostructures, in particular QDs. Nevertheless, the compressive strain from a lattice mismatch between an epitaxial layer and a substrate is required for the self-assembled QDs grown by the SK method since the QD formation relies on strain-driven mechanisms. This is a significant limitation of the SK method. Droplet epitaxy which is an alternative method is therefore proposed to extend the self-assembly approach to the lattice-matched systems in addition to the lattice-mismatched ones [4]. In general, droplet epitaxy consists of two steps: the formation of liquid metallic droplets by irradiating group-III element(s) on the substrate, and the supply of group-V element(s) in order to crystallize such droplets into the III-V nanostructures. The difference between the SK method and droplet epitaxy is the sequence of the deposition of group-III and group-V elements, i.e., group-III and group-V elements are simultaneously deposited in the SK method, whereas group-III element(s) is deposited prior to group-V element(s) for droplet epitaxy. Consequently, droplet epitaxy can be applied to both lattice-matched and lattice-mismatched systems because the strain is not necessary. Droplet epitaxy also offers high degree of freedom to engineer the feature and density of nanostructures via the variations of the growth parameters such as deposition rate of group-III element(s), group-V flux intensity, and substrate temperature. It is worth pointing out that the strain occurring during crystallization in the case of lattice-mismatched droplet epitaxy should be taken into account as it affects the morphology of nanostructures and their electronic structures.

Among various semiconductor nanostructures, GaSb/GaAs nanostructures have drawn much attention over the past few decades due to the staggered type-II band alignment. For GaSb nanostructures in a GaAs matrix, holes are strongly localized in the GaSb region, while electrons in the GaAs matrix reside around the GaSb/GaAs interface via the Coulomb attraction. GaSb/GaAs QDs grown by the SK method have been extensively studied [5-7]. Since a spatial separation between electron and hole wave functions results in a low transition probability and decreases the carrier recombination rate, the GaSb/GaAs QDs are suitable for solar cells [8] and high-operating-temperature infrared photodetectors [9]. The large hole confinement potential of 450 meV makes the GaSb/GaAs QDs promising for memory devices with long storage time [10]. Even these intrinsic properties hinder the realization of light sources, the photoluminescence (PL) and electroluminescence (EL) from the GaSb/GaAs QDs can be observed at room temperature by performing the long Sb exposure after the QD growth. Also, the light-emitting diodes and lasers have been demonstrated [11, 12]. To enhance the light emission efficiency, GaSb/GaAs QRs which have more surface area for radiative recombination than the QDs [9] are utilized. In addition, the QRs contain fewer defects and less strain than the QDs [13]. According to these merits, multi-stacked QR solar cells can be grown without the need of strain compensation [14]. Apart from the application point of view, the GaSb/GaAs QRs feature in the fundamental physics. For instance, they are a good candidate for the observation of strong optical exciton Aharov-Bohm effect, i.e., an oscillatory component in the energy of the optically active states [15].

The fabrication of self-assembled GaSb/GaAs QRs is usually based on the growth of GaSb/GaAs QDs by the SK method, and followed by soaking with a proper Sb/As ratio [9] or capping with a GaAs layer [16]. An As-for-Sb exchange reaction is responsible for the QD-to-QR transition. However, the QD/QR mixture might appear because such a transition is not a spontaneous process [17]. It has been found that the GaSb/GaAs QRs can be spontaneously formed by molecular beam epitaxy with an unusual growth procedure as a consequence of the wetting layer instability [18]. Furthermore, the utilization of a partial-capping-and-regrowth technique is another way to obtain the QRs [19]. It is evident that such methods require the additional process and the specific conditions. Droplet epitaxy which is a simple and flexible method is thus introduced in the GaSb/GaAs system. For this method, the GaSb/GaAs nanostructures are achieved by the incorporation of Sb atoms into the liquid Ga droplets which are primarily deposited on the GaAs surface. According to droplet epitaxy, various kinds of self-assembled GaSb/GaAs nanostructures should have been reported. In fact, the QDs are mostly studied [20-23], whereas there are very few works on the QRs [24]. It is worth remembering that the low growth temperature is required for droplet epitaxy in order to avoid the desorption of the droplets. At low temperature, the Sb atoms supplied to the growth surface can condense in a form of a polycrystalline granular layer [20]. Hence, the critical factors in the crystallization process are substrate temperature, Sb flux intensity, and crystallization time. Besides, the compressive strain caused by the lattice mismatch between GaSb and GaAs may give rise to some deviations of nanostructure morphology from the expectations. From these issues, it is clear that there is more room for tailoring the properties of GaSb/GaAs nanostructures grown by droplet epitaxy through the growth conditions to satisfy the requirements for the scientific studies or the promising applications.

1.2 Objectives and limitations

It is generally accepted that the properties of self-assembled nanostructures strongly depend on the growth conditions which determine morphology, density, and composition of the nanostructures. As aforementioned, droplet epitaxy provides many possibilities for the fabrication of a variety of III-V compound nanostructures, and the better understanding of type-II GaSb/GaAs nanostructures is still needed. The investigation of the effect of growth parameters on the structural and optical properties of the GaSb/GaAs nanostructures grown by droplet epitaxy is therefore the main objective of this dissertation. There are several growth parameters studied here such as crystallization time, Ga amount, Ga deposition rate, and substrate temperature. Nevertheless, the Sb flux intensity cannot be adjusted over a wide range and seems to be limited up to ~10^{-6} Torr owing to a technical limit of a valved-cracker cell. The self-assembled GaSb nanostructures are grown on the GaAs (001) substrates by droplet epitaxy using solid-source molecular beam epitaxy (MBE). The evolution of Ga droplets during crystallization with the Sb flux is tracked by reflection high energy electron diffraction (RHEED) to find the proper crystallization time such that the Ga droplets are completely crystallized into the GaSb nanostructures without the formation of polycrystalline granular Sb layer. Atomic force microscopy (AFM) is employed to examine the morphology of GaSb/GaAs nanostructures. The optical properties of the GaSb nanostructures embedded in the GaAs matrix are characterized by photoluminescence (PL) spectroscopy. The temperature- and power-dependent PL measurements are performed to study the carrier behavior and the ability of hole confinement in the GaSb nanostructures. Moreover, the simple models are proposed to describe some experimental results.

1.3 Overview

The significance of semiconductor nanostructures and the fabrication methods have just been discussed in the first part of Chapter 1, and followed by the motivation for the study of the type-II GaSb/GaAs nanostructures grown by droplet epitaxy. The objectives of this dissertation and the constraints on the experiments have just been given as well. Before doing any research, the fundamental knowledge, including the literature reviews, is very important. The concepts of MBE and droplet epitaxy, and the relevant physics in epitaxial growth, such as atomistic processes and growth modes, are therefore summarized in Chapter 2. The origin and interpretation of RHEED patterns, low-dimensional structures, PL spectroscopy, and a short review on the GaSb/GaAs nanostructures are also mentioned. The typical experimental procedures and the necessary equipment are presented in Chapter 3. To make various contents in this dissertation easier to understand, the details of each experiment are described together with the results and discussion.

According to the limitation on the Sb flux intensity which is rather low, it is possible to grow the GaSb/GaAs QRs. Meanwhile, the crystallization time is a crucial factor. Chapter 4 is thus devoted to the evolution of Ga droplets into GaSb QRs. Such evolution can be tracked by crystallizing the droplets with different durations. The minimum crystallization time required for the QR formation can be found from this experiment. Once the GaSb/GaAs QRs are achieved by droplet epitaxy, their optical properties which can be obtained from the PL measurement become more interested as they can prove the crystal quality and display some characteristics of the type-II band alignment. These are the keynote of Chapter 5.

The influences of growth parameters (e.g., Ga amount, Ga deposition rate, and temperatures for droplet formation and crystallization) on the structural and optical properties of the GaSb/GaAs nanostructures are thoroughly discussed in Chapters 6-9. Many kinds of GaSb/GaAs nanostructures are formed by adjusting these fundamental growth parameters. The descriptive models based on the diffusion process are suggested to explain the formation mechanisms. The PL measurement reveals a lot of relevant information about the optical properties and the carrier dynamics in such type-II nanostructures. The essential results and discussion with some comments are concluded in Chapter 10.

Chapter 2

Fundamental knowledge

This chapter is devoted to the fundamental knowledge necessary for doing the experiments and analyzing the results. The concept of molecular beam epitaxy (MBE) is summarized, and followed by the explanation of the atomistic processes in epitaxial growth and the growth modes. Since the reflection high energy electron diffraction (RHEED) is an important tool for the real-time surface investigation during the MBE growth, the origin of RHEED patterns and how to interpret the patterns are needed. The perception of droplet epitaxy is very significant because it is the growth method for self-assembled GaSb/GaAs nanostructures studied here. The energy levels and the density of states in low-dimensional structures are concisely described. As the photoluminescence (PL) spectroscopy is the optical characterization technique employed in this dissertation, the understanding of the PL emission including the effects of temperature and excitation power on the PL results is needed. A short review of some interesting topics in GaSb/GaAs nanostructures is provided in the last section.

2.1 Basics of molecular beam epitaxy

Molecular beam epitaxy (MBE) is an epitaxial growth technique based on the reaction of atomic or molecular beams of constituent elements on a substrate surface heated at necessary temperature in ultra-high vacuum (UHV) environment. The following explanations are concentrated on a solid-source MBE which was used to grow every sample in this work. An illustration of a general MBE growth chamber is shown in Figure 2.1. The molecular beams are produced by the effusion (Knudsen) cells or valved-cracker cells through the evaporation or sublimation of solid-source materials. These cells are placed in the position and angle such that the good uniformity of beams on the substrate can be provided. Moreover, the continuous rotation of substrate can improve the growth homogeneity. The beam flux is switched on and off by a mechanical shutter or valve situated in front of the source. Therefore, the composition and doping profiles can be abruptly changed. Due to the UHV environment, it is possible to install *in-situ* characterization tools such as a reflection high energy electron diffraction (RHEED) system for investigating the real-time phenomena on the substrate surface during the growth, and a quadrupole mass spectrometer (QMS) for monitoring the molecular species in the growth chamber.

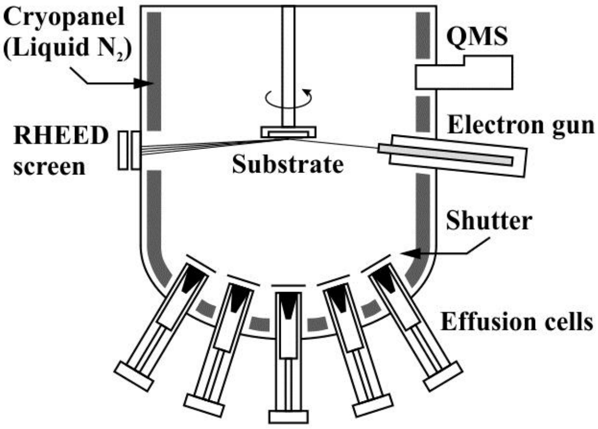

Figure 2.1 Illustration of a typical MBE growth chamber.

The mean free path of a particle (atom or molecule) evaporated from the source must be larger than the distance from source to substrate, which is in a range of 5-30 cm. If the background pressure of the growth chamber is not low enough, the particles in the beam may be scattered by undesirable gas species, leading to the fluctuation of beam direction and flux intensity. Based on the kinetic theory of gases, the mean free path is calculated by

$$\Lambda = \frac{k_B T}{\sqrt{2}\pi d^2 P_s} \tag{2.1}$$

where k_B is the Boltzmann constant, T is the temperature, d is the particle diameter, and P_s is the equilibrium vapor pressure of the source. Since a typical value of the particle diameter is 2-5 Å, the mean free path is ~10 m at a pressure of 10^{-5} Torr which can be approximated to be a pressure limit for MBE growth. Thus, the background pressure is even more critical and affects the purity of sample.

The maximum flux F_m coming from a source having a surface area A_s per unit time is given by

$$F_m = A_s P_s \left(\frac{N_A}{2\pi M k_B T} \right)^{1/2} \tag{2.2}$$

where N_A is Avogadro's number, and M is the molecular weight. Given that the distance from source to substrate is r_s and the angle between the beam axis and the normal to the substrate is φ, then the flux impinging on the substrate can be obtained by

$$F = \frac{F_m \cos\varphi}{\pi r_s^2} \tag{2.3}$$

In general, the incoming flux delivers 10^{15}-10^{16} cm^{-2}s^{-1} corresponding to a growth rate in the order of one monolayer per second which is low enough for surface migration of the incoming species, resulting in the atomically smooth epitaxial layer. In respect of purity, the time which the surface takes to be covered by one monolayer of residual species must be much less than the time for the formation of one monolayer by the beam flux. For example, if the residual species is CO and one monolayer consists of 10^{15} atoms, it takes ~7.3 h to form one monolayer in 10^{-10} Torr at 300 K, while it takes a few seconds in the case of the beam flux. Consequently, to ensure the purity of epitaxial layer, the background pressure must be in the order of 10^{-10} Torr. Another consideration is a sticking coefficient. Fortunately, the sticking coefficient of typical residual gas species is much less than unity and most semiconductor surfaces are relatively unreactive with residual species. Hence, the UHV condition is not so stringent at ~10^{-10} Torr. The background pressure range of 10^{-9}-10^{-8} Torr is acceptable.

2.2 Atomistic processes in epitaxial growth

For the MBE growth of semiconductors, the constituent elements in effusion cells or valved-cracker cells are heated until they evaporate or sublimate with desired flux intensity. After opening the shutters or valves, such atoms or molecules in the beams impinge on the substrate surface which is heated to several hundred degrees Celsius to avoid the formation of polycrystalline or amorphous layer owing to a low mobility of adatoms. Even it is very simple in concept, there are many atomistic processes involved during the growth.

As the molecular beam is in the vapor phase but the substrate is in the solid phase, atoms or molecules in the beam have to condense over the substrate. At certain temperature, there is an equilibrium vapor pressure. The nucleation occurs on the condition that the partial pressure of beams P_0 exceeds the equilibrium vapor pressure P_∞ over the solid phase. This condition is called supersaturation, defined by $s = P_0 / P_\infty$. The supersaturation is generally achieved just above the substrate surface.

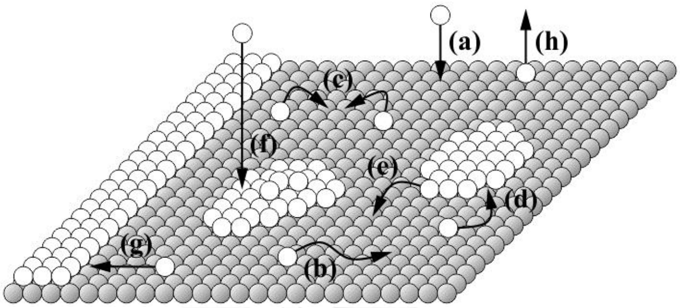

Figure 2.2 Atomistic processes during epitaxial growth.

Typical processes occurring on the substrate during the epitaxial growth are depicted in Figure 2.2. Atoms from the molecular beam are deposited on a crystalline substrate surface (a). The atoms adsorb on the surface and become adatoms with adsorption energy E_a. Such adatoms can diffuse across the surface (b) if an activation energy for diffusion E_d is overcome. When adatoms meet each other (c), they form the cluster which can either grow to a stable cluster by attachment of additional adatoms (d) or decay by detachment of atoms (e). The impingement of atoms on islands (f) should be also considered. Moreover, the adatoms may be incorporated into a step (g) or desorbed (re-evaporated) from the surface (h) by obtaining energy which is equal to E_e. Since E_d is much smaller than E_e, the surface diffusion is far more likely than the desorption. Nonetheless, the latter is dominant at high temperatures.

In thermodynamic equilibrium, all atomistic processes are equilibrated by their reverse processes with equal rates. This is the concept of detailed balance. For instance, the rates of condensation and desorption must be equal, and decay of clusters must occur with the same rate as they grow. Hence, there is no net growth and macroscopic quantities, such as surface coverage and roughness, do not change in average, while microscopic processes like atomistic processes continuously change and cause the fluctuations around the equilibrium quantities. It implies that the epitaxial growth is far away from thermodynamic equilibrium. In fact, the epitaxial growth is a non-equilibrium kinetic phenomenon. However, not all processes are limited by kinetics because some process may be in the local thermodynamic equilibrium. A parameter used to distinguish between thermodynamic and kinetic regimes is the ratio of the diffusion rate D to the deposition or incorporation rate F [25]. If the D/F ratio is large, the growth is in the thermodynamic regime where adatoms have time to find the nucleation sites so that the total energy of the system is minimized. On the other hand, if the D/F ratio is small, the growth is in the kinetic regime where the individual processes leading to metastable structures become more significant. It is worth noticing that the MBE growth of semiconductor nanostructures lies between these two regimes (i.e., the intermediate D/F ratio), meaning that both thermodynamics and kinetics play a role in the determination of their morphology at the same time.

During the nucleation stage, the adatoms diffusing on the surface may encounter with other adatoms and form a cluster which either grows or decays. The cluster which has the same probabilities to grow and decay is called a critical cluster. If the critical cluster size contains i atoms, the cluster containing more than i atoms is stable, which is called a stable cluster. On the contrary, the cluster containing less than i atoms, which is called a subcritical cluster, is unstable. The unstable clusters can reduce the total energy of the system by shrinking, whereas the stable clusters can reduce the total energy of the system by growing to be larger clusters.

According to the nucleation theory [26], the maximum or saturation density of stable clusters can be expressed by $n_x \propto (F/v)^p \exp(E_x/k_B T)$ where F is the deposition rate, v is the atomic vibration frequency, p is the value depending on the number of atoms in a critical cluster i, E_x is the energy related to the atomistic processes, k_B is the Boltzmann constant, and T is the temperature. The binding energy E_i of the critical cluster, the activation energy for surface diffusion E_d, and the adsorption energy E_a contribute to the energy term E_x. The values of p and E_x displayed in Table 2.1 correspond to the dominant atomistic process relying on the condensation regime [27]. The direct deposition is important in the extremely incomplete condensation regime, while the desorption is negligible in the complete condensation regime. Between these two regimes, there is an initially incomplete regime where the diffusive capture dominates primarily.

Table 2.1 Values of p and E_x at different condensation regimes for three-dimensional (3D) and two-dimensional (2D) islands.

Regime	**3D islands**	**2D islands**
Extremely incomplete	$p = 2i/3$ $E_x = (2/3)[E_i + (i+1)E_a - E_d]$	$p = i$ $E_x = E_i + (i+1)E_a - E_d$
Initially incomplete	$p = 2i/5$ $E_x = (2/5)(E_i + iE_a)$	$p = i/2$ $E_x = (1/2)(E_i + iE_a)$
Complete	$p = i/(i+2.5)$ $E_x = (E_i + iE_d)/(i+2.5)$	$p = i/(i+2)$ $E_x = (E_i + iE_d)/(i+2)$

It is worth pointing out that the maximum cluster density follows a power law on the deposition rate and exponentially depends on the substrate temperature. Therefore, the density of stable clusters and self-assembled nanostructures grown by MBE can be controlled by fundamental growth parameters such as the deposition rate and the substrate temperature. For the complete condensation regime, since $D \propto \exp(-E_d / k_B T)$ if the activation energy for diffusion (E_d) is only considered, the maximum cluster density (n_x) can be simplified by a lumped parameter (D/F) and is proportional to $(D/F)^{-p}$ where $p = i/(i+2)$ for 2D islands and $p = i/(i+2.5)$ for 3D islands [28].

2.3 Growth modes

There are five growth modes which are most frequently found in epitaxy: Frank-van der Merwe (FM) mode, Volmer-Weber (VW) mode, Stranski-Krastanov (SK) mode, step-flow (SF) mode, and columnar-growth (CG) mode. These growth modes are illustrated in Figure 2.3.

The FM mode happens if atoms or molecules of deposited material are more strongly bound to the substrate than to each other. When the first monolayer is completely formed on the substrate, it will be covered by the loosely bound second layer which provides a decrease in binding strength towards a value for bulk deposited material. As a result, the layer-by-layer growth is obtained. The FM mode is commonly referred to the two-dimensional (2D) growth mode. In contrast to the FM mode, the VW mode is achieved when atoms or molecules of deposited material are more strongly bound to each other than to the substrate, resulting in the isolated islands on the surface. If the deposited material is further supplied, such islands grow and finally coalesce, giving rise to a rough surface with root-mean-square (rms) roughness comparable to the average distance between islands. The VW mode is also known as the three-dimensional (3D) or island growth mode.

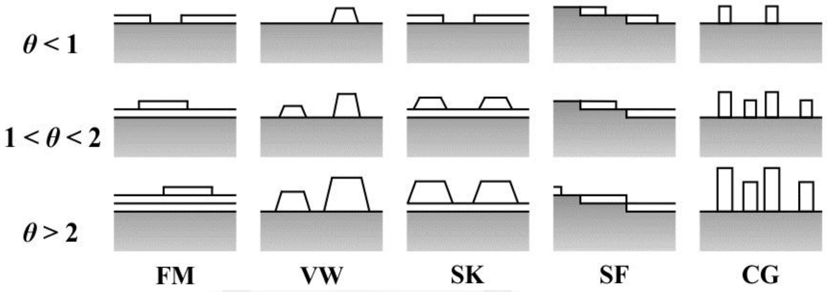

Figure 2.3 Growth modes in epitaxial growth. θ is the deposited material coverage in a unit of monolayer (ML).

According to the thermodynamic model [29], the epitaxial growth mode is governed by the surface and interfacial free energies for epitaxial layer and substrate. Suppose that γ_e and γ_s are the surface free energies of an epitaxial layer and a substrate, respectively, and γ_i is the epitaxial layer-substrate interfacial free energy. The growth mode is determined by the areal change in the free energies related to the epitaxial layer coverage, and defined by $\gamma_{net} = \gamma_e + \gamma_i - \gamma_s$. The FM mode appears if $\gamma_{net} < 0,$ while $\gamma_{net} > 0$ is required for the VW mode.

The SK mode is a combination of the FM and VW modes. The initial growth of a few monolayers proceeds in a layer-by-layer manner which is called a wetting layer. The islands are subsequently formed on top of the wetting layer after exceeding a certain critical thickness. That is why the SK mode is known as a layer-plus-island mode. The SK mode requires the condition that the deposited material has a lattice constant a bit larger than the substrate because the compressive strain is important for the formation of islands. Below the critical thickness, the thermodynamic condition for layer-by-layer growth is still satisfied. Nevertheless, the compressive strain due to the lattice mismatch proportionally increases with the deposited material coverage. When the coverage is more than the critical thickness, it becomes energetically favorable for the island formation to reduce the strain energy at the cost of the surface energy such that the minimization of total energy is achieved. The SK mode plays a crucial role in the fabrication of self-assembled semiconductor nanostructures, in particular quantum dots.

It is worth keeping in mind that in the FM mode, the first monolayer must be completed before the nucleation of a new one, and there is no wetting layer formed in the VW mode. In addition to above considerations, the strain and the surface chemistry are often used to predict the favorable mode. As a matter of fact, the FM mode prefers the system having no strain, whereas the VW mode tends to take place in the highly lattice-mismatched system. The SK mode can be found in the system possessing small strain. The appearance of 3D islands is a result of a reduction in strain energy in both in-plane and out-of-plane directions at the expense of surface energy such that the total energy of the system is minimized. However, the island formation is not the only way to reduce the strain. Meanwhile, the dislocations might be introduced. For this reason, there is the competition between these two phenomena. The surface chemistry also affects the epitaxial layer. A clear example is the growth of a polar material on a non-polar substrate such as the growth of GaAs on Ge substrate. Although the lattice constants of GaAs and Ge are nearly the same, the anti-phase domain which is a kind of crystallographic defect can be observed.

For a vicinal (tilted) substrate where the surface consists of a number of flat terraces separated by atomic steps, the growth will proceed by the advancement of steps if the substrate temperature is high or the deposition flux is low enough for the incorporation of adatoms into the step edges. Consequently, the epitaxial layer has the same smoothness as the starting substrate. Such a growth situates in the SF mode. The advantage of step-flow growth is an improvement of crystal quality by the suppression of island formation. Nonetheless, the epitaxial layer may grow on the terraces in the FM or SK modes if the substrate temperature is too low or the deposition flux is too high to prohibit the adatom diffusion.

The CG mode occurs in some cases where the surface diffusion is extremely low, resulting in the film containing a number of columns of deposited material. Interestingly, such columns have well-defined boundaries, i.e., each column does not merge with others. This is different from the VW and SK modes where the islands coalesce and eventually cover the entire substrate surface when the coverage of deposited material increases.

The growth mode may be altered by the introduction of surfactants. The surfactants can modify the thermodynamic factors such as the surface energies of epitaxial layer and/or substrate, as well as the kinetic factors such as the diffusivity and the Ehrlich-Schwoebel barrier. However, the surfactant atoms should not incorporate into the epitaxial layer.

2.4 Reflection high energy electron diffraction

Reflection high energy electron diffraction (RHEED) is a relevant *in-situ* monitoring tool during the MBE growth. Since RHEED is very sensitive to the surface morphology and the surface reconstruction (arrangement of surface atoms), it can be used to determine the growth rate, growth mode, and composition. Importantly, the high-vacuum environment is required for RHEED system. This requirement limits a utilization of RHEED in vapor phase epitaxy. For a typical RHEED setup, an electron beam with high energy (10-100 keV) is incident on the sample surface at a small angle (less than 5°). The RHEED patterns caused by diffracted electrons are displayed on a phosphor screen.

The diffraction process is based on the interaction of an electron beam with the array of surface atoms. Despite the high electron energy, the use of small angle ensures that the component of electron momentum perpendicular to the surface is small. As a result, electrons are diffracted by atoms at the top monolayers and cannot penetrate far into the sample. That is why RHEED is surface sensitive. Since electrons behave as matter waves, their de Broglie wavelength is given by $\lambda = h/\sqrt{2m_eE_e}$ where h is the Planck constant, m_e is the rest mass of electron, and E_e is the electron energy. Nevertheless, such an equation holds true for E_e < 50 keV at which the relativistic effects are insignificant. The magnitude of the wave vector $\boldsymbol{k}_0$ of high energy electrons is given by $|\boldsymbol{k}_0| = 2\pi/\lambda$.

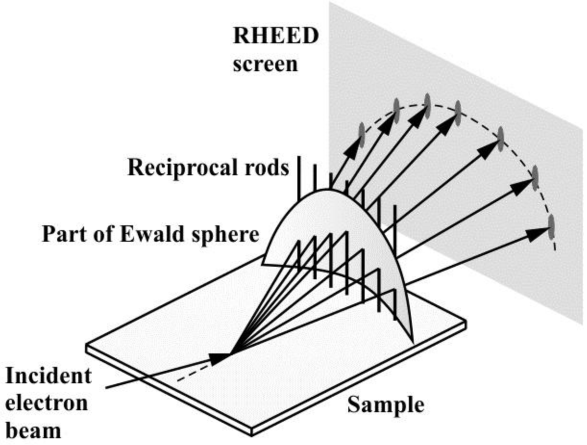

Figure 2.4 Origin of RHEED pattern. Bragg condition for diffraction is satisfied at any intersection points between Ewald sphere and reciprocal rods.

The diffraction condition of RHEED in reciprocal space is introduced with the concepts of Ewald sphere and reciprocal lattice. If a tip of an electron wave vector $\boldsymbol{k}_0$ is pinned at a reciprocal lattice point, the Ewald sphere is defined as a sphere around the origin of $\boldsymbol{k}_0$ with a radius $|\boldsymbol{k}_0|$. A 2D array of surface atoms is represented by a set of lines perpendicular to the surface in real space. Such vertical lines are called reciprocal rods. The Bragg condition for diffraction is satisfied at any intersection points between the Ewald sphere surface and the reciprocal rods, as shown in Figure 2.4. For example, the electron energy of 15 keV corresponding to the de Broglie wavelength of ~10 pm is employed. The radius of Ewald sphere is $|\boldsymbol{k}_0| = 627\,\mathrm{nm}^{-1}$, whereas the distance between reciprocal rods in the reciprocal space is typically in the order of ~20 nm^{-1}. It is obvious that the Ewald sphere is so large that it intersects many reciprocal rods. For this reason, the diffraction pattern on the phosphor screen consists of a set of streaks. This discussion is valid for a flat surface in atomic scale. In the case of the presence of 3D islands, electrons cross such islands and diffract from 3D lattices, leading to a spotty RHEED pattern. According to these results, RHEED can indicate the growth mode. It should be noted that the spot size of the electron beam grazing onto the surface is ~100 μm, meaning that it covers a relatively large area of the surface. The observed RHEED pattern is therefore an average diffraction result.

Another important issue is the correlation between surface reconstruction and RHEED pattern. Reciprocal lattice is an artificial lattice that connects the surface reconstruction in the real space to the RHEED pattern which is a product in the reciprocal space. In fact, the reciprocal lattice is a Fourier transform of the real lattice. Figure 2.5 displays an example of the RHEED patterns of GaAs (001) with β2(2×4) surface reconstruction.

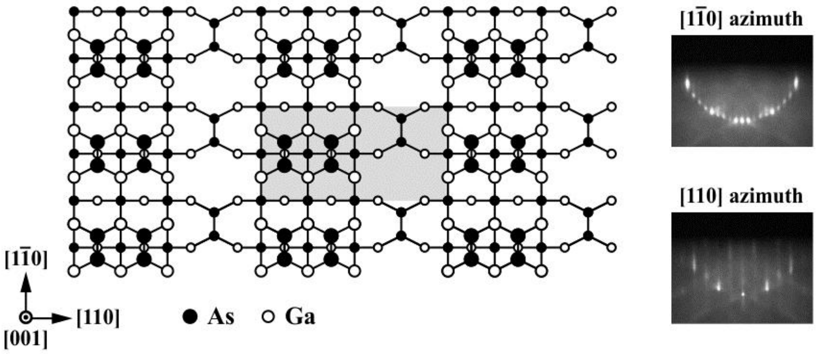

Figure 2.5 β2(2×4) surface reconstruction of GaAs (001) and its corresponding RHEED patterns. Black and white circles denote As and Ga atoms, respectively. Smaller circles indicate atoms further from the surface. The gray rectangular represents a (2×4) unit cell.

RHEED can be utilized for the growth rate calibration through the periodic variation of specular beam (reflected beam) intensity. This technique is generally known as the RHEED intensity oscillations. Such oscillations indicate layer-by-layer growth. The origin of RHEED oscillations can be explained as follows. Starting from the perfectly smooth surface without any deposited material where the specular beam exhibits the maximum intensity, the intensity immediately drops at initial deposition as the surface loses its perfect smoothness. A decrease in specular beam intensity proceeds until the deposited material coverage is equal to a half of monolayer. For further deposition, the specular beam can recover its intensity because the surface configuration moves towards a smooth surface again. Once a monolayer is completed, a second maximum intensity is obtained, implying that the period of oscillations is equal to the time for the growth of one monolayer. The specular beam intensity as a function of deposited material coverage (θ) is illustrated in Figure 2.6. The intensity of such oscillations becomes damped after the completion of several monolayers owing to the residual 2D islands which reach a steady-state density progressively. With usual growth conditions, the group-III flux intensity governs the growth rate because of a unity sticking coefficient of group-III elements. For instance, the deposition rate of Ga is equivalent to the growth rate of GaAs grown under the presence of As atmosphere.

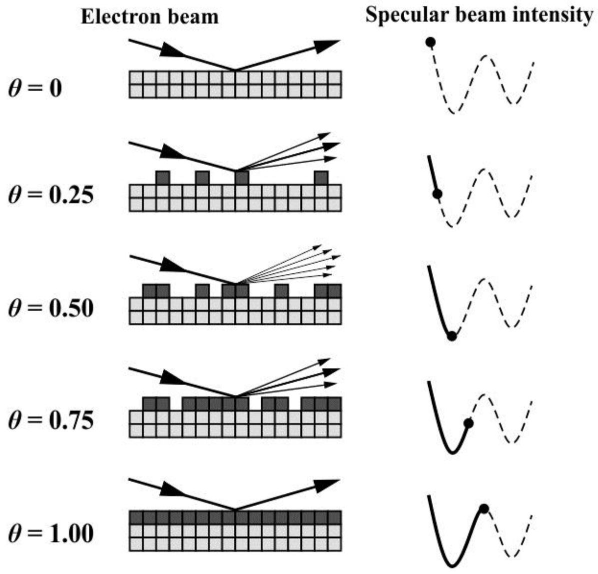

Figure 2.6 RHEED intensity oscillations. θ is the deposited material coverage in a unit of monolayer (ML).

2.5 Droplet epitaxy

The concept of droplet epitaxy was proposed by Koguchi *et al*. in 1990 [4, 30]. For III-V material systems, droplet epitaxy is different from the standard MBE growth which group-III and group-V atoms are simultaneously supplied. Droplet epitaxy technique is based on the incorporation of group-V atoms into the group-III droplets which are initially formed. The growth procedure is shown in Figure 2.7. The first step is the deposition of group-III atoms on the substrate surface without the group-V environment, resulting in the liquid metallic droplets. The second step is the crystallization process at which the group-V flux is supplied to the droplets, leading to the III-V nanostructures. Unlike the SK method, the strain is not necessary for droplet epitaxy to create the nanostructures. The morphology of nanostructures strongly depends on the crystallization temperature and group-V flux intensity. A variety of nanostructures can be fabricated, for example, quantum dots [31], quantum rings [32], concentric quantum rings [33], ring-disk structures [34], dot-disk structures [35], and dot-ring structures [35]. Figure 2.8 displays the schematics of such nanostructures. The fundamentals of growth kinetics will be discussed in more detail later. Besides, if the droplets can dissolve the substrate or the layer underneath them, nanoholes can be formed after crystallization [36].

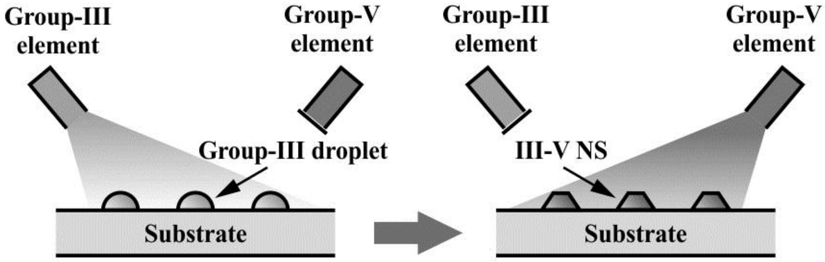

Figure 2.7 Growth procedure for droplet epitaxy. NS denotes the nanostructure.

The droplet formation is based on the VW-like growth mode. Consequently, the chosen group-III element(s) must not wet the substrate surface. It is worth keeping in mind that the low substrate temperature is required for this step so as to prevent the droplets from desorption. The size and density of the droplets can be easily controlled by the substrate temperature, group-III flux intensity, and amount. For example, small droplets with high density can be created by using low substrate temperature and high group-III flux intensity, while large droplets can be obtained by depositing high group-III amount. However, the coalescence of droplets happens at high group-III amounts. The density of nanostructures is equivalent to that of the original droplets unless the substrate temperature is so high that the group-III atoms in the droplets are desorbed and the growth interruption time is so long that the droplet coalescence which lowers the density takes place.

Diffusion is the main mechanism that determines which nanostructures will be formed. As a matter of fact, the diffusion characteristics of atoms are different for different elements. This makes the diffusion mechanism more complicated if more than one group-III and/or group-V elements are used. Hence, only single group-III element (e.g., Ga) and group-V one (e.g., As) are considered for simplicity.

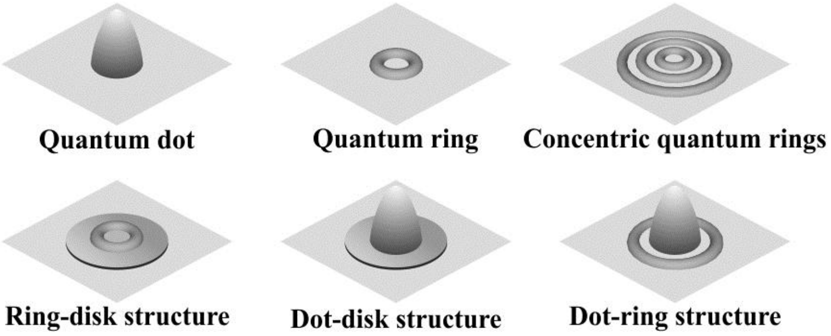

Figure 2.8 Examples of self-assembled nanostructures which can be fabricated by droplet epitaxy.

Roughly, there are two competitive processes during crystallization (see Figure 2.9): the growth of III-V nanocrystals by the diffusion of group-V atoms into the group-III droplet (process A) and at the droplet periphery (process B) [32]. The first happens only when the group-V atoms diffuse through the droplet and reach the droplet/substrate interface where the nanocrystals can grow with some probability. The latter takes place predominantly because the droplet periphery is directly exposed to the group-V flux. At high group-V flux intensity, both processes A and B are significant and the crystallization is fast enough that the droplet shape is still retained, resulting in the quantum dots. On the contrary, at low group-V flux intensity, process A is slower than process B, leading to the quantum rings. In addition to the group-V flux intensity, the substrate temperature plays a crucial role during crystallization because the lateral diffusion of group-III atoms from the original droplets increases with temperature. If the temperature is high enough that the group-III atoms are allowed to diffuse away from the initial position, concentric double rings derived from the growth of III-V nanocrystals at an outer zone can be created. The nanostructure shape is therefore governed by group-V flux intensity and substrate temperature. However, it is not possible to create concentric multiple rings (more than two rings) by the conventional droplet epitaxy because a gradient of group-III atom concentration compels the group-III atoms to diffuse away from the original position as far as possible. In other words, the nanocrystals cannot accumulate between inner and outer rings such that another ring occurs.

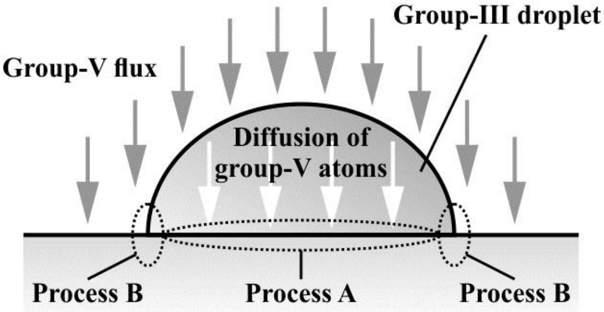

Figure 2.9 Schematic diagram of possible processes during crystallization.

Due to the fact that a reservoir of group-III atoms is always at the center of the growing structure during crystallization, it is possible to create the complex structures (e.g., concentric multiple rings, ring-disk, dot-disk, and dot-ring structures) by the pulsed supply of group-V flux at different intensities and substrate temperatures. This is called pulsed droplet epitaxy [35], which the simple structures like quantum dot, ring, and disk can be combined into a single multifunction nanostructure with unique electronic properties.

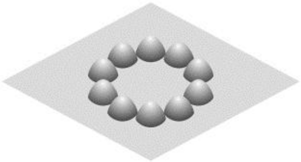

Figure 2.10 Illustration of ring-shaped quantum dot molecules.

In the case of lattice-mismatched droplet epitaxy, the strain also affects the shape derivation of nanostructures, for instance, InP/InGaP ring-shaped quantum dot molecules (see Figure 2.10) at which the formation of circularly aligned quantum dots (rather than quantum rings) is as a result of the strain relaxation [37]. Nevertheless, not all material pairs with lattice mismatch can be chosen for achieving such a peculiar nanostructure.

Since the diffusion is very significant in the droplet epitaxy, some factors involving with the diffusion, such as the anisotropic behavior and the Miller indices of the substrate surface, can cause the deviation of nanostructure morphology. The explicit examples are the anisotropic shape of GaAs quantum dots grown on GaAs (001) surface where the $[1\bar{1}0]$ direction is preferable for the diffusion of Ga atoms [38], and the strange InGaAs nanostructures grown on type-A GaAs surfaces [39].

According to above discussions, the advantages of droplet epitaxy, which cannot be found in other techniques for self-assembled nanostructure fabrication, are summarized as follows:

1. It can be applied to both lattice-matched and lattice-mismatched material systems.
2. Density of nanostructures can be controlled over 10^6-10^{11} cm^{-2}.
3. Many kinds of nanostructures can be obtained.
4. Various substrates are allowed to use.
5. Energy consumption is reduced because droplet epitaxy is performed at low temperature.

2.6 Low-dimensional structures

For a bulk semiconductor, charge carriers (electrons and/or holes) can move freely in all three dimensions. However, if any of the structural dimensions is reduced to be comparable to the de Broglie wavelength, the charge carriers experience the confinement of motion in the corresponding direction, giving rise to the quantum confinement effect which makes the electronic and optical properties considerably deviate from the bulk. A de Broglie wavelength of a carrier having an effective mass m^* can be calculated by

$$\lambda = h(3m^* k_B T)^{-1/2} \tag{2.4}$$

where h is the Planck constant, k_B is the Boltzmann constant, and T is temperature. The de Broglie wavelength of charge carriers in semiconductors is in the nanometer scale.

The carrier wave functions in semiconductors can be obtained by solving the time-independent Schrödinger equation in the effective-mass approximation [40]:

$$\left[-\frac{\hbar^2}{2m^*}\nabla^2 + V(\boldsymbol{r})\right]\psi(\boldsymbol{r}) = E\,\psi(\boldsymbol{r}) \tag{2.5}$$

where $\hbar$ is the reduced Planck constant, $\boldsymbol{r} = (x, y, z)$ is the position vector, $V(\boldsymbol{r})$ is the potential distribution, E is the carrier energy, and $\psi(\boldsymbol{r})$ is the carrier envelope function. As the effective-mass approximation is based on an assumption that the envelope functions slowly fluctuate on the scale of lattice period, it can be applied not only to the bulk materials but also to the low-dimensional structures.

In the case of a bulk, the movement of carriers is not restricted to any direction, i.e., the 0D confinement. The relation between the carrier energy and the carrier wave vector $\boldsymbol{k} = (k_x, k_y, k_z)$ is thus the same as a free particle:

$$E_{0\mathrm{D}} = \frac{\hbar^2}{2m^*}k^2 \tag{2.6}$$

where $k^2 = k_x^2 + k_y^2 + k_z^2$.

If one of three dimensions (e.g., L_z) is squeezed into the order of the de Broglie wavelength, the carriers are allowed move in the xy plane. In other words, this is the 1D confinement along the z direction. Such a structure is called a quantum well (QW) where the carrier energy is given by

$$E_{1\mathrm{D}} = E_n = \frac{\hbar^2}{2m^*}\left[k_x^2 + k_y^2 + \left(\frac{n\pi}{L_z}\right)^2\right] \tag{2.7}$$

Once the carriers are constrained along the y and z directions with the dimensions of L_y and L_z, they can only travel along the x direction. This situation is the 2D confinement which is found in a quantum wire (QWR) where the carrier energy can be expressed by

$$E_{2\mathrm{D}} = E_{m,n} = \frac{\hbar^2}{2m^*}\left[k_x^2 + \left(\frac{m\pi}{L_y}\right)^2 + \left(\frac{n\pi}{L_z}\right)^2\right] \tag{2.8}$$

The carriers are completely localized when they are confined in all three spatial directions with the dimensions of L_x, L_y, and L_z. This is the 3D confinement that is generally referred to a quantum dot (QD). The carrier energy is determined by

$$E_{3\mathrm{D}} = E_{l,m,n} = \frac{\hbar^2}{2m^*}\left[\left(\frac{l\pi}{L_x}\right)^2 + \left(\frac{m\pi}{L_y}\right)^2 + \left(\frac{n\pi}{L_z}\right)^2\right] \tag{2.9}$$

From Equations (2.7) to (2.9), the carrier energies in low-dimensional structures depend on the dimension(s) along the direction(s) of confinement as well as the quantum numbers *l*, *m*, and *n*. The corresponding density of states, which is the number of states per unit energy for 0D, 1D, 2D, and 3D confinements, is as follows:

$$\rho_{0\mathrm{D}}(E) = \frac{(2m^*)^{3/2}}{2\pi^2\hbar^3}E^{1/2} \tag{2.10}$$

$$\rho_{1\mathrm{D}}(E) = \frac{m^*}{\pi\hbar^2 L_z}\sum_{n}\Theta(E - E_n) \tag{2.11}$$

$$\rho_{2\mathrm{D}}(E) = \frac{(2m^*)^{1/2}}{\pi\hbar L_y L_z}\sum_{m,\,n}(E - E_{m,\,n})^{-1/2} \tag{2.12}$$

$$\rho_{3\mathrm{D}}(E) = \frac{2}{L_x L_y L_z}\sum_{l,\,m,\,n}\delta(E - E_{l,\,m,\,n}) \tag{2.13}$$

where Θ is the Heaviside function and δ is the delta function.

It is clearly seen that the density of states is drastically changed when the carrier confinement is introduced. The density of states is proportional to $E^{1/2}$ and continuous for the bulk, whereas it becomes step-like for the QW. In the case of QWR, the density of states is inversely proportional to $E^{1/2}$. Interestingly, the QD possesses the discrete density of states, which is similar to a real atom. That is why the QD is often called an artificial atom.

As previously mentioned, the de Broglie wavelength is the criterion to define the low-dimensional structures in which the quantum confinement effect appears. It should be noted that both electron and hole have their own wavelengths which are not necessary to be the same because they are related to the effective mass, making this criterion ambiguous. Thus, the concept of exciton Bohr radius, which is derived from the electron and hole effective masses, is used instead for convenience. An exciton is composed of an electron and a hole, bound together via the Coulomb attraction. The exciton Bohr radius is the spatial extension of an exciton, which is defined by

$$a_B = \frac{4\pi\varepsilon\hbar^2}{\mu^* e^2} \tag{2.14}$$

where ε is the permittivity, μ^* is the reduced effective mass which is involved with the effective masses of electron (m_e^*) and hole (m_h^*) and determined by $(1/m_e^* + 1/m_h^*)^{-1}$, and e is the electron charge. Since the exciton Bohr radius of typical semiconductors is usually larger than the lattice constant, the quantum confinement effect, which takes place when the structure dimension is comparable to or less than a_B, can be observed in the nanostructures that are easily provided by the present fabrication technologies as well as the self-assembly methods.

In addition to the low-dimensional structures discussed above, quantum ring (QR) can confine the charge carriers in all three spatial directions like the QD and therefore has a discrete density of states [41]. From the topological point of view, the QR is doubly connected, while the QD is singly connected. This non-trivial topology of QR leads to the carrier energy levels which depend on the angular momentum through the azimuthal quantum number. For simplicity, the QR is assumed to have an infinitesimal width so that it can be treated as a one-dimensional QWR bent into a circle with radius r. According to its periodic boundary conditions, the energy levels in the QR are

$$E_\ell = \frac{\hbar^2}{2m^*}\left(\frac{\ell}{r}\right)^2 \tag{2.15}$$

where $\ell = 0, \pm 1, \pm 2, ...$ is the azimuthal quantum number. Interestingly, when the inner part of QR is threaded by a magnetic flux ϕ resulting from a magnetic field B, the carrier moving around the QR trajectory experiences an additional phase which modifies its energy levels to

$$E_\ell = \frac{\hbar^2}{2m^*}\left(\frac{1}{r^2}\right)\left(\ell + \frac{\phi}{\phi_0}\right)^2 \tag{2.16}$$

where $\phi = \pi r^2 B$ and ϕ_0 is the flux quantum. It means that the ground state energy is periodic in the magnetic flux with a period of ϕ_0. This is known as Aharonov-Bohm type oscillations. In addition, such a periodic ground state leads to the existence of persistent current [1] which is given by

$$I_p = -\frac{\partial E_\ell}{\partial \phi} \tag{2.17}$$

The persistent current is also periodic with the same period of the ground state energy.

2.7 Photoluminescence spectroscopy

Photoluminescence (PL) is the luminescence from a substance exposed to the light which photon energy is high enough that the substance can absorb it. In the context of semiconductors, PL results from the radiative recombination between electrons and holes which are generated by the light having photon energy larger than the band gap in the case of bulks, or the effective band gap (i.e., the difference between electron and hole quantization energy levels) in the case of nanostructures. It is worth keeping in mind that not all photo-excited carriers contribute to the PL emission because non-radiative recombination may occur and results in the phonon emission. The PL spectroscopy is generally used to investigate the electronic states, crystal quality, composition, and optical properties of semiconductors.

A typical PL spectroscopy setup consists of the following components: (1) an excitation light source, (2) optical elements for focusing the light source to a sample and the luminescence from the sample, (3) a monochromator for resolving the wavelengths in the luminescence, (4) a detector, and (5) a data acquisition system. A standard lock-in technique is often employed to amplify the PL signals. The sample is usually placed in a cryostat where the temperature can be precisely controlled.

According to this dissertation, the discussion on the PL of nanostructures and how to interpret the PL results are relevant. Due to the quantum size effect, the ground-state PL peak energy indicates the nanostructure size, i.e., the smaller nanostructures provide the higher ground-state energy. The PL line shape is related to the size distribution of nanostructures. The broad PL spectrum reflects the poor size uniformity. For self-assembled III-V QDs and QRs, their height is much less than their lateral dimension. Again, owing to the quantum size effect, the quantization energy levels are determined by the height, whereas the lateral dimension governs the separation between the energy levels. If the nanostructure height is assumed to be the dominant factor which defines the peak position of a single nanostructure, the relation between height distribution and PL line width, which is represented by a full width at half maximum (FWHM), can be expressed by $\Gamma \propto (h_a - \Delta h/2)^{-2} - (h_a + \Delta h/2)^{-2}$ where Γ is the FWHM of a PL spectrum, h_a is the average height, and Δh is the FWHM of the height distribution [42].

To observe the carrier behaviors and the ability of carrier confinement in the nanostructures, one of the efficient techniques is the temperature-dependent PL measurement. In general, the PL peak energy shifts to the lower energy with an increase in temperature as a result of the thermal lattice expansion and the electron-phonon interaction. The temperature dependence of the peak energy (E_{PL}) follows the Varshni empirical equation:

$$E_{PL}(T) = E_0 - \frac{\alpha T^2}{T + \beta} \tag{2.18}$$

where E_0 is the peak energy at 0 K, and α and β are Varshni coefficients [43]. Due to the electron-phonon scattering, the PL line width also increases with temperature. In the case of the strong electron-phonon coupling, the temperature-dependent FWHM of a Gaussian PL profile can be explained by

$$\Gamma(T) = [(8\ln 2)S(\hbar\omega)^2(2\bar{n}+1)]^{1/2} \tag{2.19}$$

where $\bar{n} = [\exp(\hbar\omega/k_B T) - 1]^{-1}$, S is the Huang-Rhys factor which is related to the electron-phonon coupling strength, and $\hbar\omega$ is the phonon energy [44, 45]. In the case of the QDs grown by the SK mode where the presence of the wetting layer is unavoidable, the variations of the peak energy and the PL line width do not follow Equations (2.18) and (2.19) since the wetting layer provides a channel for the migration of thermal-activated carriers between QD ensembles, resulting in a faster decrease in the peak energy than the band gap of its bulk material and an unusual reduction in FWHM at intermediate temperatures [46-48].

In addition to the emission energy and the PL line shape, the carriers in the nanostructures are affected by the temperature. This can be clearly seen from the quenching of PL intensity when the temperature increases as a consequence of the thermal escape of carriers from the nanostructures into the barriers or the non-radiative recombination centers. The temperature dependence of integrated PL intensity (I_{PL}) can be simply described by a single thermal activation energy E_A:

$$I_{PL}(T) = \frac{I_0}{1 + C\exp(-E_A / k_B T)} \tag{2.20}$$

where I_0 is the integrated PL intensity at 0 K, C is the constant which is a ratio of the non-radiative lifetime to the radiative one [49]. Sometimes, two activation energies (E_{A1} and E_{A2}) are required to obtain the better fit to the PL data over the temperature range. In this case, Equation (2.20) is modified to

$$I_{PL}(T) = \frac{I_0}{1 + C_1\exp(-E_{A1} / k_B T) + C_2\exp(-E_{A2} / k_B T)} \tag{2.21}$$

where C_1 and C_2 are the constants that measure the strength of two thermal quenching processes. The process with the larger activation energy is interpreted as the thermal escape of carriers from the nanostructures, while the other is related to the defects [50, 51]. However, the two activation energies may be represented the quenching processes at low-temperature and high-temperature regions [52].

PL can give the information of the excited states and the recombination mechanisms by the variation of excitation power. The PL emission from the nanostructures is mostly contributed by the radiative recombination between electrons and holes which the overlap of their wave functions is sufficient, and such a recombination follows the selection rules [53]. For example, an electron in the ground state will recombine with a hole in the ground state, a first-excited state electron will recombine with a first-excited state hole, and so on. As the carrier relaxation time to the ground states is much shorter than the carrier lifetime, the ground-state emission can be seen even at low excitation power. Due to the fact that the number of photo-generated carriers increases with the excitation power, the ground state may be fully occupied and the adjacent excited states are subsequently filled. This is called a band-filling effect. The ground-state and excited-state emissions are thus observed at high excitation power. The excited-state peaks in a PL band become more resolved at low temperature. The recombination processes can be interpreted from the power-dependent PL measurement because the relation between the PL intensity and the excitation power (P) is given by $I_{PL}(P) \propto P^{\gamma}$ where γ is the exponent. $\gamma < 1$ indicates the defect-related recombination, whereas $1 < \gamma < 2$ reflects the typical excitonic recombination at which the PL intensity relies on the carrier density [54, 55].

Above discussions are the basic concepts of general PL spectroscopy. Indeed, other useful information, such as the polarization properties, the carrier dynamic behaviors, and the absorption spectra, can be probed by the PL spectroscopy with a specific system. However, these issues will be concisely mentioned as they are beyond the scope of this dissertation.

If the nanostructures exhibit the anisotropic shape, the lateral confinement becomes anisotropic and can be seen from the polarized photoluminescence (PPL) measurement where a polarizer is added to the general PL setup. For instance, the highly anisotropic GaAs QDs, which their bases along the $[1\bar{1}0]$ direction are longer than those along the [110] direction, leads to the higher PL intensity in the $[1\bar{1}0]$ direction than in the [110] one [56]. In this case, a degree of polarization can be defined by

$$DOP = \frac{I_{[1\bar{1}0]} - I_{[110]}}{I_{[1\bar{1}0]} + I_{[110]}} \tag{2.22}$$

where $I_{[1\bar{1}0]}$ and $I_{[110]}$ are the PL intensity parallel to the $[1\bar{1}0]$ and [110] directions, respectively.

Time-resolved photoluminescence (TRPL) is another kind of PL spectroscopy. The carrier capture process in the nanostructures and the carrier lifetime are investigated by TRPL measurements. Unlike the general PL system, a relatively short pulsed excitation source and a time resolving system are necessary to obtain the TRPL results which are usually displayed by the time dependence of the number of photons. When the carriers are excited by a short pulsed laser, the number of photons will rise to some maximum value and subsequently decay. The time taken to reach the maximum photon amount (I_m) in the TRPL data reflects the time required for the carrier capture in the nanostructures, while the decrement in photon amounts is associated with the radiative lifetime. The decay line can be simply explained by

$$I(t) = I_m \exp(-t/\tau) \tag{2.23}$$

where τ is the time constant. The larger time constant suggests the longer radiative lifetime. Nonetheless, the decay line may be fitted with two time constants (τ_1 and τ_2) [57], i.e.,

$$I(t) = I_1 \exp(-t/\tau_1) + I_2 \exp(-t/\tau_2) \tag{2.24}$$

where $I_1 + I_2 = I_m$.

If the wavelength (or photon energy) of the excitation source is varied at the same time that the some specific PL wavelength is monitored, the absorption spectra or the information on the electronic states including the excited states and the defect states can be taken. This is the concept of photoluminescence excitation (PLE) and different from the PL which the excitation wavelength is fixed but the PL emission is collected throughout the range of desired wavelengths. The PLE setup, therefore, requires a tunable laser or a broad-spectrum light source combined with a monochromator.

A main limitation of the standard PL spectroscopy is the difficulty to probe the optical properties from individual nanostructures since the PL emission from a nanostructure is rather weak and the spot size of the focused excitation laser is still larger than the single-nanostructure size. To overcome this limitation, micro-photoluminescence (micro-PL) has been introduced. In the micro-PL system, an optical microscope is the pivotal equipment for focusing the laser and the PL signals.

2.8 Interesting topics in GaSb/GaAs nanostructures

2.8.1 Critical thickness

A lattice mismatch relative to the substrate is defined by $(a_s - a_e)/a_s$ where a_e and a_s are the lattice constants of an epitaxial layer and a substrate, respectively. Since the lattice constants of GaSb and GaAs are 0.60960 and 0.56534 nm [58], respectively, the lattice mismatch in the case that GaSb is grown on GaAs is around

7.8%, giving rise to the compressive strain. It means that the epitaxial growth of GaSb on a GaAs substrate is in the SK mode, i.e., the growth begins with a pseudomorphic 2D layer-by-layer fashion, leading to a wetting layer, and followed by the spontaneous formation of 3D islands or QDs after exceeding a critical thickness (θ_c). As the wetting layer is biaxially strained to match the in-plane lattice constant of the substrate, some portion of strain energy is reduced through the tetragonal distortion in the wetting layer with the out-of-plane lattice constant. When the thickness of GaSb layer is above θ_c, the appearance of QDs is a result of a reduction in strain energy in both in-plane and out-of-plane directions at the expense of surface energy such that the total energy of the system is minimized.

Interestingly, the value of θ_c in the GaSb/GaAs (001) system is widely varied from 0.4 to 4.0 monolayers (ML) [5, 59-65]. This is much different from the InAs/GaAs (001) system where θ_c is typically found in a narrow range of 1.4-1.8 ML regardless of the growth conditions with the usual growth temperatures (450-510 °C) [66-70]. Consequently, the growth mechanisms and the determination of θ_c which is quite uncertain in the GaSb/GaAs system are complicated, giving rise to the difficulty to reproduce the QDs.

By applying the continuum mechanics and comparing the obtained strain energy to the InAs/GaAs (001) system, the calculated θ_c for GaSb/GaAs (001) is 1.2 ± 0.5 ML which is consistent with the cross-sectional scanning tunneling microscopy (XSTM) results taken from the epitaxial growth of GaSb at the typical growth temperatures (470-515 °C) with the moderate growth rates (0.1-1.0 ML/s) [71]. It is worth noticing that the GaSb QDs cannot be grown at ~520 °C, and the wetting layer is only formed at this temperature [72]. However, the thermodynamic and kinetic aspects and the Sb-for-As exchange reaction are not included in such calculations. In the growth of GaSb/GaAs QDs, the Sb flux is often irradiated on the As-stabilized GaAs surface of the buffer layer in order to remove the residual As and stabilize the Sb flux. This is called Sb soaking process where the Sb-for-As exchange takes place and leads to a GaSb layer forming without the Ga deposition. The thickness of GaSb layer is decided by the soaking time, Sb flux intensity, and substrate temperature, and can be up to 2 ML [6, 73]. Therefore, the Sb-for-As exchange reaction plays a crucial role in the critical thickness. In addition, the epitaxial growth of GaSb on GaAs without the Sb soaking process may result in the formation of QRs (instead of QDs) because the spatial inhomogeneity of the Ga atom population and the As/Sb intermixing induce the instability in both the wetting layer and the shape of initially formed QDs [18].

2.8.2 Anion exchange reaction

Anion exchange may occur during the growth of III-V heterostructures with different anions of group-V elements. This affects the composition, interface abruptness, electronic properties, optical properties, and device performance. Bond strengths can be seen as a rule of thumb (not a criterion) to predict whether the anion exchange reaction will take place or not. According to a thermodynamic analysis, the higher bond strengths imply the larger tendency for the exchange reaction [74]. In other words, the strong-for-weak-bond exchange (e.g., As-for-Sb) is always expected to happen with a higher degree of extent, while the amount of the weak-for-strong-bond exchange (e.g., Sb-for-As) tends to be small. As a matter of fact, the direction of exchange reaction is governed by the change of free energy which is contributed not only by the bond strength but also by other factors such as strain energy, surface energy, and segregation. Moreover, the equilibrium point of reaction can be shifted by such factors [74]. For instance, the weak-for-strong-bond exchange is energetically preferred because it reduces the surface energy as a result of the formation of weak bonds on the surface.

A major challenge of the growth of GaSb/GaAs QDs followed by capping with a GaAs layer is the control of group-V flux exposure during switching from As to Sb and vice versa. As previously explained, the Sb-for-As exchange reaction happens in the Sb soaking process before growing the GaSb/GaAs QDs in the SK mode, and causes the formation of GaSb layer which effects on the critical thickness. The Sb-for-As exchange becomes more pronounced at high temperatures, high Sb flux intensity, and long Sb-soaking duration. Nonetheless, the thickness of GaSb layer seems to be limited at approximately 2 ML [6, 73]. The As-for-Sb exchange reaction, which is the reverse process, is unavoidable during the growth of GaAs capping layer on the GaSb QDs, where the group-V flux is changed from Sb to As. It is worth pointing out that the As-for-Sb exchange is stronger than the Sb-for-As exchange because Ga-As bond is stronger than Ga-Sb bond [16, 75, 76]. In the GaAs capping process, the use of As_2 which is more reactive than As_4, high growth temperature, and low growth rate enhance the As-for-Sb exchange reaction [16, 77-79]. Due to the fact that a decrease in Sb content in the GaSb wetting layer and QDs can reduce the strain energy, the As-for-Sb exchange is energetically favorable. Consequently, Sb atoms tend to be removed from the GaSb structures by re-evaporating or staying at the growth front in a form of Sb floating layer [16]. This phenomenon can cause the transformation of the GaSb QDs. Since the apex of a GaSb QD is the region where the compressive strain is significantly relaxed, and experiences the mismatch strain more than other parts when the QD is capped with GaAs which has the smaller lattice constant, Sb atoms at the QD apex are easily repelled owing to the weak Ga-Sb bond and replaced by As atoms [16]. As a result, the GaSb QD can be transformed into the QR. Nevertheless, such a transformation can be prevented by the irradiation of Sb flux on the GaSb QDs for a proper duration before capping [80]. Hence, it is worth keeping in mind that the QD-to-QR transformation does not always happen.

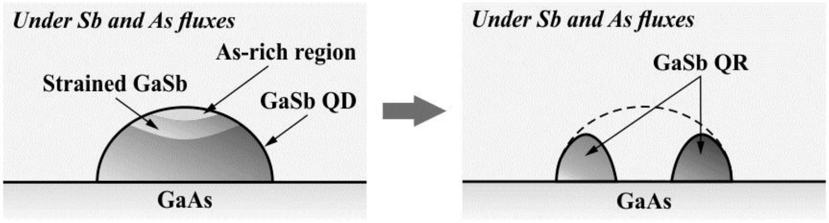

Figure 2.11 Formation mechanism for the transformation of GaSb QD to QR by Sb and As exposure.

By controlling the ratio of Sb to As fluxes (Sb/As) in the soaking process which is performed after growing the GaSb QDs, the GaSb QRs can be obtained without capping with GaAs. The As-for-Sb exchange reaction is responsible for the QD-to-QR transformation. However, the transition from QD to QR is not a spontaneous procedure with a constant rate of As-for-Sb exchange because not all the GaSb QDs are transformed into the QRs at high Sb/As ratio [17]. The formation mechanism of a GaSb/GaAs QR is shown in Figure 2.11. Once a GaSb QD is exposed to the Sb and As fluxes with some Sb/As ratio, it is possible that As atoms may condense and create an As-rich region at the QD apex. This induces the mismatch strain and forces Sb atoms to diffuse away so as to reduce the strain energy, resulting in the QR. In the case that the QRs are intentionally formed, a decrease in the Sb/As ratio speeds up the QR formation. At given Sb/As ratio and growth temperature, the long exposure time can encourage the As-for-Sb exchange reaction, giving rise to the less abrupt GaSb/GaAs interface and the higher PL intensity from the GaSb QRs embedded in a GaAs matrix due to the more overlap between electron and hole wave functions [9]. Intriguingly, the GaSb QDs can be destroyed by the severe As-for-Sb exchange occurring at high growth temperature and low Sb/As ratio, and only a flat GaSb surface is left without the existence of GaSb QRs [17].

2.8.3 Growth interruption

It is generally accepted that growth interruption (GI) can modify the morphology of self-assembled QDs. For example, the size variation in InAs/GaAs QDs takes place when the GI is introduced [81]. An anomalous effect of the GI on the GaSb/GaAs QDs grown by MBE has been reported [82]. The GI applied under Sb flux causes the disappearance of the QDs, as evidenced by the transition from spotty to streaky RHEED patterns and the PL measurement. Furthermore, it is found that the GI time required for smoothing out the QDs is decided by the GaSb coverage. This phenomenon can be described by the strain redistribution and the anion exchange reaction during GI.

2.8.4 Type-II band alignment

It is well known that a GaSb/GaAs heterostructure exhibits a staggered type-II band alignment. A realistic approximation of a band alignment can be obtained by the model-solid theory where the strain effects are included and represented by the deformation potentials [83]. The calculated band alignments for completely relaxed and pseudomorphic GaSb/GaAs QWs [73] are illustrated in Figure 2.12. It is obvious that the compressive strain due to the lattice mismatch plays a pivotal role in the top of GaSb heavy-hole (HH) and light-hole (LH) subbands and the bottom of GaSb conduction band. The large valence band offset indicates that only holes are localized within the GaSb region, while electrons do not experience any confinement but occupy the GaAs region, leading to a spatial separation between electron and hole wave functions. As a result of a low recombination probability in the type-II heterostructures, the radiative lifetime is longer than the type-I heterostructures where electrons and holes are confined in the same region. These concepts can be applied not only to the QWs but also to the other kinds of nanostructures. In the case of GaSb/GaAs QDs, it is found that the hole confinement potential in the QD is as high as 450 meV [10] and the TRPL result reveals that the decay time constant is ~23 ns [57] which is much longer than type-I InAs/GaAs QDs having the radiative lifetime of ~1 ns [84].

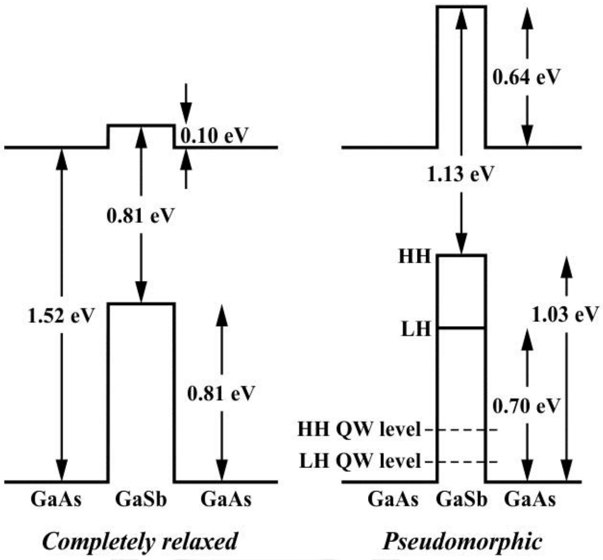

Figure 2.12 Schematic band alignment for GaSb/GaAs heterostructures of (a) a completely relaxed and (b) a pseudomorphic GaSb layer.

The PL from GaSb nanostructures buried in a GaAs matrix results from the radiative recombination between holes in the GaSb nanostructures and electrons in the GaAs matrix. The population of confined holes induces the electrons in the GaAs barriers to reside around the GaSb nanostructures via the Coulomb attraction, giving rise to an internal electric field at the GaSb/GaAs interface, which bends the conduction band into the triangular QW (see Figure 2.13). This is called a band-bending effect. Therefore, the electron energy levels at the interface become quantized. An increment in photo-generated carriers by increasing the excitation power leads to the stronger band-bending effect and shifts the quantization levels for electrons at the GaSb/GaAs interface, causing the blueshift of the ground-state emission. This is a characteristic of type-II band alignment. The shift of the ground-state energy due to the band-bending effect can be described by

$$\Delta E_{BB} = \left(\frac{\hbar^2}{2m_e^*}\right)^{1/3} \left(\frac{9\pi}{8}\right)^{2/3} \left(\frac{2\pi e^2}{\varepsilon}\right)^{2/3} n_w^{2/3} \qquad (2.25)$$

where n_w is the photo-generated carrier density at the triangular QW [73]. The energy shift can be connected to the excitation power (P) by a rate equation:

$$G = Bn_w^2 \qquad (2.26)$$

where G is the carrier generation rate and proportional to the excitation power, and B is the bimolecular radiative recombination coefficient [85]. Therefore, $\Delta E_{BB} \propto P^{1/3}$. This model is generally used to characterize the type-II nanostructures. However, in the case of a type-II GaAsSb/GaAs QW, it is found that the energy shift may not follow the band-bending model throughout the wide range of excitation power, i.e., the energy shift $\Delta E_{PL} \propto P^{\beta}$ where $\beta = 1/2$ for low excitation and $\beta = 1/4$ for high excitation [85]. From this, it can be deduced that $\beta = 1/3$ holds true for moderate excitation. Furthermore, β should be 1/2 if the capacitive charging effect owing to the spatial separation between electrons and holes is considered, but the experimental results do not conform to such an expectation [86]. These arguments emphasize that the origin of the blueshift in the type-II nanostructures is still elusive.

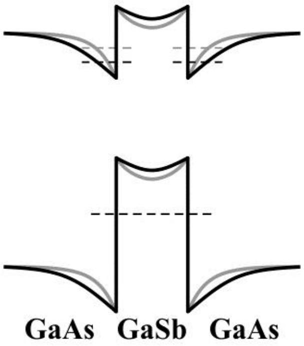

Figure 2.13 Schematic band alignment for a GaSb/GaAs heterostructure including the band-bending effect. The gray lines represent the stronger band-bending effect.

The band-bending effect in GaSb/GaAs QDs can cause the dependence of thermal activation energy on the excitation power [87]. As the internal electric field at the GaSb/GaAs interface is stronger when the excitation power increases, the activation energy gets reduced. Meanwhile, the blueshift of the PL peak energy is achieved. Consequently, the sum of the activation energy and the PL peak energy should be constant regardless of the excitation power.

For type-II nanostructures, it is possible that in some temperature range, there is a competition between the electron-phonon interaction and the band-bending effect due to the population of the thermal-excited carriers. In addition, the presence of an optically induced charge depletion for some cases in GaSb/GaAs nanostructures gives rise to the anomalous PL results [88]. Such effects make the temperature dependence of PL peak energy deviate from the prediction by the Varshni empirical equation.

Chapter 3

Experimental procedures and equipment

The experimental procedures and equipment for sample preparation and characterization are briefly described in this chapter. All samples were grown in a solid-source molecular beam epitaxy (MBE) installed with a 15-keV reflection high energy electron diffraction (RHEED) system and an Sb valved-cracker cell. The GaSb nanostructures on the GaAs (001) substrates were formed by droplet epitaxy. The morphology of nanostructures was investigated by atomic force microscopy (AFM). The optical properties of GaSb nanostructures embedded in the GaAs matrix were examined by photoluminescence (PL) measurement.

3.1 Molecular beam epitaxy

Every sample was fabricated in Riber Compact 21 solid-source MBE machine, as shown in Figure 3.1. The main elements required for this dissertation are gallium (Ga), arsenic (As), and antimony (Sb). Ga and As are contained in the pyrolytic boron nitride (PBN) crucibles which are placed within the separate conventional effusion cells. On the contrary, the valved-cracker cell having three independent heaters for the reservoir, valve, and cracker is utilized to produce the beam of Sb radicals which can be Sb_1, Sb_2, and Sb_4, depending on the cracker temperature. The cooled water (~20 °C) is needed to flow during the valved-cracker cell operation. For all effusion and valved-cracker cells, the cell temperatures are controlled by the computer using the feedback from thermocouples.

The load-lock chamber, the buffer chamber, and the introduction chamber are commonly used by both Riber Compact 21 and Riber 32P because such two machines are connected together to reduce the working area (see Figure 3.1). Each chamber is separated by gate valves. The high vacuum environment for each chamber is maintained by pumping systems consisting of ion pumps and titanium sublimation pumps. The load-lock chamber interposes between vacuum and standard atmosphere, and is the only one chamber which is allowed to be vented for inserting or taking out the sample. A turbomolecular pump is used to lower the pressure in the load-lock chamber from the standard atmosphere to the vacuum level of ~10^{-6} Torr after inserting the new sample or taking out the grown sample. Such a vacuum level is safe to open the gate valve to meet the higher vacuum level, which is less than 10^{-8} Torr, in the buffer chamber. It is necessary to wait until the pressure of the buffer chamber is $\sim5\times10^{-9}$ Torr before the new sample is transferred to the introduction chamber in order to remove the contaminants and moisture. Subsequently, the sample is brought to the growth chamber which possesses the background pressure of $\sim10^{-10}$ Torr. Liquid nitrogen is required for the cryopanels of the growth chamber to keep the ultra-high vacuum environment during the growth and to minimize the unintentional impurities which may get incorporated into the deposited layers.

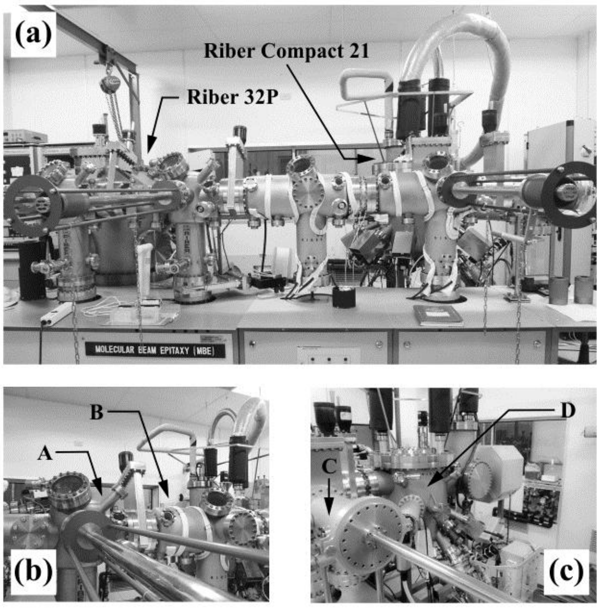

Figure 3.1 (a) Riber Compact 21 and Riber 32P MBE systems connected together. (b) A and B are the introduction and buffer chambers, respectively. (c) C and D are the load-lock and growth chambers, respectively.

Before loading the new sample into the MBE system, the semi-insulating GaAs (001) substrate having the size of around 1.0 cm × 1.5 cm is mounted on an unpolished 3-inch Si wafer by indium glue, and then assembled with a substrate holder. The sample can be transferred between the chambers by the wafer cassettes (carts) together with magnetic arms. The new sample is heated at 450 °C for 1 h in the introduction chamber to eliminate moisture and volatile contaminants.

Once the decontaminated sample is perfectly inserted to the substrate manipulator in the growth chamber, the first process of the MBE growth is to remove native oxide from the substrate surface at 580 °C under As_4 flux of 8×10^{-6} Torr for 10 min. After oxide removal, a GaAs buffer layer with a thickness of a few hundred nanometers is grown at 580°C. When the GaAs buffer layer is prepared, the desired sample structures are ready to be grown. According to this dissertation which is intensively dedicated to the variations of growth parameters in the droplet epitaxy of GaSb nanostructures, the growth condition for a specific study will be thoroughly described later because there are many parameters in the droplet epitaxy technique, which effect on the structural and optical properties of GaSb nanostructures.

3.2 Droplet epitaxy of GaSb/GaAs nanostructures

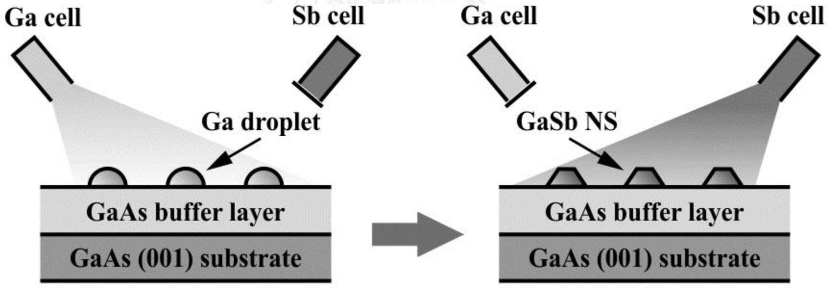

Figure 3.2 Droplet epitaxy of GaSb nanostructures on GaAs (001) substrate. NS denotes the nanostructure.

In the droplet epitaxy, the deposition of group-III element(s) for droplet formation has to be done without the environment of group-V element(s). For this reason, after the growth of GaAs buffer layer, the As_4 flux must be terminated in order to remove the As atmosphere in the growth chamber. Once the background pressure of the growth chamber is less than 5×10^{-9} Torr, Ga is deposited on the substrate surface to form the liquid Ga droplets, and the Sb flux is then supplied to the droplets for crystallization into the GaSb nanostructures. The growth procedure for the droplet epitaxy of GaSb nanostructures on the GaAs (001) substrate is illustrated in Figure 3.2.

3.3 Reflection high energy electron diffraction

Reflection high energy electron diffraction (RHEED) is a powerful tool for *in-situ* monitoring during the growth. The RHEED system is composed of a 15-keV electron gun, a phosphor screen, a charge-coupled device (CCD) camera, and a computer for data acquisition and analysis. The benefits of the RHEED observation are the growth rate determination through the RHEED intensity oscillations which their period is equal to the time for the growth of one-monolayer deposited material, as mentioned in Chapter 2, and the calibration of the substrate surface temperature which will be discussed below. Due to the fact that RHEED is very surface sensitive, the surface morphology of the sample can be interpreted from RHEED patterns. Besides, the variation of specular beam intensity during droplet epitaxy reflects the evolution of nanostructures. Such a variation as a function of time is recorded and analyzed by ImageJ image processing program.

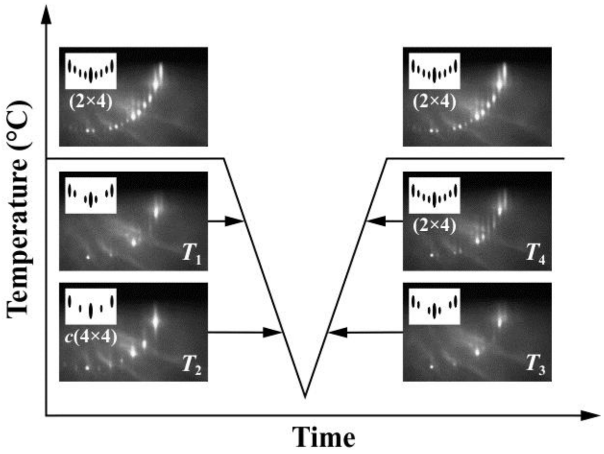

Figure 3.3 Surface temperature calibration by the transition of RHEED patterns.

Since the semi-insulating GaAs (001) wafers are used as the substrates, the surface temperature can be indirectly obtained by the change of surface reconstruction from As-terminated (2×4) to *c*(4×4), which is clearly seen from RHEED patterns [89]. The calibration process performed under As_4 pressure of 8×10^{-6} Torr is explained as follows. The substrate temperature is decreased from the temperature for the growth of GaAs buffer layer with a rate of 10 °C/min until the *c*(4×4) pattern appears, and then increased with the same rate until the (2×4) pattern comes again. Figure 3.3

shows the different RHEED patterns at the different temperatures of T_1, T_2, T_3, and T_4. These temperatures are taken from the thermocouples and defined as the temperature at which the RHEED patterns change. An average temperature, i.e., $(T_1 + T_2 + T_3 + T_4)/4$, is equivalent to the real surface temperature of 500 °C [89].

3.4 Atomic force microscopy

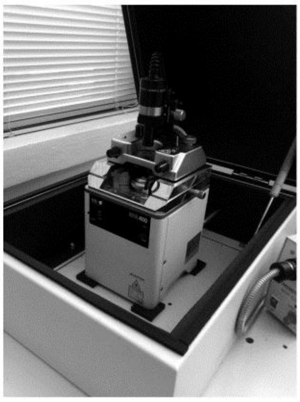

Figure 3.4 Seiko SPA400 AFM installed in a soundproof housing.

As this dissertation is focused on the effect of growth parameters on the size, shape, and density of GaSb nanostructures, atomic force microscopy (AFM) is chosen to probe the nanostructures. A Seiko SPA400 AFM (see Figure 3.4) operated in dynamic mode was used for morphological characterization. AFM tips are made from Si with Al coating on the back side for high laser reflectance, and their radius of curvature is typically less than 8 nm. This AFM is controlled by Spisel32 software. The quality of raw data is improved by noise removal before being analyzed with Gwyddion software.

3.5 Photoluminescence measurement

Optical properties of GaSb nanostructures embedded in the GaAs matrix were investigated by means of photoluminescence (PL) measurement. The temperature- and power-dependent PL measurements were performed in order to prove the crystal quality of GaSb nanostructures grown by droplet epitaxy and examine some unique properties resulting from the type-II band alignment.

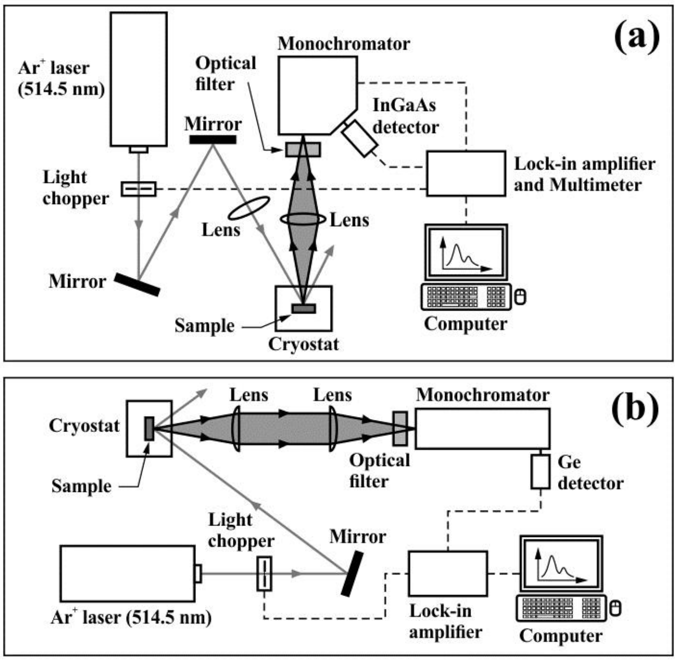

Figure 3.5 Schematics of PL setups at (a) Department of Electrical Engineering, Chulalongkorn University, and (b) Department of Electrical and Computer Engineering, National University of Singapore. The dashed lines represent the electric wires and signal cables.

General PL setup and how to obtain the luminescence from the sample are described as follows. The sample having the size of 3 mm × 5 mm is mounted to the sample holder by thermal grease and placed within a cryostat for precise control of temperature. The sample is excited by an Ar^+ laser having a wavelength of 514.5 nm. The laser beam is focused to the sample by lens until the spot size is ~0.3 mm. The luminescence from the sample is also focused by lens to a monochromator to resolve the wavelengths before coming to a detector. A standard lock-in technique is applied to amplify the luminescence signals. The PL spectra are recorded by a computer. There are two PL systems used in this dissertation, as displayed in Figure 3.5. These setups are very similar. Both InGaAs and Ge detectors are cooled by liquid nitrogen during operation.

Chapter 4

Evolution of Ga droplets into GaSb quantum rings

The main theme of this chapter is the tracking of evolution of Ga droplets into GaSb quantum rings (QRs) by means of reflection high energy electron diffraction (RHEED) and atomic force microscopy (AFM). The gradual transition from the liquid Ga droplets to the crystalline GaSb QRs can be probed by the RHEED patterns and the specular beam intensity since RHEED is very surface sensitive. The crystallization time is varied in order to obtain the snapshots of surface morphology for each stage during crystallization with Sb flux. In addition, the minimum crystallization time for the QR formation can be determined from RHEED and AFM results.

4.1 Experimental details

GaSb QRs were grown on the semi-insulating GaAs (001) substrates by droplet epitaxy using solid-source molecular beam epitaxy. After the oxide desorption at 580 °C under As_4 flux of 8×10^{-6} Torr for 10 min, a 200-nm GaAs buffer layer was grown at 580 °C. At this stage, the RHEED pattern showed a (2×4) reconstruction. Next, the substrate temperature was reduced to 250 °C. Once the substrate temperature reached 250 °C where the RHEED pattern showed a *c*(4×4) reconstruction, the As_4 flux was terminated to deplete the As atmosphere so as to prevent the reaction between Ga and As_4 during the Ga deposition. When the background pressure of the growth chamber was less than 5×10^{-9} Torr, Ga amount of 3 monolayers (ML) (an equivalent amount of 3-ML GaAs grown in the presence of As) was deposited on the substrate at 250 °C with a growth rate of 0.5 ML/s to form the Ga droplets. Then, the Sb_4 flux of 5×10^{-7} Torr was supplied to the droplets at 250 °C for 60 s for crystallization. After that, the substrate was rapidly quenched to room temperature and taken out of the growth chamber. The changes of RHEED pattern and specular beam intensity were observed during the growth. The surface morphology was examined by AFM operated in dynamic mode.

4.2 Results and discussion

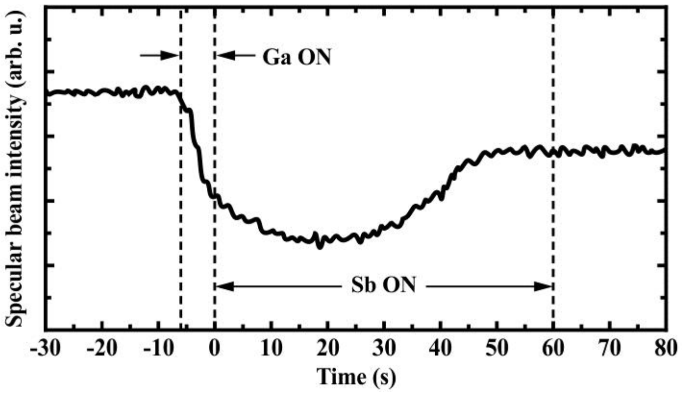

Figure 4.1 Variation of specular beam intensity as a function of time. Ga was deposited for 6 s to form 3-ML Ga droplets, and Sb_4 flux was subsequently supplied for 60 s.

The variation of specular beam intensity during the growth as a function of time is depicted in Figure 4.1. When Ga was deposited on the *c*(4×4) surface at 250 °C, the specular beam intensity drastically dropped because the Ga droplets formed in the Volmer-Weber-like growth mode were in liquid phase. Interestingly, the intensity further decreased at the time that the Sb_4 flux was introduced, and then gradually increased to a saturation value. This phenomenon is different from the case of GaAs nanostructures grown by droplet epitaxy, where the specular beam intensity increases as soon as the Ga droplets were exposed to the As flux [34]. Such a change in the specular beam intensity is similar to the case of the Sb soaking process (before the growth of GaSb/GaAs QDs) where the Sb-for-As exchange reaction takes place [90]. Thus, the drop of intensity at the initial stage of crystallization is attributed to the Sb-for-As exchange reaction. However, the time elapsed from the lowest intensity to the saturated one in the Sb soaking process (~10 s) [90] is much less than the crystallization process (~30 s). This difference is likely due to the existence of the liquid Ga droplets on the surface and the low temperature used in the droplet epitaxy technique, which decelerates the Sb-for-As exchange reaction. From Figure 4.1, the intensity saturated after Sb_4 exposure for ~50 s, implying that the Ga droplets were completely crystallized and transformed into GaSb nanostructures. For this growth condition, the minimum crystallization time is ~50 s. The longer time is necessary to ensure the perfect crystallization. Nevertheless, the long crystallization time may induce the formation of polycrystalline granular Sb layer which is undesirable. To investigate the evolution of the Ga droplets into the GaSb nanostructures, the crystallization time (t_c) was therefore set to 0, 20, 40, and 60 s.

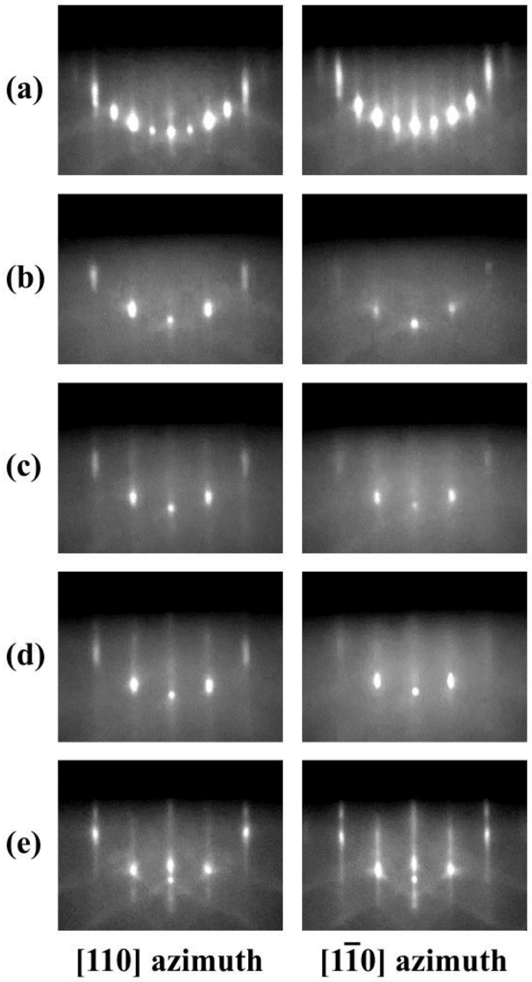

Figure 4.2 RHEED patterns along [110] and $[1\bar{1}0]$ azimuths: (a) before Ga deposition, (b) t_c = 0 s (after Ga deposition), (c) t_c = 20 s, (d) t_c = 40 s, and (e) t_c = 60 s.

Figure 4.2 displays the RHEED patterns along the [110] and $[1\bar{1}0]$ azimuths at each stage of droplet epitaxy. Prior to the Ga deposition, the RHEED pattern showed the *c*(4×4) surface reconstruction (see Figure 4.2(a)). After the Ga amount of 3 ML was deposited on the surface (t_c = 0 s), the pattern became diffused (see Figure 4.2(b)) because of the appearance of liquid Ga droplets. The changes of RHEED patterns after the introduction of the Sb_4 flux are described as follows. At t_c = 20 s, the pattern was featured by the unclear streaks having the small spots (see Figure 4.2(c)). At t_c = 40 s, the intensities of streaks and spots became more explicit (see Figure 4.2(d)). The pattern at t_c = 60 s, as shown in Figure 4.2(e), consisted of the clear streaks having the small spots and the elongated large spots, indicating the formation of ring structures [91], i.e., GaSb QRs on the surface. Such a pattern originates from the reflection/transmission and the diffraction images of the rotational-shaped object [91].

The AFM images with the cross-sectional profiles of the samples grown with various t_c are displayed in Figure 4.3. At t_c = 0 s, the Ga droplets are hemispherical-like and have the average dimensions of 50 nm in diameter and 4.3 nm in height (see Figure 4.3(a)). The density of Ga droplets is ~8×10^9 cm^{-2}. At t_c = 20 s, some small ring structures can be found (see Figure 4.3(b)). Nonetheless, most of the droplets were still not completely crystallized within 20 s. Hence, it is worth considering the changes of the droplet shape under the Sb_4 flux. Compared with the initial droplet in Figure 4.3(a), Figure 4.3(b) reveals that the droplet height became lower, while the droplet base became wider, suggesting that the crystallization firstly occurs at the droplet periphery. Consequently, the Ga atoms tend to diffuse out of the droplet owing to the gradient of Ga atom concentration. At t_c = 40 s, each droplet was transformed into the QR with the nanohole at the center, as shown in Figure 4.3(c). The origin of nanohole can be explained by the Ga droplet etching or Ga nanodrill [92]. When the Ga droplet is formed on the GaAs surface, it dissolves the GaAs surface underneath into Ga and As atoms. Thus, during crystallization, the Ga atoms from the droplet and the dissolved Ga atoms diffuse out of the droplet as above-mentioned. The diffusion of Ga atoms, however, is restricted to around the initial droplet due to the small size of the Ga droplet [93, 94]. That is why each QR consists of the lobe around the nanohole. Since the activation energy for the surface exchange reaction of Sb atoms is lower than that of As atoms, the reaction rate for the Sb-for-As exchange is faster than that for the As-for-Sb exchange (i.e., the reverse reaction) at the same temperature [90]. For this reason, the dissolved As atoms would be replaced by Sb atoms through the Sb-for-As exchange reaction. The Sb-for-As exchange reaction during crystallization also turns the GaAs surface into the GaSb surface [6, 16, 73]. The composition of the QRs may be varied as a result of the surface exchange reaction as well as the thermal-activated diffusion of As atoms from the GaAs layer into the QRs.

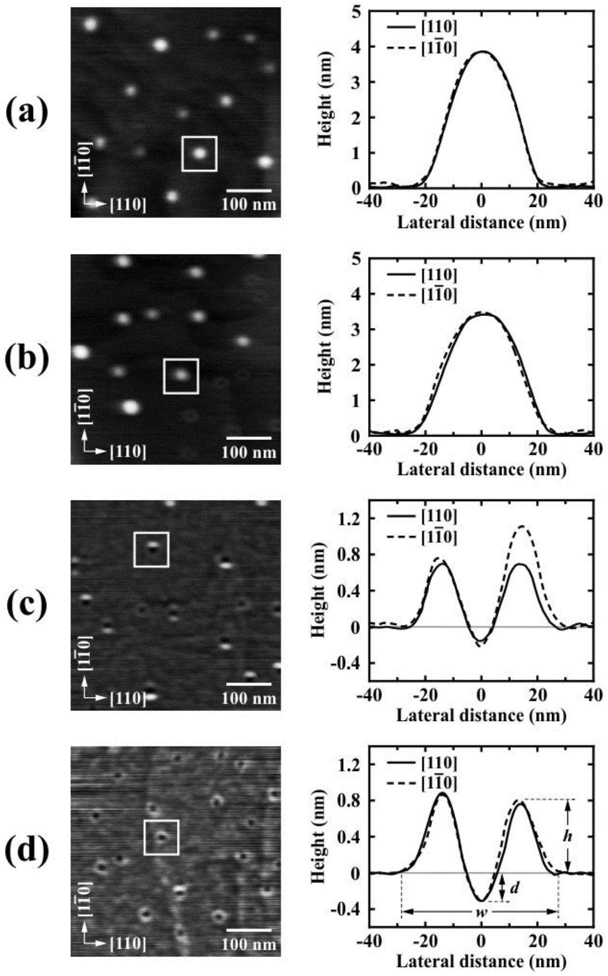

Figure 4.3 AFM images with cross-sectional profiles of selected structures (enclosed by white squares) at different crystallization times: (a) $t_c = 0$ s (3-ML Ga droplets), (b) $t_c = 20$ s, (c) $t_c = 40$ s, and (d) $t_c = 60$ s. The gray lines represent the mean surface level.

It is worth noting that the lobe height along the $[1\bar{1}0]$ direction became lower when t_c was increased from 40 to 60 s (see Figures 4.3(c) and (d)). It can be therefore deduced from this evidence that some portion of the lobe was still in liquid phase at $t_c = 40$ s, which is consistent with the unsaturated specular beam intensity and the unclear RHEED pattern at $t_c = 40$ s. Besides, the nanohole depth became deeper with increasing t_c because there was more time spent on the droplet etching. Since the GaAs surface is changed into the GaSb surface by the Sb-for-As exchange reaction and the diffusion of Ga atoms on the GaSb surface is isotropic [24], the shape of QRs is rather circular, as displayed in Figure 4.3(d). The average values of QR outer dimension (*w*), height (*h*), and depth (*d*), measured along the [110] direction, are 58.4 ± 2.7, 0.6 ± 0.2, and 0.3 ± 0.1 nm, respectively. The density of GaSb QRs is $\sim 8\times10^9$ cm^{-2} which is equivalent to the density of Ga droplets, suggesting that all Ga droplets were transformed into the GaSb QRs at the end of crystallization.

Chapter 5

Optical properties of GaSb/GaAs quantum rings

This chapter is concentrated on the optical properties of GaSb/GaAs quantum rings (QRs). It should be noted that the QRs in Chapter 4 seem to be too small for studying the optical properties by the photoluminescence (PL) measurement at which the QRs are capped with a GaAs layer. Importantly, the strong As-for-Sb exchange reaction during the capping process can wipe out the small QRs. For this reason, a larger QR size is required. Increasing the substrate temperature for droplet deposition is an easy way to obtain large QRs. The formation mechanism of the QRs is concisely described in this chapter. The temperature- and power-dependent PL measurements are performed to probe the carrier dynamics and the characteristics of the type-II band alignment.

5.1 Experimental details

GaSb QRs were grown on semi-insulating GaAs (001) substrates by droplet epitaxy using solid-source molecular beam epitaxy. After the desorption of the native oxide at 580 °C under the $\mathrm{As_4}$ flux of 8×10^{-6} Torr for 10 min, a 300-nm GaAs buffer layer was grown at 580 °C. Next, the substrate temperature (T_s) was reduced to 300 °C under the $\mathrm{As_4}$ flux. When T_s = 300 °C, the $\mathrm{As_4}$ flux was stopped supplying in order to eliminate the As atmosphere in the growth chamber. After that, it was needed to wait until the background pressure of the growth chamber was less than 5×10^{-9} Torr to prevent the initial reaction between Ga and $\mathrm{As_4}$ during the Ga deposition. The Ga amount of 3 monolayers (ML) (an equivalent amount of 3-ML GaAs grown under the As pressure) was then deposited on the substrate surface at T_s = 300 °C, where the reflection high energy electron diffraction (RHEED) showed a clear *c*(4×4) pattern, with a rate of 0.5 ML/s to form the liquid Ga droplets. Subsequently, T_s was lowered to 250 °C and the $\mathrm{Sb_4}$ flux of 5×10^{-7} Torr was irradiated to the substrate surface for 90 s so as to crystallize the droplets into the GaSb QRs. The formation of GaSb QRs after crystallization was indicated by the RHEED pattern featured by the streaks and spots [91]. Finally, the sample was rapidly cooled down to room temperature. To confirm the existence of the Ga droplets after Ga deposition, another sample was provided by stopping the growth just after the Ga deposition at T_s = 300 °C without crystallization. Morphology of the Ga droplets and the GaSb QRs was investigated by atomic force microscopy (AFM) operated in dynamic mode.

For the PL study, the GaSb QRs were capped with a 20-nm GaAs layer at T_s = 250 °C (right after crystallization) to suppress the As-for-Sb exchange reaction which may annihilate the QRs, and an additional 130-nm GaAs layer at T_s = 450 °C. A 514.5-nm line Ar^+ laser having a spot size of ~0.3 mm was used as an excitation source. The PL emission was detected by a cooled Ge detector. The temperature- and power-dependent PL measurements were also carried out.

5.2 Results and discussion

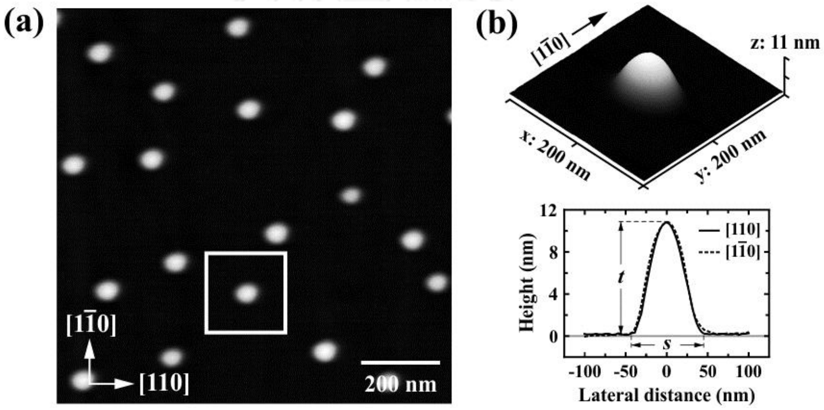

Figure 5.1 (a) AFM image of Ga droplets. (b) Three-dimensional AFM image of a single Ga droplet (enclosed by a white square) with its cross-sectional profiles. The gray line represents the mean surface level.

Figure 5.1(a) shows an AFM image of Ga droplets having the density of ~1.8×10^{9} cm^{-2}. A three-dimensional (3D) AFM image of a single Ga droplet and its cross-sectional profiles along [110] and [1$\bar{1}$0] directions are depicted in Figure 5.1(b). The average droplet size is ~94 nm in diameter (*s*) and ~10.6 nm in height (*t*). After the Ga droplets were exposed to the Sb_4 flux of 5×10^{-7} Torr for 90 s, the GaSb QRs were formed on the surface, as confirmed by the AFM image in Figure 5.2(a) as well as the RHEED pattern consisting of streaks and spots. To make a closer look at the GaSb QR, the 3D AFM image of a single GaSb QR and its cross-sectional profiles are provided in Figure 5.2(b). The average QR size is ~96 nm in diameter (*w*) and ~1.3 nm in depth (*d*). Compared with the original droplet, the larger average QR diameter indicates the outward diffusion of Ga atoms. Since the density of GaSb QRs is equivalent to the density of Ga droplets, it can be deduced that all Ga droplets evolved into the GaSb QRs after crystallization with the Sb_4 flux.

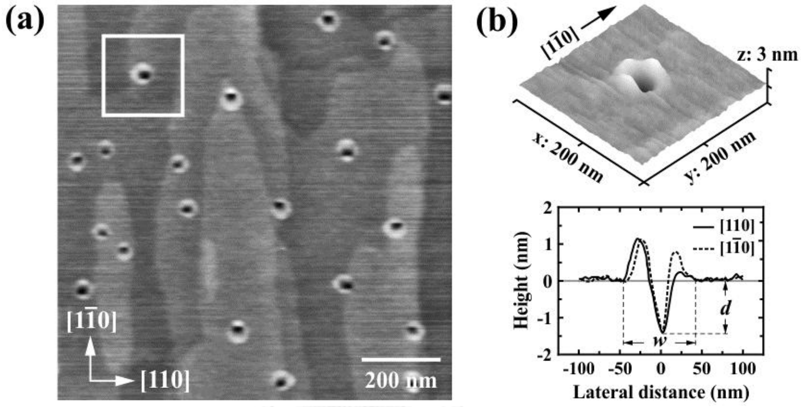

Figure 5.2 (a) AFM image of GaSb QRs. (b) Three-dimensional AFM image of a single GaSb QR (enclosed by a white square) with its cross-sectional profiles. The gray line represents the mean surface level.

The formation mechanism of the GaSb QR can be explained by the diffusion of Ga atoms from the initial Ga droplet. When Ga is deposited on the *c*(4×4) GaAs surface, the liquid Ga droplets are formed in the Volmer-Weber-like growth mode. It results in a Ga-rich region at the interface between the Ga droplet and the GaAs surface. The GaAs surface underneath the droplet is therefore dissolved into Ga and As atoms. Since the Sb_4 flux intensity used for the crystallization is not high, the growth of GaSb nanocrystals at the droplet periphery has a higher rate than other parts and acts as the nucleation seed for the further GaSb growth. Because of the gradient of Ga atom concentration, Ga atoms from both the initial Ga droplet and the dissolved Ga atoms diffuse out of the droplet and react with the Sb_4 flux, giving rise to the lobe around the nanohole (see Figure 5.2). The dissolved As atoms would be replaced by the Sb atoms due to the Sb-for-As exchange reaction [16]. Besides, the Sb-for-As exchange reaction turns the GaAs surface into the GaSb surface during crystallization. The shape of GaSb QRs is quite circular as a result of the isotropic diffusion of Ga atoms on the GaSb surface [24].

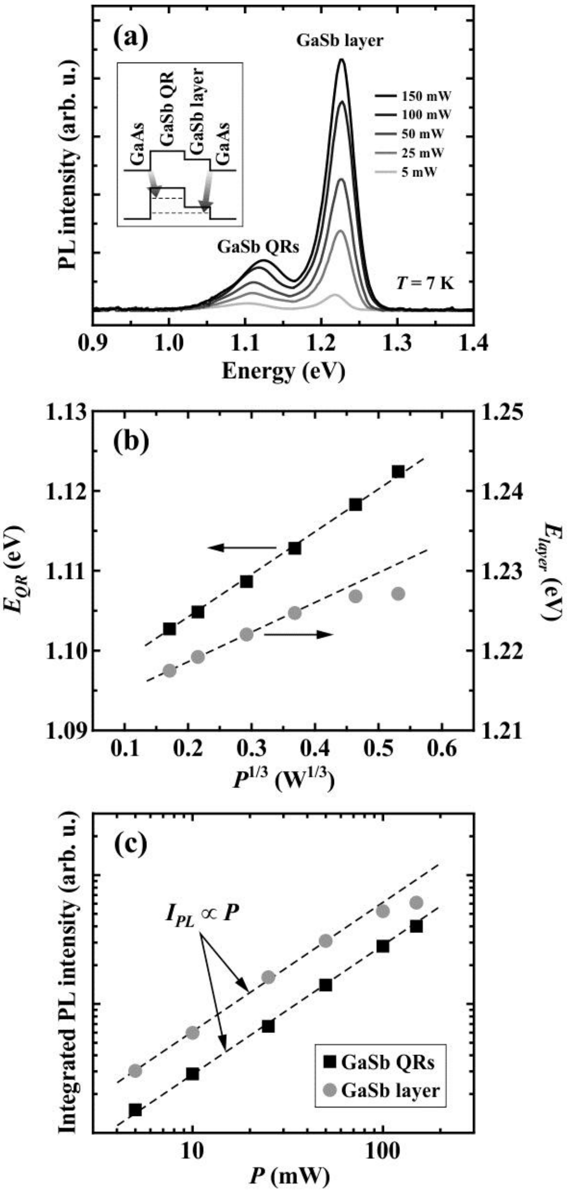

Figure 5.3 (a) Power-dependent PL spectra at 7 K. The inset shows a schematic diagram of band alignment. (b) A plot of E_{QR} and E_{layer} as a function of the third root of excitation power. The dashed straight lines are guide for the eyes. (c) A log-log plot of integrated PL intensity as a function of the excitation power.

Figure 5.3(a) displays the power-dependent PL measured at 7 K. The variation range of peak energy is around 1.103-1.122 eV for the GaSb QRs and 1.217-1.227 eV for the GaSb layer originating from the Sb-for-As exchange reaction during crystallization, as previously explained. The excitation power (*P*) was varied from 5 to 150 mW. It is worth noticing that the PL peak energies of GaSb QRs (E_{QR}) and GaSb layer (E_{layer}) shift to higher energies with increasing the excitation power (see Figure 5.3(a)). This is a characteristic of the type-II band alignment [5] and can be described as follows. Holes confined in the GaSb region induce electrons in the GaAs region to stay at the GaSb/GaAs interface. As a result, an internal electric field appears at the GaSb/GaAs interface and bends the conduction band into a triangular quantum well, giving rise to the quantization energy levels for electrons [73]. The increase in the excitation power enhances the accumulation of photo-generated carriers as well as the internal electric field at the interface, resulting in the further bending in the conduction band and hence the raising up of electron quantization energy [73]. That is why the blueshift in both E_{QR} and E_{layer} takes place when the excitation power increases. According to the band-bending model, the electron quantization energy would increase proportionally with the third root of excitation power [73]. The plot of E_{QR} and E_{layer} as a function of the third root of excitation power ($P^{1/3}$) is shown in Figure 5.3(b). The dependence of integrated PL intensities (I_{PL}) of GaSb QRs and GaSb layer on the excitation power is displayed in Figure 5.3(c). As expected, E_{QR} increases linearly with $P^{1/3}$. Furthermore, the PL intensity of GaSb QRs is linearly dependent on the excitation power, implying that the carrier loss through the non-radiative recombination processes is negligible. It is noteworthy that E_{layer} becomes saturated when $P > 50$ mW. This saturation behavior also appears in the PL intensity of GaSb layer. Such phenomena have been observed in the GaSb wetting layer (WL) in the growth of GaSb/GaAs quantum dots (QDs) by Stranski-Krastanov method and are attributed to the reduction in the oscillator strength by screening within the 2D electron-hole plasma [7].

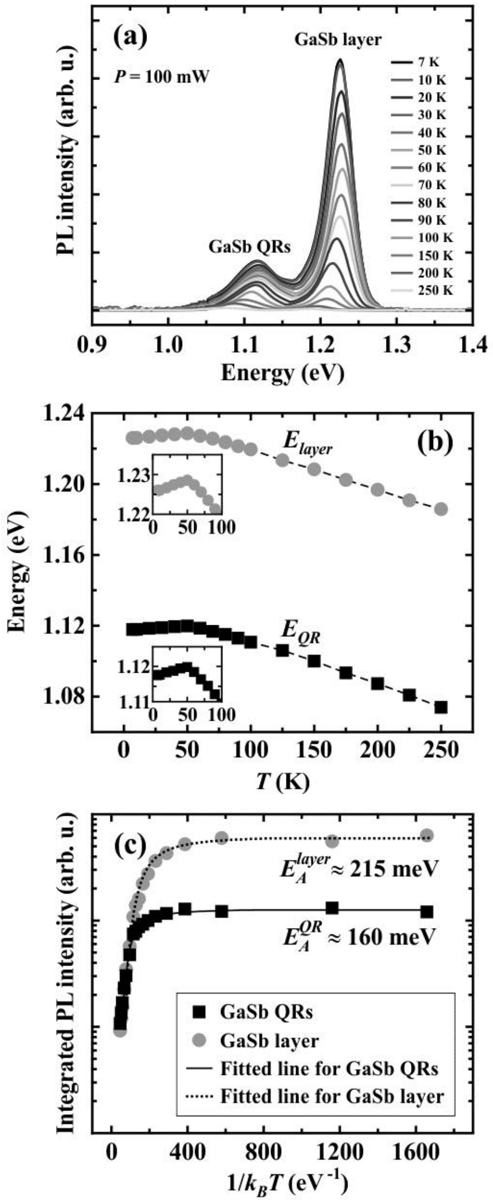

Figure 5.4 (a) Temperature-dependent PL spectra obtained by using the excitation power P = 100 mW. (b) A plot of E_{QR} and E_{layer} as a function of temperature. The dashed lines show the trend of variation. The insets are the magnified view in the temperature range of 0-100 K. (c) An Arrhenius plot of integrated PL intensity with the activation energy fit.

The temperature-dependent PL spectra taken by using P = 100 mW are displayed in Figure 5.4(a). The PL spectra can be distinctly detected up to 250 K. However, the observation of PL emissions at high temperatures reflects a good crystal quality. Figure 5.4(b) shows the dependence of E_{QR} and E_{layer} on temperature (T). Both E_{QR} and E_{layer} exhibit a blueshift in the temperature range of 7-50 K and follow the band gap temperature dependence at high temperatures owing to the cumulative effects of the electron-phonon interaction and the thermal lattice expansion. The blueshift occurring in the low temperature range is another characteristic of the type-II band alignment and can be explained by a higher population of thermal-excited carriers, leading to the steeper triangular quantum well where the electron quantization energy is lifted up [73]. An Arrhenius plot of PL intensities of GaSb QRs and GaSb layer is depicted in Figure 5.4(c). The temperature dependence of integrated PL intensity can be expressed by

$$I_{PL}(T) = \frac{I_0}{1 + C\exp(-E_A / k_B T)} \tag{5.1}$$

where I_0 is the integrated PL intensity at 0 K, C is the constant, E_A is the thermal activation energy, and k_B is the Boltzmann constant. An activation energy of ~160 meV is obtained for the GaSb QRs (E_A^{QR}) and ~215 meV for the GaSb layer (E_A^{layer}). It is clear that E_A^{layer} conforms to the calculated hole confinement energy of ~207 meV for the GaSb WL which is a similar structure to the GaSb layer [7], indicating that the PL quenching arises from the thermal escape of holes. From the carrier confinement point of view, the QRs confine the carriers in all three spatial directions like the QDs [41]. Thus, the GaSb QRs should have a larger activation energy than the GaSb layer. Nonetheless, E_A^{QR} is found to be less than E_A^{layer}, implying that there should be a carrier transfer between the GaSb QRs and the GaSb layer. Figure 5.4(c) reveals that the PL intensity of the GaSb layer decreases at the same time that the PL intensity of the GaSb QRs increases at T = 175 K ($1/k_B T \approx 66$ eV^{-1}), suggesting that the thermally escaped holes from the GaSb layer become captured into the GaSb QRs, and then contribute to the emission of the QRs. That is why the PL intensity of the GaSb QRs drops slower than that of the GaSb layer.

Chapter 6

Effect of Ga amounts on GaSb/GaAs nanostructures

Group-III amount is one of the key growth parameters in droplet epitaxy. Under the same group-V flux intensity and substrate temperature, a higher group-III amount results in larger III-V nanostructures (NSs). In this chapter, it can be expected that the higher Ga amount should lead to the larger GaSb quantum rings (QRs) after crystallization with low Sb flux. The experimental results, however, suggest that an increase in the Ga amount gives rise to the NSs like the quantum dots (QDs) instead of the larger QRs. The possible formation mechanisms for such nanostructures are discussed here. The photoluminescence (PL) measurement is also carried out.

6.1 Experimental details

All samples were grown on semi-insulating GaAs (001) substrates by droplet epitaxy using solid-source molecular beam epitaxy. After the desorption of the native oxide at 580 °C under the As_4 flux of 8×10^{-6} Torr for 10 min, a 300-nm GaAs buffer layer was grown. The substrate temperature was then lowered to 260 °C and the As_4 flux was stopped supplying to deplete the As atmosphere. Once the background pressure of the growth chamber was less than 5×10^{-9} Torr, the desired Ga amount was deposited on the substrate surface at 260 °C with a rate of 0.5 monolayers (ML)/s to form the liquid Ga droplets. In this work, Ga amounts of 3, 4, and 5 ML were chosen (referred as samples A, B, and C, respectively). Here, 1-ML Ga is defined as an equivalent 1-ML GaAs grown under the As flux. To obtain the GaSb NSs, the droplets were crystallized by supplying the Sb_4 flux of 5×10^{-7} Torr at 250 °C for 90 s. Finally, the sample was either rapidly quenched to room temperature or capped with a 150-nm GaAs layer for the PL measurement. The details of the capping process have been mentioned in Chapter 5. The surface morphology was investigated by atomic force microscopy (AFM) operated in dynamic mode. The PL measurement was performed by using a 514.5-nm line Ar^+ laser having a spot size of ~0.3 mm and a cooled InGaAs detector.

6.2 Results and discussion

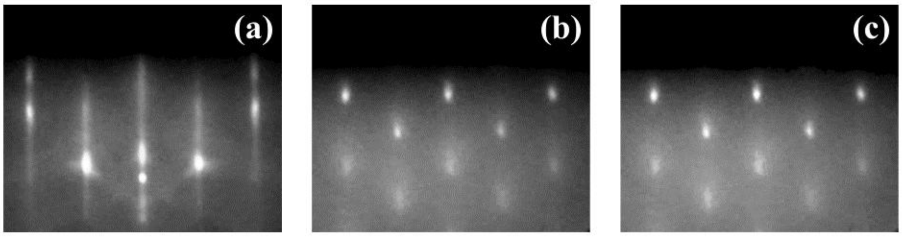

Figure 6.1 RHEED patterns after crystallization of (a) sample A, (b) sample B, and (c) sample C.

At the substrate temperature of 260 °C, the reflection high energy electron diffraction (RHEED) pattern showed a *c*(4×4) As-stabilized surface. Once Ga was deposited on the surface, the RHEED pattern became diffused as a result of the appearance of liquid Ga droplets. Interestingly, when the Sb_4 flux was introduced, the RHEED pattern of sample A slowly developed into the streaks and spots (~50 s), while the patterns of samples B and C became spotty after supplying the Sb_4 flux for ~10 s. It suggests that the large Ga droplets are crystallized faster than the small ones. The RHEED patterns after crystallization of all samples are shown in Figure 6.1. The RHEED pattern of sample A, which consists of the streaks and spots, reflects the formation of QRs [91]. The patterns of samples B and C are featured by the spots only, implying that there should be the QDs on the surface.

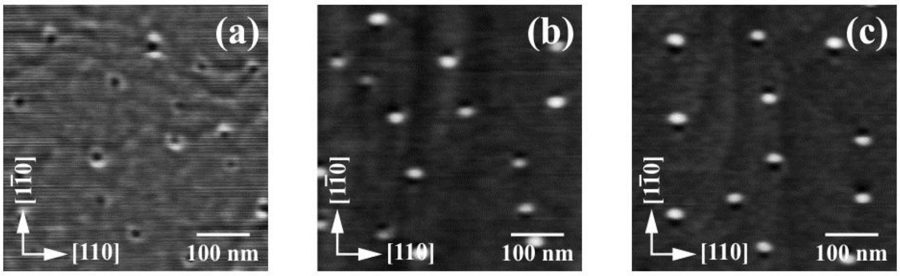

Figure 6.2 AFM images of GaSb NSs in (a) sample A, (b) sample B, and (c) sample C.

The AFM images displayed in Figure 6.2 reveal that QRs are obtained in sample A, whereas each NS in samples B and C consists of the thin QR lobe and the QD placing at the nanohole edge. The densities of GaSb NSs for samples A, B, and C are ~7.2×10^9, ~6.0×10^9, and ~4.5×10^9 cm^{-2}, respectively. It is clear that the density of GaSb NSs decreases with increasing the Ga amount. This observation is attributed to the coalescence of the initial Ga droplets, which can take place at high Ga amount to reduce the surface energy.

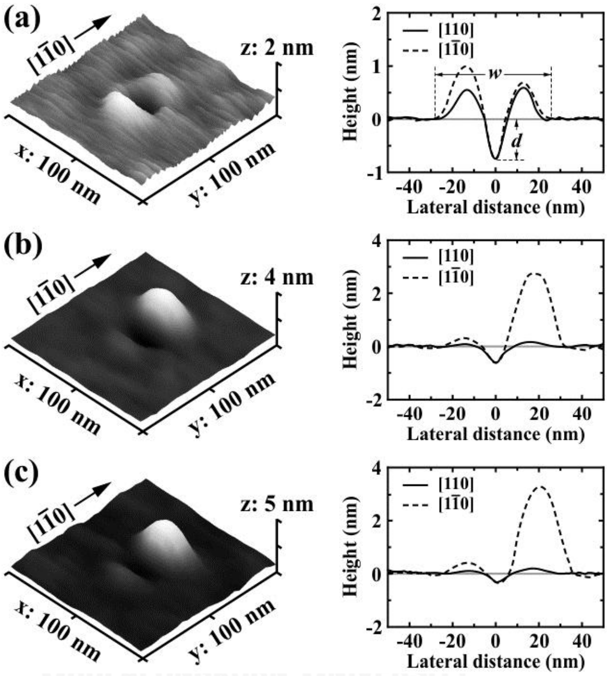

Figure 6.3 Three-dimensional AFM images of individual GaSb NSs with cross-sectional profiles of (a) sample A, (b) sample B, and (c) sample C. The gray lines represent the mean surface level.

To make a closer look at the GaSb NSs, three-dimensional AFM images with cross-sectional profiles of individual NSs are taken and depicted in Figure 6.3. It is obvious that, for samples B and C, the QR lobe height is much lower than the QD height. That is why the RHEED patterns of samples B and C are spotty. For sample A, the formation mechanism of the QR which is the lobe around the nanohole can be described by the outward diffusion of Ga atoms from the initial droplet and the droplet etching. Like sample A, the droplet etching causes the nanoholes in samples B and C. Since the compressive strain due to the lattice mismatch between GaSb and GaAs is built up and stored in the GaSb nanocrystals, the formation of the QDs in samples B and C would be responsible for the strain relaxation [24]. It is noteworthy that the QRs in sample A possess the nearly uniform lobes without the QDs, suggesting that the strain stored in the GaSb QRs does not exceed a critical value.

According to the AFM results, the average NS diameters (*w*) measured along the $[1\bar{1}0]$ direction for samples A, B, and C are 53.9, 60.0, and 65.8 nm, respectively. It is apparent that the NS diameter increases with the Ga amount because of the increase in the initial droplet size. The average NS depths (*d*) are 0.76, 0.64, and 0.39 nm for samples A, B, and C, respectively. The NS depth decreases with increasing the Ga amount because the large Ga droplet tends to be crystallized faster than the small one, resulting in the less time spent in the droplet etching [95]. The variations of NS diameter and depth are thus opposed to each other, as seen in Figure 6.4.

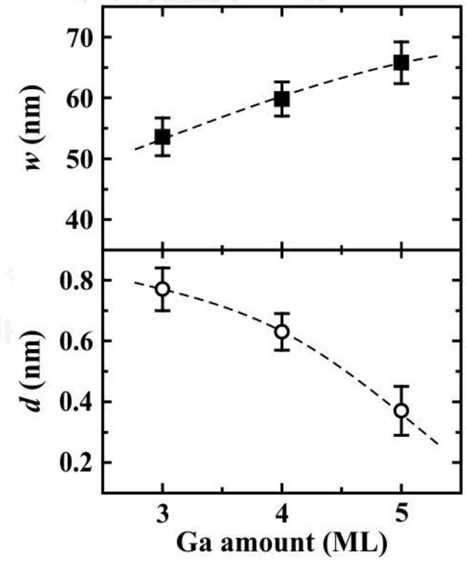

Figure 6.4 Dependence of NS diameter (*w*) and depth (*d*) on Ga amount. The dashed lines show the trend of variation.

Due to the Sb-for-As exchange reaction, the GaAs surface is transformed into the GaSb surface during crystallization. Since the diffusion of Ga atoms on GaSb surface is isotropic [24], the shape of NSs in all samples should be circular. Nevertheless, only QRs in sample A show the circular shape. The NSs in the other samples are somewhat elongated in the $[1\bar{1}0]$ direction and the elongation is more pronounced when the Ga amount increases (see Figures 6.3(b) and (c)). From these results, it is highly possible that the time taken to form the GaSb surface through the Sb-for-As exchange reaction would affect the shape of GaSb NSs. If the GaSb surface does not mainly occur at the same time that the droplets begin to be crystallized, most Ga atoms have to diffuse on the GaAs surface where the $[1\bar{1}0]$ direction is preferred. The shape of NSs is thus elongated in the $[1\bar{1}0]$ direction and the QD tends to grow in this direction where the GaSb nanocrystals accumulate. Apart from the diffusion, the NS shape in the lattice-mismatched system is determined by the balance between strain energy and surface energy. The NS consisting of one QD with thin QR lobe would be the shape that minimizes the total energy of the system. The above condition along with the explanations is consistent with the AFM results in samples B and C (see Figures 6.3(b) and (c)). On the other hand, if most Ga atoms diffuse from the Ga droplet after the GaSb surface is greatly formed, the diffusion of Ga atoms becomes isotropic, resulting in the circular shape of NSs as found in the QRs in sample A. The evidence supporting such descriptions is the change of RHEED patterns of samples B and C at which the spotty patterns quickly appeared after the introduction of Sb_4 flux, while the RHEED pattern of sample A took a long time to develop into the streaks and spots.

The normalized PL spectra measured at 20 K are depicted in Figure 6.5(a). The GaSb NS peaks for samples A, B, and C are at 1.121, 1.092, and 1.079 eV, respectively. The NS peak shifts to the lower energy as a result of the larger NS size when the Ga amount increases. Since samples B and C contain both thin QR lobes and large QDs, there should be two separate PL peaks from NSs. In contrast to the expectation, only one peak from the GaSb NSs is observed from samples B and C, implying that the thin lobes might be annihilated by the As-for-Sb exchange reaction during capping [17, 96] and the NS peak is attributed to the GaSb QDs. Another peak at 1.227 eV originates from the GaSb layer caused by the Sb-for-As exchange reaction during crystallization. The dependence of the PL peak energy of GaSb NSs (E_{NS}) on the third root of excitation power ($P^{1/3}$) is shown in Figure 6.5(b). It is found that E_{NS} increases with the excitation power because more photo-generated carriers induce the steeper triangular quantum well at the GaSb/GaAs interface, leading to the rise of electron quantization energy [5]. Furthermore, E_{NS} is linearly dependent on $P^{1/3}$, which is the characteristic of type-II band alignment [73].

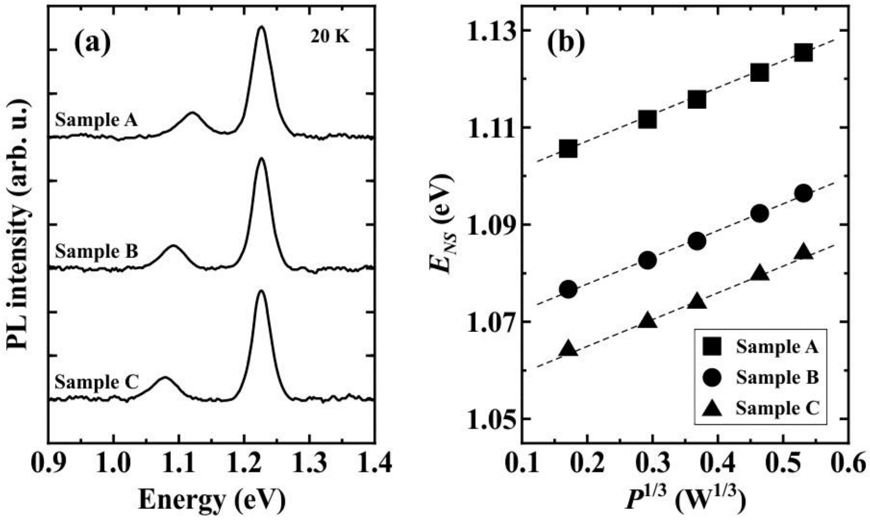

Figure 6.5 (a) Normalized PL spectra of GaSb NSs at 20 K. (b) Variations of GaSb NS peak energies measured at 20 K as a function of the third root of excitation power. The dashed straight lines are guide for the eyes.

Chapter 7

Effect of Ga deposition rates on GaSb/GaAs nanostructures

In general, the diffusion behavior of group-III atoms out of the original droplet during crystallization with group-V flux is different for different droplet sizes. The droplet size and density can be changed by the group-III deposition rate. For droplet epitaxy in the GaSb/GaAs system, the variation of Ga deposition rate gives rise not only to a GaSb quantum ring (QR) but also to a complex nanostructure, a GaSb QR surrounded by ring-shaped quantum dot molecules (R-QDMs) after crystallization with Sb flux. A simple descriptive model is consequently proposed in this chapter to explain the formation mechanisms. This model relies on the Ga droplet size, distance between Ga droplets, and diffusion area of Ga atoms during crystallization. Besides, the mismatch strain is a key factor in the origin of R-QDMs. The photoluminescence (PL) measurement is performed to verify the model.

7.1 Experimental details

All samples were grown on semi-insulating GaAs (001) substrates by droplet epitaxy using solid-source molecular beam epitaxy. After the surface oxide desorption at 580 °C under As_4 flux of 8×10^{-6} Torr for 10 min, a 300-nm GaAs buffer layer was grown at 580 °C where the reflection high energy electron diffraction (RHEED) pattern showed a clear (2×4) As-stabilized surface. Then, the substrate temperature was reduced to 300 °C under As_4 flux. When the substrate temperature was stable at 300 °C, the RHEED pattern showed a sharp *c*(4×4) As-stabilized surface. To prevent the initial reaction between Ga and As_4 during droplet formation, the As_4 flux was terminated in order to eliminate As in the growth chamber. Once the background pressure was less than 5×10^{-9} Torr, a constant Ga amount of 3 monolayers (ML) (an equivalent amount of 3-ML GaAs grown under the presence of As) was deposited at 300 °C to form Ga droplets with different Ga deposition rates of 0.1, 0.2, 0.3, and 0.5 ML/s (labeled as samples A, B, C, and D, respectively). During Ga deposition stage, the RHEED pattern became diffused and changed from *c*(4×4) to halo patterns since the Ga droplets were in liquid phase. After that, the Sb_4 flux of 5×10^{-7} Torr was supplied to the droplets at 250 °C for 90 s. During this stage, the RHEED pattern was gradually clear and the pattern after 90-s Sb exposure consisted of streaks and spots. Such a pattern reflects the existence of ring-shaped nanostructures on the surface [91]. Finally, the sample was immediately quenched to room temperature. For PL study, another set of sample was fabricated with the same procedures. GaSb nanostructures were then capped by a 150-nm GaAs layer (see more details in Chapter 5). The surface morphology of all samples was investigated by AFM operated in dynamic mode. The PL measurement was carried out at 20 K with a 100-mW Ar$^+$ laser having a spot size of ~0.3 mm and a cooled InGaAs detector.

7.2 Results and discussion

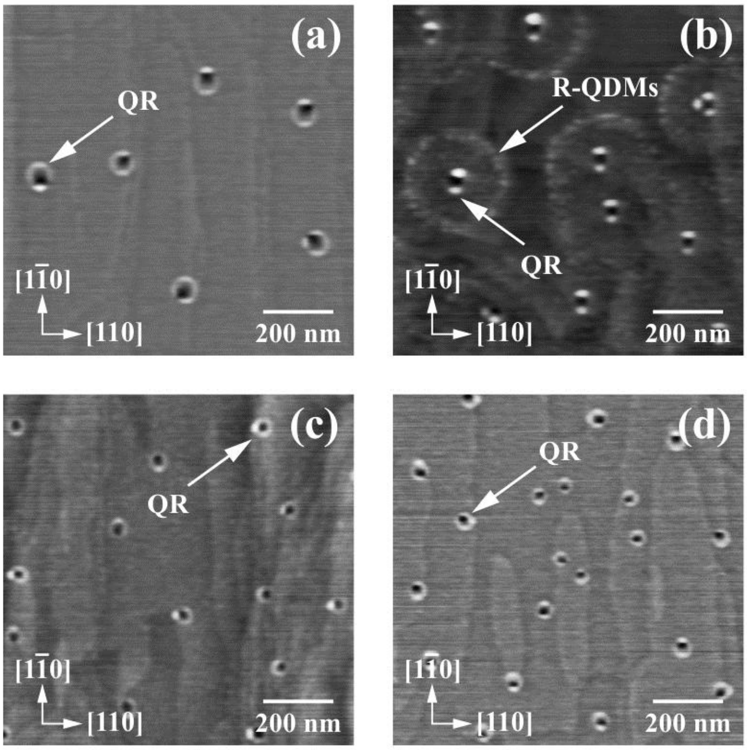

Figure 7.1 AFM images of GaSb nanostructures in (a) sample A, (b) sample B, (c) sample C, and (d) sample D.

Figure 7.1 shows the AFM images of GaSb nanostructures grown with various Ga deposition rates. Here, the GaSb nanostructures are classified into two types. One is the QR which is found in samples A, C, and D. The other is the QR surrounded by

R-QDMs, which is observed in sample B. Because of the low growth temperature in droplet epitaxy technique, the desorption of Ga atoms from the surface can be neglected. Therefore, the density of GaSb nanostructures would be equivalent to that of initial Ga droplets. The densities of GaSb nanostructures of samples A, B, C, and D are 6×10^8, 1.1×10^9, 1.3×10^9, and 1.8×10^9 cm^{-2}, respectively. It is obvious that the density increases with the Ga deposition rate. Since the diffusion length of adatoms decreases with increasing of the deposition rate, the density of original droplets and hence the density of GaSb nanostructures increase with the Ga deposition rate.

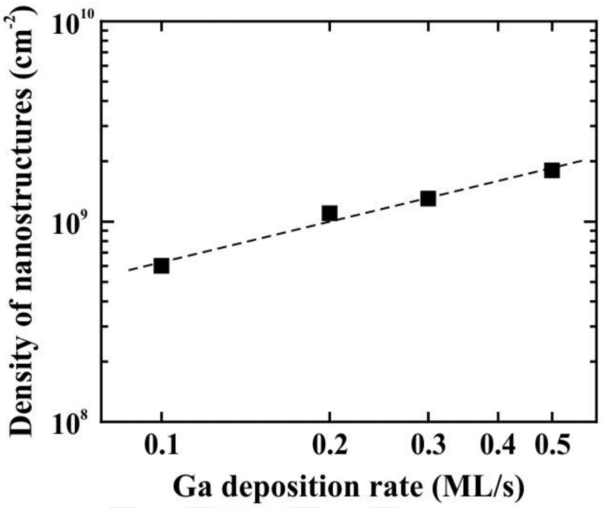

Figure 7.2 Density of GaSb nanostructures plotted as a function of Ga deposition rate in a log-log graph. The dashed line represents least-squares fit to the data.

According to the nucleation theory [26], the maximum cluster density can be expressed by $n_x \propto (F/v)^p \exp(E_x/k_BT)$ where F is the deposition rate, v is the atomic vibration frequency, p is the value depending on the number of atoms in a critical cluster, E_x is the energy related to the atomistic processes during nucleation stage, k_B is the Boltzmann constant, and T is the temperature. The values of p and E_x for 2D and 3D islands at different condensation regimes have been reported in Chapter 2. Since the Ga deposition rate was varied, while the other growth parameters were not changed, the relation between the density of GaSb nanostructures and the Ga deposition rate should follow a power law. In this case, 3D islands and complete condensation regime are most important. Thus, $p = i/(i+2.5)$ where i is the critical cluster size [27]. In Figure 7.2, the density of GaSb nanostructures is plotted as a function of the Ga deposition rate in a log-log graph. It is clear that the results are in good agreement with the power law as expected and a slope of the log-log graph obtained by fitting the data is equal to the p value. The slope of a dotted line in Figure 7.2 is $p = 0.67 \pm 0.06$, suggesting that the number of Ga atoms containing in the critical cluster is $i = 5$. In other words, all Ga clusters containing more than 5 atoms are stable and grow into the Ga droplets.

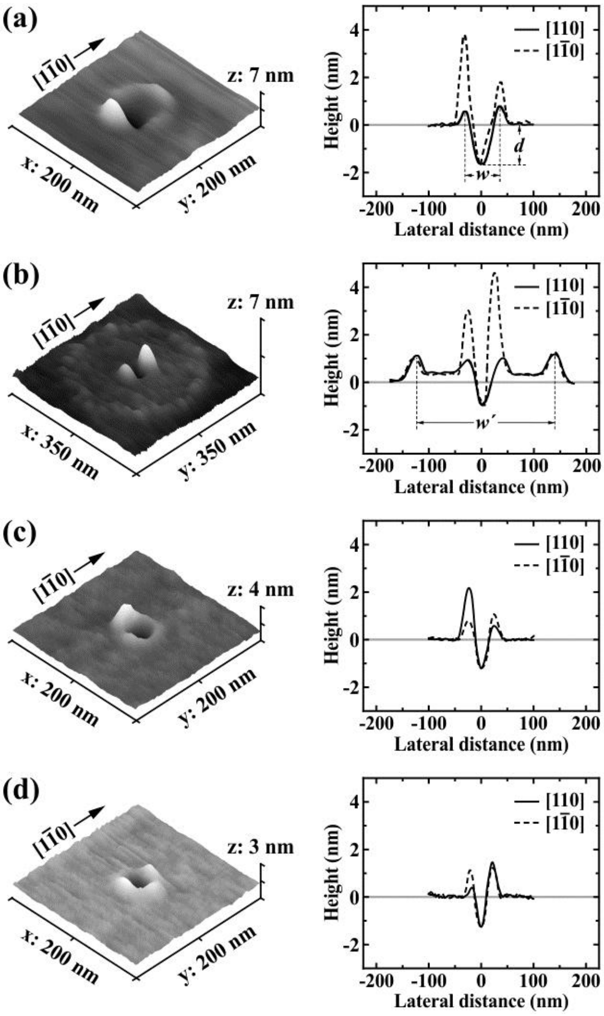

Figure 7.3 Three-dimensional AFM images of individual GaSb nanostructures with cross-sectional profiles of (a) sample A, (b) sample B, (c) sample C, and (d) sample D. The gray lines represent the mean surface level.

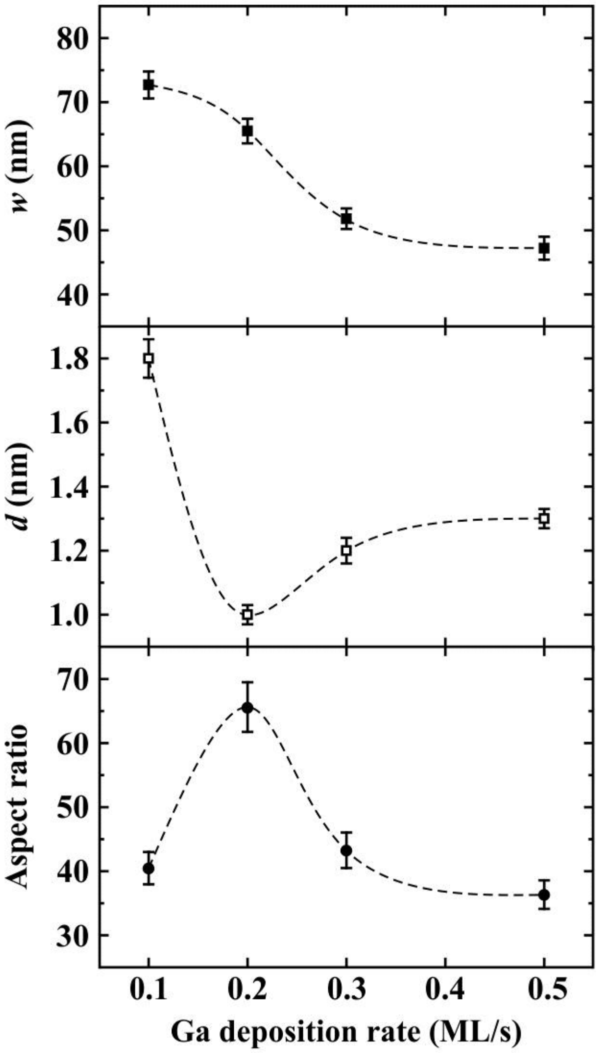

Figure 7.4 Dependence of QR width (*w*), depth (*d*), and aspect ratio (*w*/*d*) on Ga deposition rate. The dashed lines represent the trend of variation.

The origin of the GaSb QR can be explained by the diffusion of Ga atoms out of the droplet and the nanohole at the center of the QR is derived from the droplet etching. The three-dimensional AFM images of individual GaSb nanostructures with cross-sectional profiles along both [110] and $[1\bar{1}0]$ directions are depicted in Figure 7.3. The average values of QR diameter (*w*) along the [110] direction of samples A, B, C, and D are 72.7, 65.5, 51.8, and 47.2 nm, respectively. Due to the fact that the ratio between the diffusion length of adatoms and the deposition rate becomes smaller when the deposition rate is higher, the QR diameter decreases with increasing the Ga deposition rate. The average value of R-QDMs diameter (*w*´) is about 240 nm. The formation of the complex structure, GaSb QR surrounded by R-QDMs, will be discussed later. Because of the Sb-for-As exchange reaction, the diffusion of Ga atoms out of the Ga droplet during crystallization should be considered as the diffusion of Ga atoms on a GaSb surface, not a GaAs surface. Both the QR and the R-QDMs are thus circular as a result of the isotropic diffusion of Ga atoms on the GaSb surface [24]. It is worth noticing on Figure 7.1 that QR lobes in all samples are not uniform and some portion of QR lobe breaks up into some kind of quantum dot (QD) at the edge of nanohole. This would be the way to reduce the strain energy caused by the lattice mismatch between GaSb and GaAs [24]. However, the QD is not formed all around the nanohole edge and the QR is still in the circular shape. There is a flat region between the QR and the R-QDMs (see Figure 7.3(b)), and its thickness is higher than the mean surface level. Hereafter, the flat region will be called a GaSb disk.

In general, it has been observed that the smaller QR has the deeper nanohole at the center [95]. This phenomenon can be described by the dependence of solubility on the particle size. Under the same temperature, the large particle has a lower saturating concentration than the small one [95]. It implies that the large Ga droplet can be crystallized at low Sb concentration, whereas the small Ga droplet will be crystallized later at high Sb concentration. The possibility of the crystallization of the large Ga droplet is therefore higher than that of the small one, suggesting that the time spent in the droplet etching process, which leads to the QR depth, is less in the large Ga droplet and more in the small one. For this reason, the large diameter QR possesses the shallow QR depth, whereas the small diameter QR possesses the deep one. Nevertheless, there may be other factors governing this phenomenon. From Figure 7.3, the average values of QR depth (d) of samples A, B, C, and D are 1.8, 1.0, 1.2, and 1.3 nm, respectively. The dependence of w, d, and aspect ratio (w/d) on the Ga deposition rate is plotted in Figure 7.4. The variation of w follows the dependence of diffusion length on the Ga deposition rate as described before (see Figure 7.4). It is apparent that the variations of d and aspect ratio in Figure 7.4 do not follow the mechanism related to the solubility, which has just been discussed, all over the range of Ga deposition rates. Such a mechanism predicts that d should increase and the aspect ratio should decrease with increasing the Ga deposition rate, respectively. In fact, this mechanism holds true throughout the range of Ga deposition rates but other factors, such as the diffusion area of Ga atoms during crystallization and the distance between Ga droplets, are needed to be taken into account.

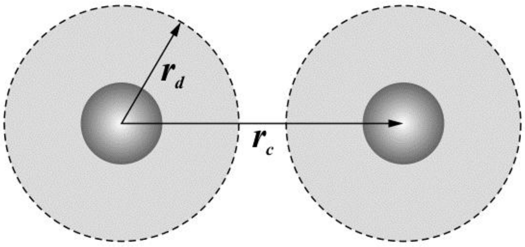

Figure 7.5 Schematic diagram for defining the radius of diffusion area (r_d) and the distance between the centers of Ga droplets (r_c) in the model.

Since the Ga deposition rate was only varied, a simple descriptive model based on the size and density of Ga droplets and the diffusion behavior of Ga atoms during crystallization is proposed. Assume that the diffusion area of Ga atoms has a radius of r_d and the distance between the centers of Ga droplets is r_c, as illustrated in Figure 7.5. If $2r_d < r_c$ and the Ga droplet is small, then the diffusion of Ga atoms will be restricted to the small region around the droplet, resulting in the GaSb QR. When the Ga droplet is larger but $2r_d < r_c$, the diffusion of Ga atoms becomes larger, leading to the GaSb QR having larger diameter and shallower depth than the case of small Ga droplet according to the solubility argument. These explanations are well consistent with the results in samples C and D. If $2r_d < r_c$ and the Ga droplet is so large that the Ga atoms can diffuse far away from the droplet, diffusing Ga atoms tend to accumulate at the distance as far as possible away from the droplet due to the large gradient of Ga atom concentration. An outer zone of GaSb nanocrystals around the GaSb QR is therefore developed. This is similar to the formation mechanism of GaAs concentric double rings [97]. Owing to the lattice mismatch between GaSb and GaAs, the formation of GaSb QDs in order to reduce the strain energy can take place at the periphery of the outer zone where GaSb accumulates. Thus, the shape of GaSb nanostructures consists of the QR surrounded by R-QDMs. The diameter and the depth of QR in sample B become larger and shallower, respectively, compared with the two previous cases because of the solubility issue. This condition along with the mechanisms which have just been discussed can explain the origin of the complex GaSb nanostructure observed in sample B. Moreover, r_d of sample B can be estimated by a half of w', i.e., $r_d \approx 120$ nm. Since the diffusion area of Ga atoms becomes larger as the droplet size increases [93, 94], if the Ga droplet is far larger such that $2r_d > r_c$, the diffusion area of Ga atoms for each Ga droplet overlaps with each other. Under this condition, the periphery of the outer zone and r_d cannot be identified. Consequently, the QR should be obtained again without the existence of R-QDMs. Also, the GaSb layer should be thicker as a result of the diffusion area overlap. Such mechanisms are plausible for sample A. According to the solubility argument, the QR diameter and depth in sample A should be much larger and shallower, respectively. The average QR diameter of sample A is the largest as expected. In contrast to the prediction, the AFM result reveals that the average QR depth of sample A is the deepest. This observation is attributed to a shift-up of mean surface level due to the thicker GaSb layer. Thus, for sample A, the QR depth measured by AFM is somewhat deeper than the real depth coming from the droplet etching process.

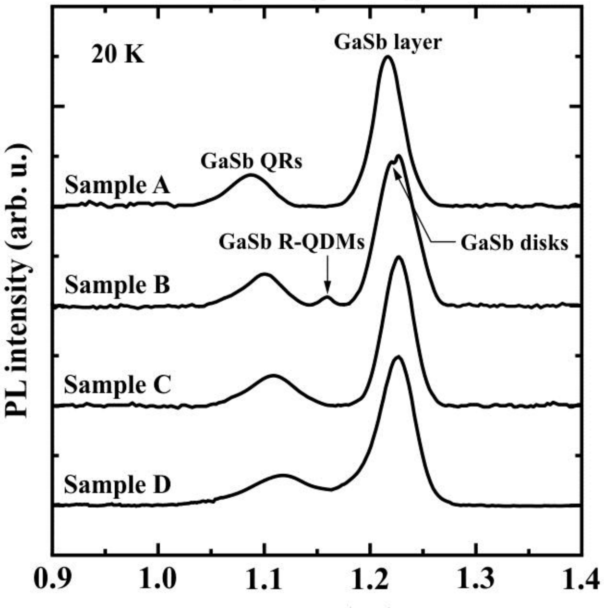

Figure 7.6 Normalized PL spectra of GaSb nanostructures at 20 K.

Consistent results with this model are also observed from the PL measurement of the capped samples. Figure 7.6 shows the normalized PL spectra of GaSb nanostructures at 20 K. The GaSb QR peaks for samples A, B, C, and D are at 1.088, 1.100, 1.107, and 1.118 eV, respectively. It is clear that the QR peak shifts to higher energy with decreasing the QR size. As a result of Sb-for-As exchange reaction, the GaSb layer is formed during crystallization. The PL peaks of the GaSb layer in samples B, C, and D locate at the same energy position of 1.227 eV, indicating the same thickness of GaSb layer. Besides, the PL results confirm the model which describes the formation mechanisms of GaSb nanostructures under the condition $2r_d < r_c$. For sample B, in addition to the GaSb QR and the GaSb layer, a small peak at 1.160 eV is attributed to the GaSb R-QDMs, whereas another peak placing at 1.220 eV which is close to the peak of GaSb layer likely stems from the GaSb disk. For sample A, the peak from the GaSb layer appears at 1.217 eV which is lower than the other samples, reflecting that the GaSb layer becomes thicker. Hence, the GaSb layer in sample A is formed not only by the Sb-for-As exchange reaction but also by the diffusion area overlap which is consistent with the model when the condition $2r_d > r_c$ is satisfied. The thicker GaSb layer causes the shift-up of mean surface level and also affects the QR depth measured by AFM. That is why the QR depth in sample A is the deepest among all samples.

Chapter 8

Effect of Ga deposition temperatures on GaSb/GaAs nanostructures

Apart from the Ga deposition rate, the substrate temperature for Ga deposition affects the size and density of Ga droplets. As the lattice mismatch strain increases with the nanostructure size, some part of a GaSb quantum ring (QR) may break up and transform into a quantum dot (QD) for reducing the strain energy, giving rise to a peculiar nanostructure which is composed of the QD and the QR in the same nanostructure. This is called a quantum ring-with-dot structure (QRDS). The formation of QRDSs becomes more apparent when the Ga deposition temperature increases. Moreover, it is found that the transition from unimodal to bimodal nanostructure height distributions occurs at high deposition temperature as a result of the large difference between QR and QD heights. Consequently, the carrier dynamics in the QRDSs are remarkable and discussed as the main issue of this chapter.

8.1 Experimental details

All samples were grown on semi-insulating GaAs (001) substrates by solid-source molecular beam epitaxy. The native oxide on substrate surface was removed at 580 °C under $\mathrm{As_4}$ flux of 8×10^{-6} Torr for 10 min. After the growth of a 300-nm GaAs buffer layer at 580 °C, the substrate temperature was reduced to the desired temperature for the Ga deposition. The deposition temperature (T_d) was set to 275, 300, 325, and 350 °C (referred as samples A, B, C, and D, respectively). In this temperature range, the reflection high energy electron diffraction (RHEED) pattern showed a *c*(4×4) As-stabilized surface. Once the substrate temperature reached the desired T_d, the $\mathrm{As_4}$ flux was terminated to remove the As background pressure for preventing the initial reaction between Ga and $\mathrm{As_4}$ during the droplet formation. When the background pressure of the growth chamber was less than 5×10^{-9} Torr, the Ga amount of 3 monolayers (ML) was deposited on the substrate with a rate of 0.5 ML/s to create the liquid Ga droplets. The droplets were crystallized at 275 °C by the $\mathrm{Sb_4}$ flux of 5×10^{-7} Torr for 90 s. The sample was either quenched to room temperature for surface morphology analysis with atomic force microscopy (AFM) operated in dynamic mode, or further grown with a 150-nm GaAs layer to cover the GaSb nanostructures for photoluminescence (PL) study. The details of the capping process have been stated in Chapter 5. In the PL system, the samples were excited by a 100-mW Ar^+ laser having a spot size of ~0.3 mm, and a cooled InGaAs detector together with a standard lock-in technique was used to detect and record the PL spectra.

8.2 Results and discussion

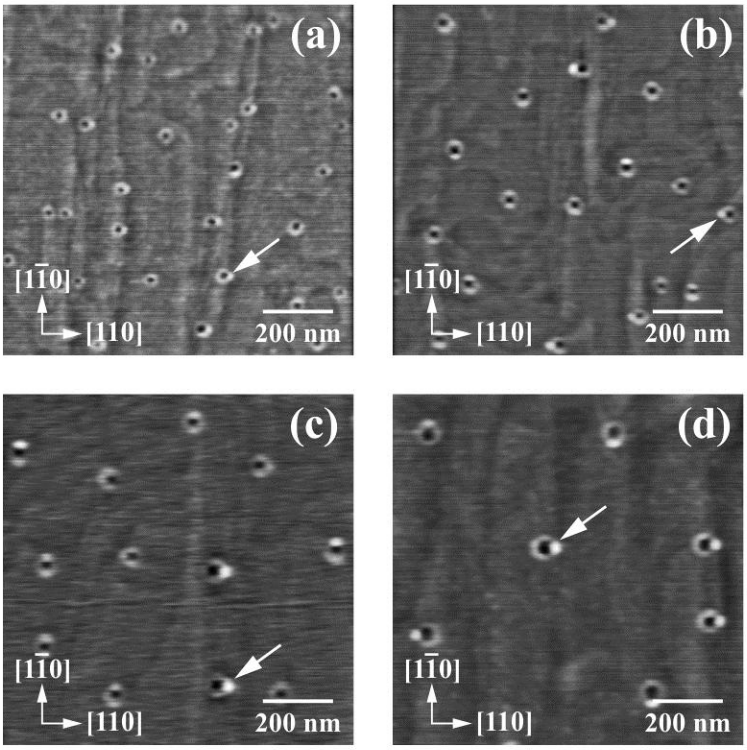

Figure 8.1 AFM images of GaSb nanostructures in (a) sample A, (b) sample B, (c) sample C, and (d) sample D. The QD formed at the QR lobe in each sample is pointed out by an arrow.

When Ga was deposited on the GaAs surface, the Ga droplets were formed in the Volmer-Weber-like growth mode. In this work, the droplet size and density can be controlled by T_d that governs the diffusion length of Ga atoms. GaSb nanostructures were obtained after crystallization with Sb_4 flux for 90 s. The AFM images of GaSb nanostructures are displayed in Figure 8.1. Each nanostructure consists of a lobe around a nanohole, which is called QR. However, some portion of the lobe breaks up and transforms into a kind of QD, leading to the QRDS. The nanohole at the center of QR results from the Ga droplet etching, while the origin of QR lobe can be described by the outward diffusion of Ga atoms from the initial Ga droplet because of the low Sb_4 flux intensity which enables the growth of GaSb nanocrystals at the droplet periphery to be faster than other parts of the droplet [32]. A compressive strain caused by the lattice mismatch between GaSb and GaAs is built up and stored in the QR lobe during crystallization. Thus, the QD formation would be responsible for the strain relaxation [24].

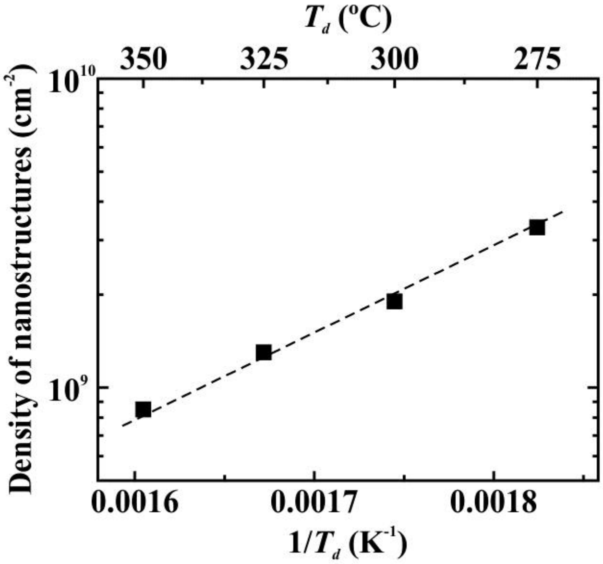

Figure 8.2 Density of GaSb nanostructures plotted as a function of Ga deposition temperature (T_d) and its reciprocal value ($1/T_d$). The dashed line represents least-squares fit to the data.

The densities of GaSb nanostructures and initial Ga droplets would be equivalent owing to the low growth temperature where the desorption of Ga atoms from the surface can be omitted. The density of nanostructures is 3.3×10^{9}, 1.9×10^{9}, 1.3×10^{9}, and 8.5×10^{8} cm^{-2} for samples A, B, C, and D, respectively. The density decreases with increasing T_d because the adatom diffusivity (D_s) increases with temperature, which is described by $D_s \propto \exp(-E_s / k_B T_d)$ where E_s is the activation energy for surface diffusion. In complete condensation regime, if E_s is only considered, the maximum cluster density can be simply expressed by $n_x \propto 1/D_s$ [27]. Figure 8.2 shows the density of GaSb nanostructures as a function of T_d and its reciprocal value ($1/T_d$). The activation energy for the Ga atom diffusion estimated from the slope of a dashed line in Figure 8.2 is ~0.65 eV.

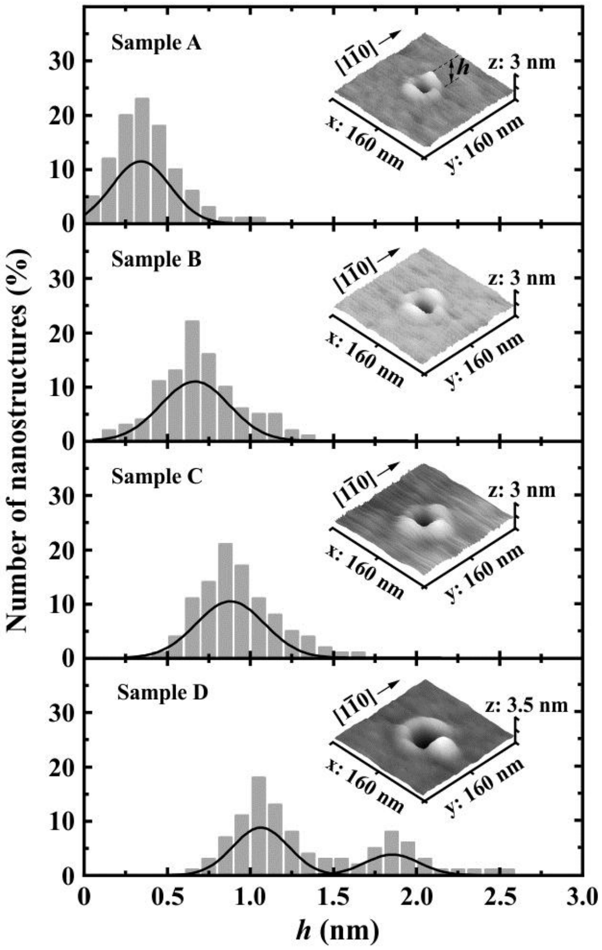

Figure 8.3 Histograms of nanostructure height (*h*). The solid lines are Gaussian fits to the data. Three-dimensional AFM image of an individual nanostructure from each sample is also presented.

In the droplet epitaxy of lattice-mismatched systems, not only the diffusion behaviors of group-III and group-V atoms but also the strain developed during crystallization is significant. As previously mentioned, the strain relaxation would cause the breaking up of QR lobe and the QD formation. For nanostructures, height is very important in determining the PL energy position, whereas height distribution correlates with the PL line shape. The height (*h*) of GaSb nanostructure was measured along both [110] and [$1\bar{1}0$] directions. In Figure 8.3, the height distributions of samples A, B, and C are unimodal, while sample D possesses the bimodal height distribution where the lower-*h* and higher-*h* sides are attributed to the QRs and the QDs, respectively. However, there is an overlap between these two distributions. By performing the Gaussian fit to the data, the average QR heights for samples A, B, C, and D are 0.33, 0.65, 0.88, and 1.07 nm, respectively. The average height becomes higher with the increase in T_d as a result of the larger original droplets. The center of the Gaussian fitted line on the higher-*h* side, which is equal to 1.83 nm, can be estimated to be the average QD height in sample D.

In addition to the height, diameter is another factor affecting the PL emission since the lateral dimensions relate to the separation of quantized energy levels. The diameter (*w*) of GaSb nanostructure is defined by a distance between highest points (see Figure 8.4(a)) along both [110] and [$1\bar{1}0$] directions. The nanostructure shape is quite circular because of an isotropic diffusion of Ga atoms on the GaSb surface formed by the Sb-for-As exchange reaction during crystallization [24]. The average diameters are 48.5, 52.6, 57.2, and 60.7 nm for samples A, B, C, and D, respectively. As the diffusion length of Ga atoms increases with temperature, the droplet size and hence nanostructure diameter increase with T_d. In Figure 8.4(b), the diameter in each sample exhibits a unimodal distribution, suggesting that the QD formation does not significantly influence the diameter of GaSb nanostructure. To make a closer look at the QRDS, a magnified AFM image of a single QRDS from sample D with its corresponding contour plot is shown in Figure 8.4(a). It is obvious that the base of QD extends inwards the nanohole edge and also outwards the QR periphery, as pointed by arrows in Figure 8.4(a). This observation is likely related to the compressive strain within QR structure [98]. Therefore, the QD base is slightly wider than the QR lobe width after strain relaxation.

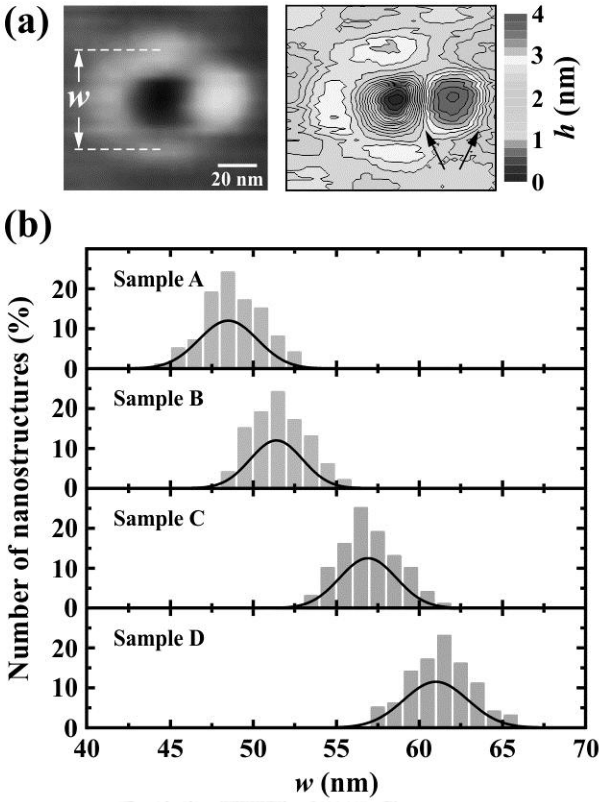

Figure 8.4 (a) A magnified AFM image of a single QRDS taken from sample D and its contour plot. The extension of QD base (inwards nanohole edge and outwards QR periphery) is indicated by arrows. (b) Histograms of nanostructure diameter (*w*). The solid lines are Gaussian fits to the data.

The normalized PL spectra measured at 20 K are depicted in Figure 8.5. The peak energy of 1.222 eV likely comes from a GaSb layer which would be formed by the Sb-for-As exchange reaction during crystallization. The peaks from GaSb nanostructures for samples A, B, and C locate at 1.118, 1.110, and 1.105 eV, respectively. Due to no clear difference between QR and QD heights in samples A, B, and C, the emissions of QRs and QDs, which contribute to the PL band, cannot be discriminated. For this reason, such a PL band is defined as *RD* which is referred to the indistinguishable PL emission. On the other hand, for sample D, two PL peaks at 1.050 and 1.101 eV are attributed to QDs and QRs, which are labelled as *D* and *R* bands, respectively, because the QD height is higher than the QR one. The PL results are consistent with the size distribution analysis. The shift of *RD* peak to the lower energy stems from the nanostructure size which is larger as T_d increases. Since the size distribution of nanostructures affects not only the PL line shape but also the behavior of carriers activated by temperature, the optical properties of sample D possessing both clear QRDSs and bimodal height distribution are of interest.

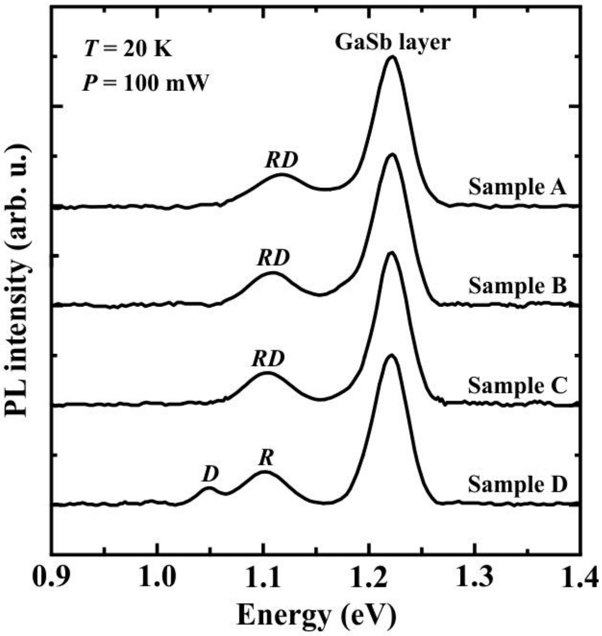

Figure 8.5 Normalized PL spectra at temperature T = 20 K with excitation power P = 100 mW. *RD* denotes the indistinguishable PL band contributed by both QR and QD emissions. *D* and *R* represent the PL emissions from QDs and QRs, respectively.

According to the PL spectrum of sample D, the *D* and *R* bands overlap each other and are far from the emission from the GaSb layer, as seen in Figure 8.5. Due to the proximity of QR to QD as well as the significant difference between QR and QD heights, which results in their own energy levels, the thermally activated carriers (holes) would directly tunnel from a QR into a QD in a single QRDS. This scenario is different from the carrier transfer in the bimodal QDs through the wetting layer, which is generally observed in InAs/GaAs QDs [46-48]. Nevertheless, the carrier migration from small QRDSs to large ones via the GaSb layer should still exist because of the large lateral dimension of nanostructures. The temperature dependence of PL spectra from sample D is displayed in Figure 8.6(a). At 250 K, the QR emission can be still observed, whereas the QD emission cannot be found. It is likely because the QRs have more surface area for the radiative recombination than the QDs. The peak energies of *D* and *R* bands (denoted by E_D and E_R) plotted as a function of temperature (*T*) are depicted in Figure 8.6(b). Both E_D and E_R show a blueshift in a range of 20-50 K, and then follow the band gap temperature dependence at high temperatures. The mechanisms responsible for such a blueshift at low temperatures are as follows. According to the type-II band alignment of GaSb/GaAs, an internal electric field at the GaSb/GaAs interface is induced by the confined holes in GaSb and the electrons in GaAs, which are attracted around GaSb via Coulomb interaction. Such an electric field bends the conduction band into the triangular quantum well, giving rise to the quantization energy levels for electrons. An increase in temperature results in the more population of thermal-excited carriers, leading to the steeper triangular quantum well and thus the shift-up of the quantization energy levels. For this reason, the PL peak energy exhibits the blueshift. Nonetheless, as temperature further increases, there is the competition between the energy level shift-up, and the cumulative effects of electron-phonon interaction and thermal lattice expansion, which lower the PL peak energy. The PL results suggest that the latter begins to be significant when $T > 50$ K, and becomes more predominant at high temperatures, as seen from the reductions in E_D and E_R.

The migration of thermal-excited carriers can be investigated from the changes of the integrated PL intensity and the full width at half maximum (FWHM) of PL line shape. The variations of the integrated PL intensity ratio of the *D*-band emission to the *R*-band one (I_D / I_R) and the FWHMs of *D* and *R* bands (labelled as F_D and F_R) are shown in Figures 8.6(c) and (d), respectively. The PL intensity ratio, F_D, and F_R are almost constant in the range of 20-50 K, implying that holes are still confined in the GaSb nanostructures. It is worth noting that both intensity ratio and F_D increase, whereas F_R decreases at intermediate temperatures (60-140 K). This behavior indicates that the thermally activated holes transfer from the QRs to the QDs and/or other larger nanostructures having a lower energy state. As temperature further increases, the reduction in intensity ratio is likely due to the holes which are thermally escaped from the QDs to the GaSb layer and/or the GaAs matrix as well as the non-radiative recombination centers, and/or become recaptured into the QRs. The increments in F_R and F_D can be explained by the electron-phonon interaction which is more important at high temperatures. The recapture of thermal-excited holes into the QRs would also participate in the rise of F_R. However, the further studies on experimental and theoretical aspects are needed for better understanding of the mechanisms of optical transition and carrier dynamics in type-II nanostructures with bimodal size distribution.

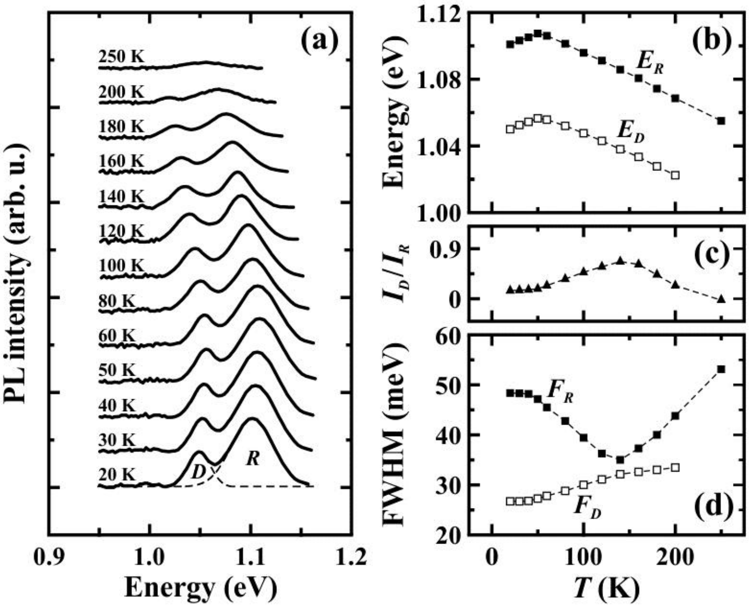

Figure 8.6 (a) Temperature-dependent PL spectra of sample D with excitation power of 100 mW. The dashed lines are Gaussian fits to the PL spectrum for specifying D and R bands. The plots of (b) PL peak energies (E_D and E_R), (c) integrated PL intensity ratio (I_D/I_R), and (d) FWHM values (F_D and F_R) as a function of temperature. The dashed lines in (b), (c), and (d) show the trend of variation.

Chapter 9

Effect of crystallization temperatures on GaSb/GaAs nanostructures

In droplet epitaxy, the crystallization process is very important as the feature of nanostructures is decided by the crystallization condition. The temperature and the group-V flux intensity are the main parameters in the crystallization process. Nonetheless, the latter cannot be studied due to the limitation of Sb valved-cracker cell, as stated in Chapter 1. The crystallization temperature strongly affects not only the nanostructure morphology but also the thickness of GaSb layer originated from the Sb-for-As exchange reaction. Similar to Chapter 7, the GaSb quantum ring (QR) and the QR surrounded by ring-shaped quantum dot molecules (R-QDMs) can be obtained by adjusting the crystallization temperature. Hence, the model proposed in Chapter 7 can be applied to explain the formation mechanism of these nanostructures. Interestingly, the GaSb layer does not appear at very low crystallization temperature. This chapter also presents a comparison between the carrier dynamics in GaSb QRs with and without the GaSb layer.

9.1 Experimental details

All samples were grown on semi-insulating GaAs (001) substrates by solid-source molecular beam epitaxy. Prior to the growth of 300-nm GaAs buffer layer, the native oxide on the substrate surface was removed at 580 °C under $\mathrm{As_4}$ flux of 8×10^{-6} Torr for 10 min. The substrate temperature was subsequently lowered to 350 °C. Then, the $\mathrm{As_4}$ flux was stopped supplying to eliminate the As background pressure which may initially react with Ga atoms during Ga deposition for the droplet formation. Once the background pressure of the growth chamber was less than 5×10^{-9} Torr, Ga amount of 3 monolayers (ML) was deposited on the substrate at 350 °C with a rate of 0.3 ML/s. After that, the Ga droplets were crystallized by $\mathrm{Sb_4}$ flux of 5×10^{-7} Torr for 90 s at desired temperature. The crystallization temperature (T_c) was set to 200, 225, 250, and 275 °C (labeled as samples A, B, C, and D, respectively). The sample was either quenched to room temperature for surface morphology analysis with atomic force microscopy (AFM) operated in dynamic mode, or further grown with a 150-nm GaAs layer to cover the GaSb nanostructures for photoluminescence (PL) measurement (see more details in Chapter 5). A 514.5-nm line Ar$^+$ laser having a spot size of ~0.3 mm and a cooled InGaAs detector were used in the PL system.

9.2 Results and discussion

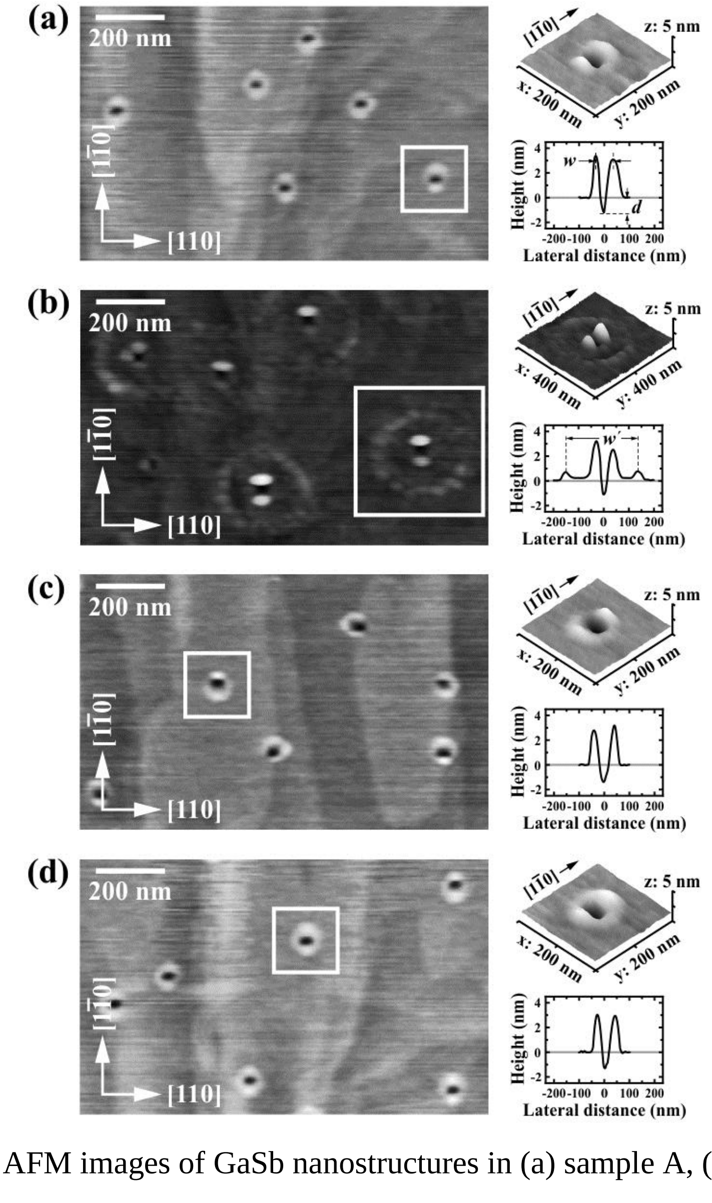

Figure 9.1 AFM images of GaSb nanostructures in (a) sample A, (b) sample B, (c) sample C, and (d) sample D. Three-dimensional AFM images of selected nanostructures (enclosed by white squares) with their cross-sectional profile along the $[1\bar{1}0]$ direction are also displayed. The gray lines represent the mean surface level.

AFM images of samples A, B, C, and D are shown in Figure 9.1. Here, the GaSb nanostructures are categorized into two types. One is the QR which is formed in samples A, C, and D. The other is the QR surrounded by R-QDMs, which is found in sample B. The density of GaSb nanostructures is $\sim 5.6\times 10^{8}$ cm^{-2} for each sample because of the same Ga deposition temperature and deposition rate, resulting in the same initial droplet density. The average QR diameter (w) is ~77 nm for all samples, implying that T_c does not take more effect on the QR diameter. The average values of QR depth (d) are about 1.1, 1.1, 1.6, and 1.6 nm for samples A, B, C, and D, respectively. The variation of d involves with the diffusion behavior of Ga atoms during crystallization, which will be discussed later. It is worth pointing out that there are few quantum ring-with-dot structures found even the QR size is larger than that in Chapter 8. As a matter of fact, the QD formation reduces the strain energy at the expense of the surface energy such that the minimization of total energy of the system is achieved. Consequently, in this case, it is plausible that most of the QRs can handle their compressive strain and exist as a stable shape.

The QR formation can be described by the outward diffusion of Ga atoms from the original droplets as a result of the gradient of Ga atom concentration and the use of low Sb_4 flux intensity, whereas the nanohole at the center of the QR results from the droplet etching process. Since the diffusion length of Ga atoms determines the morphology of GaSb nanostructures and exponentially increases with temperature, the descriptive model in Chapter 7 can be applied here to describe the origin of R-QDMs as well as the change of QR depth. Given that the radius of diffusion area for each Ga droplet is r_d and the distance between the centers of Ga droplets is r_c. The droplet size and its distribution are assumed to be the same in all samples due to the same Ga deposition temperature and deposition rate. For this reason, according to the model, r_d is only varied and becomes longer when T_c increases. If $2r_d < r_c$ and T_c is not high, then the diffusion of Ga atoms will be limited around the droplet periphery, giving rise to the GaSb QR as observed in sample A. When T_c is so high that the Ga atoms are allowed to diffuse away from the original droplet but the condition $2r_d < r_c$ is still satisfied, an outer zone of GaSb nanocrystals around the GaSb QR can be developed as a result of the gradient of Ga atom concentration. Because of the mismatch strain stored in the GaSb nanocrystals, the QDs which are circularly formed along the outer zone would be a way to reduce the strain energy. This can describe the origin of the GaSb nanostructures in sample B, which consist of the QR surrounded by R-QDMs. Besides, r_d can be estimated by a half of w', i.e., $r_d \approx 150$ nm. If T_c further increases such that $2r_d > r_c$, the diffusion area for each droplet overlaps with each other. Therefore, the QR should be obtained again because the periphery of outer zone and r_d cannot be identified. Moreover, the diffusion area overlap causes a shift-up of mean surface level, resulting in the deeper QR depth. This condition is well consistent with the AFM results in samples C and D. The cross-sectional profile in Figure 9.1(b) shows that there is an almost flat region between the QR and the R-QDMs. Such a region is called a GaSb disk.

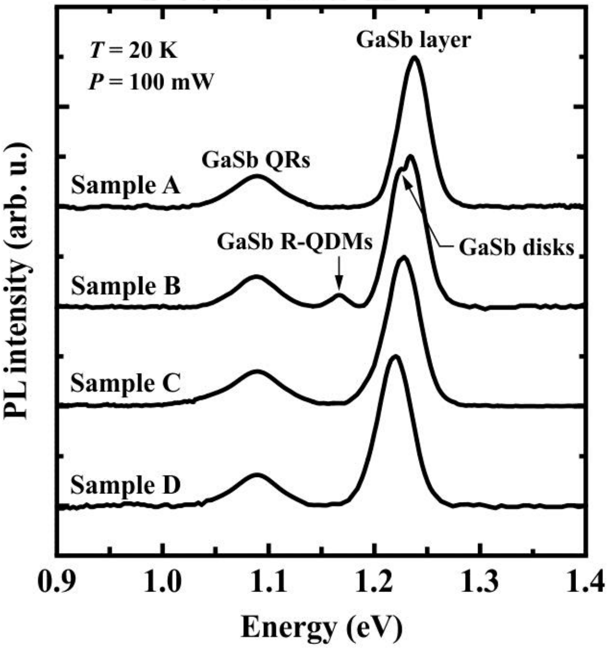

Figure 9.2 Normalized PL spectra at temperature $T = 20$ K with excitation power $P = 100$ mW.

The normalized PL spectra measured at 20 K are depicted in Figure 9.2. The PL peak from the GaSb layer which is formed during crystallization places at 1.238, 1.232, 1.227, and 1.218 eV for samples A, B, C, and D, respectively. Such a decrease in the peak energy indicates that the GaSb layer becomes thicker with the increase in

T_c because raising the temperature encourages the Sb-for-As exchange reaction and the diffusion of Sb atoms into the GaAs buffer layer [90]. The thickening of GaSb layer in samples C and D also comes from the diffusion area overlap, as described in Chapter 7. It is obvious that T_c plays a crucial role in the thickness of GaSb layer. On the contrary, T_c does not influence the GaSb QRs as the QR peak appears at 1.090 eV for every sample. For sample B, there are two additional peaks at 1.165 and 1.224 eV, which are attributed to the GaSb R-QDMs and the GaSb disks, respectively. Since the PL results evidently show that the GaSb layer thickness can be changed by T_c, it is possible to eliminate the GaSb layer by applying very low T_c in order to suppress the Sb-for-As exchange reaction and limit the diffusion area. Therefore, it can be hypothesized that the use of very low T_c with the same Sb_4 flux intensity should result in the GaSb QRs without the GaSb layer. To verify this hypothesis, another sample (referred as sample E) was grown with the same growth parameters, except T_c which was set to 100 °C.

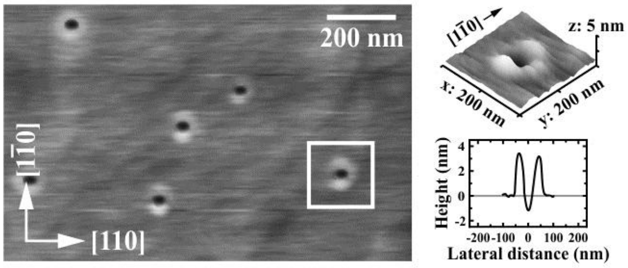

Figure 9.3 AFM image of GaSb nanostructures in sample E. Three-dimensional AFM image of a selected nanostructure (enclosed by a white square) with its cross-sectional profile along the $[1\bar{1}0]$ direction is also displayed. The gray line represents the mean surface level.

Figure 9.3 shows the AFM image of sample E. As expected, the GaSb QRs are obtained and the density is equivalent to the other samples ($\sim 5.6\times10^{8}$ cm^{-2}). The average QR size is ~77 nm in diameter and ~1.1 nm in depth. The PL measurement with the variation of excitation power (P) from 5 to 200 mW was carried out on sample E. The higher excitation powers were also used but the PL intensity decreases as a consequence of the heat generated in the sample. The power-dependent PL spectra of sample E are depicted in Figure 9.4. Even though the PL intensity of the GaSb layer is several times higher than that of the GaSb QRs, the peak from the GaSb layer cannot be observed, whereas the QR emission still exists. The inset of Figure 9.4 displays the peak energy of the GaSb QRs (E_{QR}) plotted as a function of the third root of excitation power ($P^{1/3}$). It is clear that E_{QR} is linearly dependent on $P^{1/3}$, which is the characteristic of type-II band alignment.

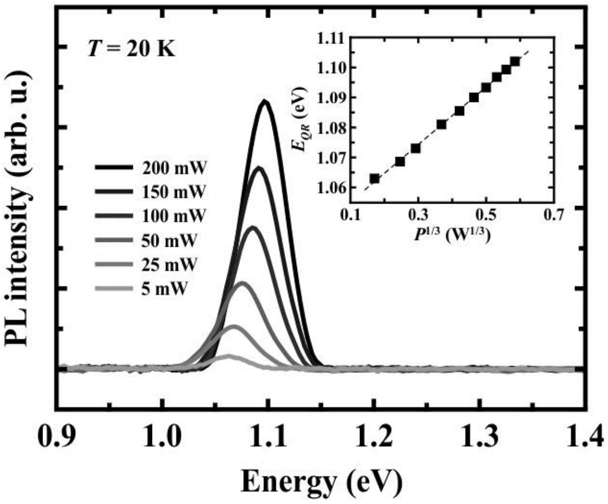

Figure 9.4 Power-dependent PL spectra of sample E at temperature T = 20 K. The inset shows the variation of E_{QR} as a function of the third root of excitation power. The dashed straight line is guide for the eyes.

Since the GaSb layer acts as the channel for the migration of thermal-excited carriers between the GaSb QRs, the temperature-dependent PL measurement is a way to investigate the difference in the carrier behaviors between the QR samples with and without the GaSb layer. Thus, samples A and E were chosen for comparison. The temperature dependence of PL spectra of these two samples is shown in Figure 9.5. The temperature (T) was varied from 20 to 250 K, where the PL signals can be apparently observed. The variations of E_{QR} as a function of temperature are displayed in Figures 9.6(a) and (c). It is found that the tendencies of the changes in E_{QR} are similar in both samples. Because the spatial separation between electrons and holes creates an internal electric field at the GaSb/GaAs interface, the conduction band is bent into a triangular quantum well, leading to the quantization energy for electrons, as shown in the inset of Figure 9.5(b). The increase in temperature causes more population of thermal-excited carriers at the GaSb/GaAs interface and stronger band bending which raises the electron quantization energy level. This mechanism can explain the blueshift of E_{QR} at low temperatures (20-50 K). When the temperature further increases, both the electron-phonon scattering and the thermal lattice expansion begin to dominate over the rise of the quantization energy level. Hence, E_{QR} shifts to the lower energy at high temperatures.

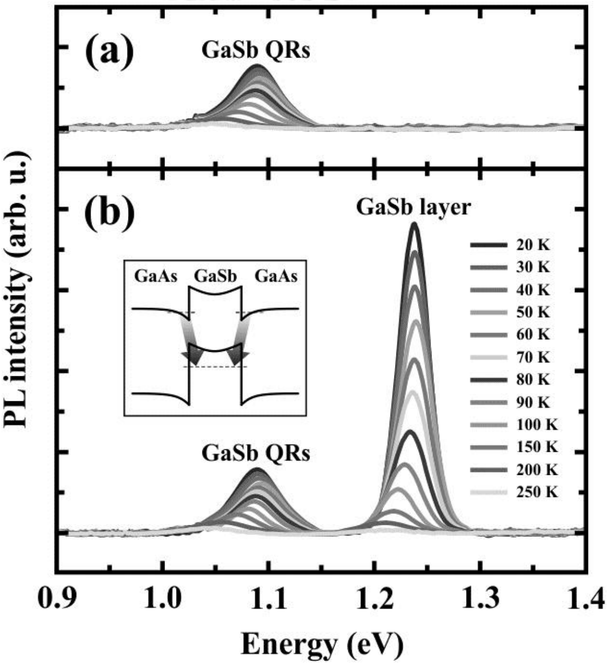

Figure 9.5 Temperature-dependent PL spectra of (a) sample E and (b) sample A, which were obtained by using the excitation power of 100 mW. Schematic band alignment of GaSb/GaAs heterostructure including the band-bending effect is also displayed in the inset of (b).

A significant difference between the QR emissions from samples A and E is the variation of full width at half maximum (FWHM). As seen in Figures 9.6(b) and (d), FWHM is almost constant over the temperature range of 20-50 K, indicating that holes are still confined in the GaSb QRs. For sample E, FWHM increases with temperature when $T > 50$ K (see Figure 9.6(b)) due to the electron-phonon scattering. This is similar to the type-I InGaAs/GaAs QDs without wetting layer (WL) [99]. On the contrary, Figure 9.6(d) shows that FWHM of sample A decreases at intermediate temperatures (60-125 K) and then increases at higher temperatures. The band narrowing at the intermediate temperatures is attributed to the thermally escaped holes which transfer from the small QRs to the large ones through the GaSb layer, while the band broadening at high temperatures likely stems from the electron-phonon scattering. Although the decrement in FWHM in sample A at the intermediate temperatures can be seen as the evidence of the migration of holes from small to large QR ensembles, the fast redshift of peak energy does not appear, which is in contrast to the type-I QDs with WL [99]. This observation is ascribed to the band-bending effect which would compensate the reduction of transition energy (i.e., the difference between electron and hole quantization energy levels) caused by electron-phonon interaction.

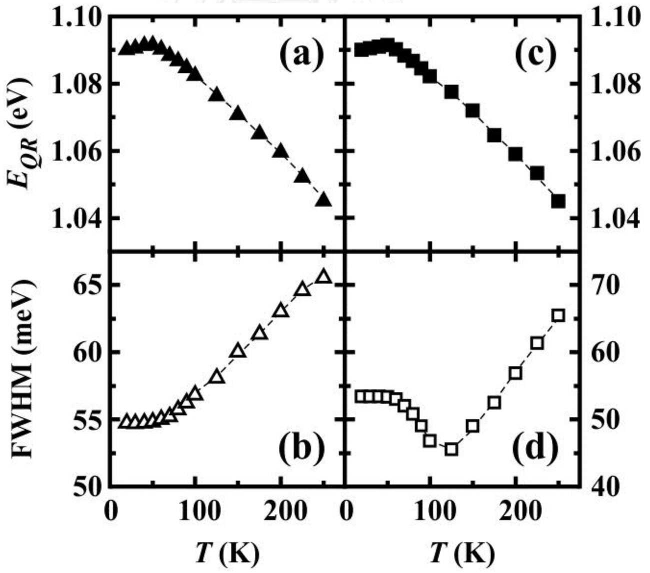

Figure 9.6 Temperature dependence of (a) E_{QR} and (b) FWHM of QRs in sample E. Temperature dependence of (c) E_{QR} and (d) FWHM of QRs in sample A. The dashed lines present the trend of variation.

Another crucial point is the ability of hole confinement which is expected to be more effective in the GaSb QRs without the GaSb layer. According to the temperature-dependent PL results, the activation energy (E_A) for thermal quenching of QR band can be extracted from the Arrhenius plot of integrated PL intensity (see Figure 9.7). The temperature dependence of integrated PL intensities of the QRs in samples A and E is well described by

$$I_{PL}(T) = \frac{I_0}{1 + C\exp(-E_A / k_B T)} \tag{9.1}$$

where I_0 is the integrated PL intensity at 0 K, C is a constant, and k_B is the Boltzmann constant. The activation energy is ~176 meV for sample A and ~420 meV for sample E. It is clear that the activation energy of the QRs in sample E is comparable to the hole confinement energy of 450 meV [10], indicating that the thermionic emission of holes from the GaSb QRs to the GaAs matrix is responsible for the reduction in PL intensity. On the other hand, the activation energy of the QRs in sample A is much smaller than the hole confinement potential because the thermal-excited holes can transfer between the GaSb QRs and the GaSb layer, and the holes which are thermally activated from the GaSb layer can be recaptured into the GaSb QRs [7], decelerating the quenching of QR emission.

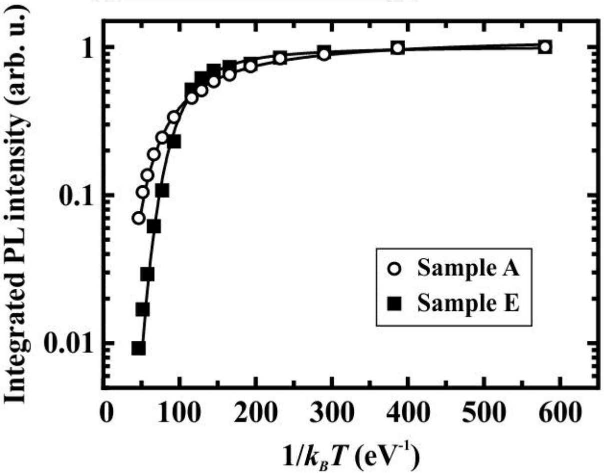

Figure 9.7 Arrhenius plot of normalized integrated PL intensity for QRs in samples A and E. The solid lines are the activation energy fit.

So far, the advantages of uncoupling between type-II nanostructure states in the application point of view have never been mentioned, while the absence of WL in type-I QD ensemble is expected to enhance the performance of QD lasers [99].

Nonetheless, because of the deep confining potential for holes and small nuclear moment in the GaSb/GaAs nanostructures [100], hole spins can be robust against the dephasing [101]. Since the hole-spin relaxation time decreases with increasing the temperature in the case of quantum wells as a consequence of hole delocalization [102], the GaSb/GaAs QDs or QRs without the GaSb layer would prolong the hole-spin relaxation time. These scenarios might be promising for quantum information processing [101].

Chapter 10

Conclusion

The influence of growth parameters on GaSb/GaAs nanostructures grown by droplet epitaxy using solid-source molecular beam epitaxy has been intensively and systematically investigated. By virtue of the valved-cracker cell which can produce the Sb flux intensity up to ~10^{-6} Torr, most of the GaSb nanostructures are ring-shaped as a result of such a low Sb flux employed in the crystallization process. However, droplet epitaxy, which provides the high degree of freedom to engineer the morphology and other properties of III-V self-assembled nanostructures, can break through this limitation as there are many crucial parameters in droplet epitaxy technique. This advantage is derived from its procedure which is divided into two steps: the formation of group-III droplets and the crystallization with group-V flux. For droplet epitaxy of GaSb nanostructures on the GaAs substrates, the Ga amount, Ga deposition rate, and Ga deposition temperature are the growth parameters which can be varied in the first step. Even the crystallization temperature and Sb flux intensity are important in the second step, the Sb flux intensity cannot be adjusted over a wide range due to the technical limit of equipment. Thus, the crystallization temperature becomes the only one parameter in the second step of droplet epitaxy, which has been studied in this dissertation.

Droplet epitaxy offers the ability to fabricate GaSb quantum rings (QRs) by crystallizing the Ga droplets with the low Sb flux. The QR results from the outward diffusion of Ga atoms from the Ga droplet owing to the growth of GaSb nanocrystals at the droplet periphery which is faster than the other parts, and the gradient of Ga atom concentration. It is worth noting that the GaSb QRs are somewhat circular because the Sb-for-As exchange reaction turns the GaAs surface into the GaSb surface during crystallization and the diffusion of Ga atoms on the GaSb surface is isotropic. Since the Ga droplet can dissolve the GaAs layer underneath, the nanohole is formed at the center of the GaSb QR after crystallization. The evolution of Ga droplets into the GaSb QRs is tracked by reflection high energy electron diffraction (RHEED) and atomic force microscopy (AFM). The RHEED specular beam intensity suggests that the minimum crystallization time is ~50 s. The longer crystallization time is needed for the larger droplets. Nonetheless, the longer time and/or the higher Sb flux may induce the polycrystalline granular Sb layer on the growth surface. Consequently, the maximum crystallization time of 90 s is enough to ensure the complete crystallization.

To examine the optical properties of GaSb nanostructures buried in the GaAs matrix by photoluminescence (PL) measurement, the capping process is very critical as the GaSb nanostructures might be destroyed by the intense As-for-Sb exchange reaction during the growth of GaAs capping layer. The As-for-Sb exchange can be suppressed at low temperature. The GaSb nanostructures are therefore capped with a 20-nm GaAs layer at 250 °C, and followed by an additional 130-nm GaAs layer grown at 450 °C. The PL emission from the GaSb/GaAs nanostructures stems from the radiative recombination between holes confined in the GaSb nanostructures and electrons in the GaAs barrier, which are induced to reside at the GaSb/GaAs interface due to the Coulomb attraction. This leads to an internal electric field at the interface which bends the conduction band into a triangular quantum well. For this reason, the ground state transition energy increases with the excitation power and is linearly dependent on the third root of excitation power.

According to the Sb-for-As exchange reaction, the GaSb layer is often formed together with the GaSb nanostructures. Importantly, the GaSb layer plays a role in the carrier dynamics in the GaSb nanostructures. For the GaSb/GaAs QRs, the power-dependent PL results indicate that the PL peaks of both the GaSb QRs and the GaSb layer exhibit the blueshift when the excitation power increases. As expected, the peak energies of both structures proportionally increase with the third root of excitation power. Nevertheless, the peak of the GaSb layer becomes saturated at high excitation powers as a consequence of the reduction in the oscillator strength by the screening effect within two-dimensional electron-hole plasma. The temperature-dependent PL results suggest that the quenching of GaSb QR emission is derived from the thermal escape of holes, and there is the carrier transfer between the GaSb QRs and the GaSb layer. Interestingly, the PL peaks of both the GaSb QRs and the GaSb layer show the blueshift in low temperature range because the higher population of thermal-excited carriers induces a stronger band-bending effect, and then follow the band gap temperature dependence in high temperature range owing to the electron-phonon interaction. However, there is a competition between these two effects at intermediate temperatures. Hence, the optical behavior in type-II nanostructures is complicated.

The variation of Ga amount leads to the strange GaSb/GaAs nanostructures. The GaSb QR, which is quite circular, is obtained after crystallizing the 3-ML Ga droplet, while the nanostructure like the quantum dot (QD) at the edge of nanohole in the $[1\bar{1}0]$ direction originates in the cases of the 4- and 5-ML Ga droplets. These results reveal that the GaSb QDs tend to appear instead of the QRs if high Ga amounts are deposited. It is found that the crucial factors governing the shape of GaSb nanostructures are the diffusion behavior of Ga atoms, time taken for the droplets to be crystallized, and strain. The coalescence of the droplets is also observed at high Ga amounts.

Since the larger droplet provides the larger diffusion area, not only the GaSb QR but also the GaSb QR surrounded by ring-shaped quantum dot molecules (R-QDMs) can be achieved by changing the Ga deposition rate which determines the droplet size and density. For the large droplet, it is possible for Ga atoms to diffuse far away from the original Ga droplet, giving rise to an outer zone of GaSb nanocrystals. Nevertheless, the R-QDMs are introduced instead of an outer QR because of the strain relaxation. A simple descriptive model, which is based on the Ga droplet size, distance between Ga droplets, and diffusion area of Ga atoms, is proposed to elucidate the formation mechanisms of such nanostructures. This model is supported and verified by the PL measurement.

For droplet epitaxy in lattice-mismatched systems, the morphology of resulted nanostructures is generally decided by the balance between strain energy and surface energy in addition to the diffusion of group-III and group-V atoms. Because of the compressive strain in GaSb QR, some portion of QR lobe may break up and transform into the QD for reducing the strain energy. A nanostructure containing both the QR and the QD is called a quantum ring-with-dot structure (QRDS). Interestingly, the formation of QRDSs becomes more pronounced for large Ga droplets which can be obtained at high Ga deposition temperature. The QRs with rather uniform lobes can be consequently accomplished by using low Ga deposition temperature. It is worth pointing out that when the Ga deposition temperature increases, the nanostructure height distribution changes from unimodal to bimodal behaviors owing to the significant difference between QR and QD heights, whereas the nanostructure diameter still displays the unimodal distribution. The temperature-dependent PL results reveal that there is the transfer of thermal-excited holes between QR and QD ensembles through the GaSb layer and/or between the QR and the QD in the single QRDS, as evidenced by the variations of integrated PL intensity and PL line shape.

As the diffusion of Ga atoms exponentially increases with temperature, the GaSb QR and the GaSb QR surrounded by R-QDMs can be grown by adjusting the crystallization temperature. For this reason, the model, which has been proposed in the case of the study of the effect of Ga deposition rate, is possibly applicable to this case. The PL measurement shows that the GaSb layer is thicker with increasing the crystallization temperature as a consequence of the stronger Sb-for-As exchange reaction and/or the diffusion area overlap. According to this observation, the GaSb QRs without the GaSb layer can be achieved by utilizing very low crystallization temperature. As a matter of fact, the GaSb layer acts as the channel for the migration of thermal-excited holes between GaSb QRs, affecting the hole confinement ability. The GaSb QRs without the presence of the GaSb layer, therefore, can confine holes more effectively than those with the GaSb layer, as confirmed by the temperature-dependent PL measurement.

Before closing this dissertation, there are some comments and suggestions worth mentioning. Firstly, the influence of the Sb flux intensity on the GaSb/GaAs nanostructures grown by droplet epitaxy is still open for further study. Secondly, the antimony radicals, in particular Sb_1 and Sb_2, are interesting as they are more reactive than Sb_4. Thirdly, the Aharonov-Bohm effect in the GaSb/GaAs QRs is intriguing for fundamental physics. Lastly, from the application point of view, the GaSb/GaAs nanostructures are suitable for photodetectors, solar cells, and memory devices due to the type-II band alignment. Compared with the GaSb/GaAs QDs, the GaSb/GaAs QRs can be seen as a candidate for light-emitting devices because they have more surface area for radiative recombination and less strain, resulting in more electron-hole wave function overlap. In addition, the GaSb QRs without the GaSb layer would enhance the hole-spin relaxation time and dephasing time, making them promising for quantum information processing.

REFERENCES

1. Büttiker, M., Imry, Y., and Landauer, R., *Josephson behavior in small normal one-dimensional rings.* Phys. Lett. A, 1983. **96**: p. 365.
2. Shimizu, H., et al., *InAs quantum dot lasers with extremely low threshold current density (7 A/cm^2/layer).* Jpn. J. Appl. Phys., 2005. **44**: p. L1103.
3. Nowozin, T., et al., *Materials for future quantum dot-based memories.* J. Nanomater., 2013. **2013**: p. 1.
4. Koguchi, N., Takahashi, S., and Chikyow, T., *New MBE growth method for InSb quantum well boxes.* J. Cryst. Growth, 1991. **111**: p. 688.
5. Hatami, F., et al., *Radiative recombination in type-II GaSb/GaAs quantum dots.* Appl. Phys. Lett., 1995. **67**: p. 656.
6. Suzuki, K., Hogg, R.A., and Arakawa, Y., *Structural and optical properties of type II GaSb/GaAs self-assembled quantum dots grown by molecular beam epitaxy.* J. Appl. Phys., 1999. **85**: p. 8349.
7. Alonso-Ávarez, D., et al., *Optical investigation of type II GaSb/GaAs self-assembled quantum dots.* Appl. Phys. Lett., 2007. **91**: p. 263103.
8. Laghumavarapu, R.B., et al., *GaSb/GaAs type II quantum dot solar cells for enhanced infrared spectral response.* Appl. Phys. Lett., 2007. **90**: p. 173125.
9. Lin, W.-H., et al., *The influence of background As on GaSb/GaAs quantum dots and its application in infrared photodetectors.* Phys. Status Solidi C, 2012. **9**: p. 314.
10. Geller, M., et al., *450 meV hole localization in GaSb/GaAs quantum dots.* Appl. Phys. Lett., 2003. **82**: p. 2706.
11. Lin, S.-Y., et al., *Room-temperature operation type-II GaSb/GaAs quantum-dot infrared light-emitting diode.* Appl. Phys. Lett., 2010. **96**: p. 123503.
12. Tatebayashi, J., et al., *Lasing characteristics of GaSb/GaAs self-assembled quantum dots embedded in an InGaAs quantum well.* Appl. Phys. Lett., 2007. **90**: p. 261115.
13. Kamarudin, M.A., et al., *Tuning the properties of exciton complexes in self-assembled GaSb/GaAs quantum rings.* Phys. Rev. B, 2011. **83**: p. 115311.

14. Carrington, P.J., et al., *Enhanced infrared photo-response from GaSb/GaAs quantum ring solar cells.* Appl. Phys. Lett., 2012. **101**: p. 231101.
15. Grochol, M., Grosse, F., and Zimmermann, R., *Optical exciton Aharonov-Bohm effect, persistent current, and magnetization in semiconductor nanorings of type I and II.* Phys. Rev. B, 2006. **74**: p. 115416.
16. Timm, R., et al., *Quantum ring formation and antimony segregation in GaSb/GaAs nanostructures.* J. Vac. Sci. Technol. B, 2008. **26**: p. 1492.
17. Lin, W.-H., et al., *The formation mechanisms and optical characteristics of GaSb quantum rings.* J. Appl. Phys., 2013. **114**: p. 053509.
18. Kobayashi, S., et al., *Self-assembled growth of GaSb type II quantum ring structures.* Jpn. J. Appl. Phys., 2004. **43**: p. L662.
19. Odashima, S., et al., *GaSb quantum rings grown by metal organic molecular beam epitaxy.* J. Cryst. Growth, 2011. **323**: p. 233.
20. Kawazu, T., et al., *Growth of GaSb dots on GaAs(100) by droplet epitaxy.* Phys. Status Solidi B, 2009. **246**: p. 733.
21. Kawazu, T., et al., *Two different growth modes of GaSb dots on GaAs(100) by droplet epitaxy.* J. Cryst. Growth, 2009. **311**: p. 2255.
22. Liang, B., et al., *GaSb/GaAs type-II quantum dots grown by droplet epitaxy.* Nanotechnology, 2009. **20**: p. 455604.
23. Kawazu, T., et al., *Effects of antimony flux on morphology and photoluminescence spectra of GaSb quantum dots formed on GaAs by droplet epitaxy.* J. Nonlinear Opt. Phys. Mater., 2010. **19**: p. 819.
24. DeJarld, M., et al., *Mechanisms of ring and island formation in lattice mismatched droplet epitaxy.* Appl. Phys. Lett., 2013. **102**: p. 133107.
25. Barth, J.V., Costantini, G., and Kern, K., *Engineering atomic and molecular nanostructures at surfaces.* Nature, 2005. **437**: p. 671.
26. Venables, J.A., et al., *Rate and diffusion analyses of surface processes.* J. Phys. Chem. Solids, 1994. **55**: p. 955.
27. Venables, J.A., Spiller, G.D.T., and Hanbücken, M., *Nucleation and growth of thin films.* Rep. Prog. Phys., 1984. **47**: p. 399.
28. Ratch, C., and Venables, J.A., *Nucleation theory and the early stages of thin film growth.* J. Vac. Sci. Technol. A, 2003. **21**: p. S96.

29. Bauer, E., *Phänomenologische Theorie der Kristallabscheidung an Oberflächen. I.* Z. Krist., 1958. **110**: p. 372.
30. Chikyow, T., and Koguchi, N., *MBE growth method for pyramid-shaped GaAs micro crystals on ZnSe(001) surface using Ga droplets.* Jpn. J. Appl. Phys., 1990. **29**: p. L2093.
31. Lee, C.-D., et al., *Fabrication of self-assembled quantum dots in lattice-matched GaAs/AlGaAs system.* J. Korean Phys. Soc., 1998. **33**: p. S262.
32. Mano, T., and Koguchi, N., *Nanometer-scale GaAs ringstructure grown by droplet epitaxy.* J. Cryst. Growth, 2005. **278**: p. 108.
33. Somaschini, C., et al., *Fabrication of multiple concentric nanoring structures.* Nano Lett., 2009. **9**: p. 3419.
34. Somaschini, C., et al., *Outer zone morphology in GaAs ring/disk nanostructures by droplet epitaxy.* J. Cryst. Growth, 2011. **323**: p. 279.
35. Sanguinetti, S., et al., *Complex nanostructures by pulsed droplet epitaxy.* Nanomater. Nanotechnol., 2011. **1**: p. 14.
36. Wang, Z.M., et al., *Self-assembly of GaAs holed nanostructures by droplet epitaxy.* Phys. Status Solidi A, 2005. **202**: p. R85.
37. Jevasuwan, W., et al., *InP ring-shaped quantum-dot molecules grown by droplet molecular beam epitaxy.* J. Cryst. Growth, 2011. **323**: p. 275.
38. Ohta, K., Kojima, T., and Nakagawa, T., *Anisotropic surface migration of Ga atoms on GaAs (001).* J. Cryst. Growth, 1989. **95**: p. 71.
39. Lee, J.H., et al., *Various quantum- and nano-structures by III-V droplet epitaxy on GaAs substrates.* Nanoscale Res. Lett., 2010. **5**: p. 308.
40. Kapon, E., *Quantum wire lasers.* Proc. IEEE, 1992. **80**: p. 398.
41. Warburton, R.J., et al., *Optical emission from a charge-tunable quantum ring.* Nature, 2000. **405**: p. 926.
42. Andrews, A.M., Schramböck, M., and Strasser, G., *InAs Quantum Dots on $Al_xGa_{1-x}As$ Surfaces and in an $Al_xGa_{1-x}As$ Matrix*, in *Handbook of Self Assembled Semiconductor Nanostructures for Novel Devices in Photonics and Electronics*, M. Henini, Editor. 2008, Elsevier: Oxford. p. 62-83.
43. Varshni, Y.P., *Temperature dependence of the energy gap in semiconductors.* Physica, 1967. **34**: p. 149.

44. Yu, P.W., *Deep-center photoluminescence in undoped semi-insulating GaAs: 0.68 eV band due to the main deep donor.* Solid State Commun., 1982. **43**: p. 953.

45. Takojima, N., et al., *Emission mechanism of blue and green bands in ultrathin ZnSe-ZnTe superlattices.* J. Cryst. Growth, 1996. **159**: p. 489.

46. Zhang, Y.C., et al., *Thermal redistribution of photocarriers between bimodal quantum dots.* J. Appl. Phys., 2001. **90**: p. 1973.

47. Zhou, X.L., et al., *Thermal carrier processes in bimodal-sized quantum dots with different lateral coupling strength.* Appl. Phys. Lett., 2011. **99**: p. 031903.

48. Muñoz-Matutano, G., et al., *Size dependent carrier thermal escape and transfer in bimodally distributed self assembled InAs/GaAs quantum dots.* J. Appl. Phys., 2012. **111**: p. 123522.

49. Cohen, E., Street, R.A., and Muranevich, A., *Bound excitons and resonant Raman scattering in* $Cd_xZn_{1-x}Te$ $(0.9 \leq x \leq 1)$. Phys. Rev. B, 1983. **28**: p. 7115.

50. Seravalli, L., et al., *Quantum dot strain engineering of InAs/InGaAs nanostructures.* J. Appl. Phys., 2007. **101**: p. 024313.

51. Mazzucato, S., et al., *Defect passivation in strain engineered InAs/(InGa)As quantum dots.* Mater. Sci. Eng. C, 2005. **25**: p. 830.

52. Mohanta, A., et al., *Time-integrated photoluminescence and pump-probe reflection spectroscopy of Si doped InN thin films.* J. Appl. Phys., 2014. **115**: p. 044906.

53. Tulkki, J., and Heinämäki, A., *Confinement effect in a quantum well dot induced by an InP stressor.* Phys. Rev. B, 1995. **52**: p. 8239.

54. Schmidt, T., Lischka, K., and Zulehner, W., *Excitation-power dependence of the near-band-edge photoluminescence of semiconductors.* Phys. Rev. B, 1992. **45**: p. 8989.

55. Luckert, F., et al., *Excitation power and temperature dependence of excitons in* $CuInSe_2$. J. Appl. Phys., 2012. **111**: p. 093507.

56. Jo, M., Mano, T., and Sakoda, K., *Formation of highly anisotropic GaAs quantum dots on GaAs(001) substrates.* J. Phys.: Conf. Ser., 2010. **245**: p. 012075.

57. Sun, C.-K., et al., *Optical investigations of the dynamic behavior of GaSb/GaAs quantum dots.* Appl. Phys. Lett., 1996. **68**: p. 1543.

58. Ayers, J.E., *Heteroepitxy of Semiconductors: Theory, Growth, and Characterization*. 2007, Florida: CRC Press.

59. Thibado, P.M., et al., *Evolution of GaSb epitaxy on GaAs(001)-c(4×4).* J. Vac. Sci. Technol. A, 1996. **14**: p. 885.

60. Kinder, B.M., and Goldys, E.M., *Microstructural evolution of GaSb self-assembled islands grown by metalorganic chemical vapor deposition.* Appl. Phys. Lett., 1998. **73**: p. 1233.

61. Wang, T., and Forchel, A., *Growth of self-organized GaSb islands on a GaAs surface by molecular beam epitaxy.* J. Appl. Phys., 1999. **85**: p. 2591.

62. Müller-Kirsch, L., et al., *Formation of GaSb/GaAs quantum dots in MOCVD growth.* Physica E, 2002. **13**: p. 1181.

63. Müller-Kirsch, L., et al., *Temporal evolution of GaSb/GaAs quantum dot formation.* Appl. Phys. Lett., 2001. **79**: p. 1027.

64. Silveira, J.P., García, J.M., and Briones, F., *Surface stress effects during MBE growth of III-V semiconductor nanostructures.* J. Cryst. Growth, 2001. **227**: p. 995.

65. Pitts, O.J., et al., *Ultrathin type-II GaSb/GaAs quantum wells grown by OMVPE.* J. Cryst. Growth, 2004. **269**: p. 187.

66. Heitz, R., et al., *Observation of reentrant 2D to 3D morphology transition in highly strained epitaxy: InAs on GaAs.* Phys. Rev. Lett., 1997. **78**: p. 4071.

67. Flebbe, O., et al, *Atomic structure of stacked InAs quantum dots grown by metal-organic chemical vapor deposition.* J. Vac. Sci. Technol. B, 1999. **17**: p. 1639.

68. Prohl, C., et al., *Atomic structure and strain of the InAs wetting layer growing on GaAs(001)-c(4×4).* J. Vac. Sci. Technol. B, 2010. **28**: p. C5E13.

69. Márquez, J., Geelhaar, L., and Jacobi, K., *Atomically resolved structure of InAs quantum dots.* Appl. Phys. Lett., 2001. **78**: p. 2309.

70. Eisele, H., and Jacobi, K., *Erratum: "Atomically resolved structure of InAs quantum dots" [Appl. Phys. Lett. 78, 2309 (2001)].* Appl. Phys. Lett., 2007. **90**: p. 129902.

71. Eisele, H., and Dähne, M., *Critical thickness of the 2-dimensional to 3-dimensional transition in GaSb/GaAs(001) quantum dot growth.* J. Cryst. Growth, 2012. **338**: p. 103.
72. Müller-Kirsch, L., et al., *Thin GaSb insertions and quantum dot formation in GaAs by MOCVD.* J. Cryst. Growth, 2000. **221**: p. 611.
73. Ledentsov, N.N., et al., *Radiative states in type-II GaSb/GaAs quantum wells.* Phys. Rev. B, 1995. **52**: p. 14058.
74. Wang, Y.Q., et al., *Thermodynamic analysis of anion exchange during heteroepitaxy.* J. Cryst. Growth, 2002. **242**: p. 5.
75. Wang, M.W., et al., *Study of interface asymmetry in InAs-GaSb heterojunctions.* J. Vac. Sci. Technol. B, 1995. **13**: p. 1689.
76. Ulloa, J.M., et al., *Suppression of InAs/GaAs quantum dot decomposition by the incorporation of a GaAsSb capping layer.* Appl. Phys. Lett., 2007. **90**: p. 213105.
77. Nosho, B.Z., et al., *Effects of* As_2 *versus* As_4 *on InAs/GaSb heterostructures: As-for-Sb exchange and film stability.* J. Vac. Sci. Technol. B, 2001. **19**: p. 1626.
78. Brown, T., Brown, A., and May G., *Anion exchange at the interfaces of mixed anion III-V heterostructures grown by molecular beam epitaxy.* J. Vac. Sci. Technol. B, 2002. **20**: p. 1771.
79. Wang, M.W., et al., *X-ray photoelectron spectroscopy investigation of the mixed anion GaSb/InAs heterointerface.* J. Vac. Sci. Technol. B, 1993. **11**: p. 1418.
80. Tseng, C.-C., et al., *Influence of As on the morphologies and optical characteristics of GaSb/GaAs quantum dots.* IEEE J. Quantum Elect., 2011. **47**: p. 335.
81. Gérard, J.M., et al., *Optical investigation of the self-organized growth of InAs/GaAs quantum boxes.* J. Cryst. Growth, 1995. **150**: p. 351.
82. Luo, X.D., et al., *Abnormal effect of growth interruption on GaSb quantum dots formation grown by molecular beam epitaxy.* J. Cryst. Growth, 2003. **247**: p. 99.

83. Van de Walle, C.G., *Band lineups and deformation potentials in the model-solid theory.* Phys. Rev. B, 1989. **39**: p. 1871.
84. Dekel, E., et al., *Cascade evolution and radiative recombination of quantum dot multiexcitons studied by time-resolved spectroscopy.* Phys. Rev. B, 2000. **62**: p. 11038.
85. Jo, M., et al., *Origin of the blueshift of photoluminescence in a type-II heterostructure.* Nanoscale Res. Lett., 2012. **7**: p. 654.
86. Hodgson, P.D., et al., *Blueshifts of the emission energy in type-II quantum dot and quantum ring nanostructures.* J. Appl. Phys., 2013. **114**: p. 073519.
87. Yin, H., Li, G., and Jiang, C., *Temperature effect of activation energy for GaSb quantum dots using variable temperature photoluminescence.* J. Nanosci. Nanotechnol., 2013. **13**: p. 1022.
88. Hodgson, P.D., et al., *Hole migration and optically induced charge depletion in GaSb/GaAs wetting layers and quantum rings.* Phys. Rev. B, 2013. **88**: p. 155322.
89. Farrell, H.H., and Palmstrøm, C.J., *Reflection high energy electron diffraction characteristic absences in GaAs(100) (2×4)-As: A tool for determining the surface stoichiometry.* J. Vac. Sci. Technol. B, 1990. **8**: p. 903.
90. Yamaguchi, K., Tsukamoto, S., and Matsuda, K., *GaSb/GaAs Quantum Nanostructures by Molecular Beam Epitaxy*, in *Handbook of Self Assembled Semiconductor Nanostructures for Novel Devices in Photonics and Electronics*, M. Henini, Editor. 2008, Elsevier: Oxford. p. 271-292.
91. Nemcsics, Á., et al., *The RHEED tracking of the droplet epitaxial grown quantum dot and ring structures.* Mater. Sci. Eng. B, 2009. **165**: p. 118.
92. Wang, Z.M., et al., *Nanoholes fabricated by self-assembled gallium nanodrill on GaAs(100).* Appl. Phys. Lett., 2007. **90**: p. 113120.
93. Li, X.L., and Yang, G.W., *On the physical understanding of quantum rings self-assembly upon droplet epitaxy.* J. Appl. Phys., 2009. **105**: p. 103507.
94. Li, X.L., Wang, C.X., and Yang, G.W., *Thermodynamic theory of growth of nanostructures.* Prog. Mater. Sci., 2014. **64**: p. 121.
95. Nemcsics, Á., *Formation kinetics of the self-organized III-V-based nanostructures grown by droplet epitaxy.* Acta Polytech. Hung., 2011. **8**: p. 5.

96. Kamarudin, M.A., et al., *GaSb quantum dot morphology for different growth temperatures and the dissolution effect of the GaAs capping layer.* J. Phys. D: Appl. Phys., 2010. **43**: p. 065402.
97. Mano, T., et al., *Self-assembly of concentric quantum double rings.* Nano Lett., 2005. **5**: p. 425.
98. Moon, P., et al., *Strained Quantum Rings*, in *Physics of Quantum Rings*, V.M. Fomin, Editor. 2014, Springer: New York. p. 331-352.
99. Sanguinetti, S., et al., *Temperature dependence of the photoluminescence of InGaAs/GaAs quantum dot structures without wetting layer.* Appl. Phys. Lett., 2002. **81**: p. 3067.
100. Young, R.J., et al., *Optical observation of single-carrier charging in type-II quantum ring ensembles.* Appl. Phys. Lett., 2012. **100**: p. 082104.
101. Gerardot, B.D., et al., *Optical pumping of a single hole spin in a quantum dot.* Nature, 2008. **451**: p. 441.
102. Syperek, M., et al., *Spin coherence of holes in GaAs/(Al,Ga)As quantum wells.* Phys. Rev. Lett., 2007. **99**: p. 187401.

APPENDIX

List of Publications

Publications related to the dissertation

1. **M. Kunrugsa**, P. Prongjit, K. Khoklang, S. Panyakeow, S. Ratanathammaphan, *Evolution of Ga droplets into GaSb quantum rings*. Proceedings of the 2014 International Conference on Nanoscience and Nanotechnology, 2014. pp. 35-38.
2. **M. Kunrugsa**, S. Kiravittaya, S. Panyakeow, S. Ratanathammaphan, *Effect of Ga deposition rates on GaSb nanostructures grown by droplet epitaxy*. J. Cryst. Growth, 2014. **402**: p. 285.
3. **M. Kunrugsa**, S. Panyakeow, S. Ratanathammaphan, *GaSb/GaAs quantum-ring-with-dot structures grown by droplet epitaxy*. J. Cryst. Growth, 2015. **416**: p. 73.
4. **M. Kunrugsa**, K.H.P. Tung, A.J. Danner, S. Panyakeow, S. Ratanathammaphan, *Fabrication of GaSb quantum rings on GaAs (001) by droplet epitaxy*. J. Cryst. Growth, 2015. (In press)
5. **M. Kunrugsa**, S. Panyakeow, S. Ratanathammaphan, *Type-II GaSb/GaAs nanostructures grown by droplet epitaxy with various Ga amounts*. Adv. Mater. Res., 2015. (Submitted)

Other publications

1. **M. Kunrugsa**, P. Prongjit, P. Boonpeng S. Panyakeow, S. Ratanathammaphan, *Influence of growth temperature on InAs quantum dots*. Proceedings of the 2013 International Electrical Engineering Congress, 2013. pp. 181-184.
2. S. Kiravittaya, **M. Kunrugsa**, S. Thainoi, S. Ratanathammaphan, S. Panyakeow, *Electronic structure calculation of GaSb/GaAs quantum dot*. Proceedings of the 2014 International Electrical Engineering Congress, 2014. pp. 1-4.
3. **M. Kunrugsa**, S. Kiravittaya, S. Sopitpan, S. Ratanathammaphan, S. Panyskeow, *Molecular beam epitaxial growth of GaSb/GaAs quantum dots on Ge substrates*. J. Cryst. Growth, 2014. **401**: p. 441.
4. K. Khoklang, S. Kiravittaya, **M. Kunrugsa**, P. Prongjit, S. Thainoi, S. Ratanathammaphan, S. Panyakeow, *Molecular beam epitaxial growth of GaSb quantum dots on (001) GaAs substrate with InGaAs insertion layer*. J. Cryst. Growth, 2015. (In press)

5. N. Prapasawad, **M. Kunrugsa**, P. Prongjit, S. Panyakeow, S. Ratanathammaphan, *The fabrication of lateral InAs quantum dot molecules on InGaAs nanomounds by molecular beam epitaxy (MBE)*. Adv. Mater. Res., 2015. (Submitted)

List of Presentations

1. **M. Kunrugsa**, P. Prongjit, P. Boonpeng S. Panyakeow, S. Ratanathammaphan, *Influence of growth temperature on InAs quantum dots*. 2013 International Electrical Engineering Congress, Chiang Mai, Thailand, March 13-15, 2013. (Oral)
2. **M. Kunrugsa**, P. Prongjit, N. Pankaow, S. Panyakeow, S. Ratanathammaphan, *Effects of Sb_4 soaking time and low V/III ratio on GaSb/GaAs quantum dots*. 7th International Conference on Materials for Advanced Technologies, Suntec City, Singapore, June 30-July 5, 2013. (Poster)
3. **M. Kunrugsa**, P. Prongjit, N. Pankaow, S. Panyakeow, S. Ratanathammaphan, *A hybrid growth of self-assembled InAs/GaAs quantum dots*. 7th International Conference on Materials for Advanced Technologies, Suntec City, Singapore, June 30-July 5, 2013. (Poster)
4. **M. Kunrugsa**, P. Prongjit, K. Khoklang, S. Panyakeow, S. Ratanathammaphan, *Evolution of Ga droplets into GaSb quantum rings*. 2014 International Conference on Nanoscience and Nanotechnology, Adelaide, Australia, February 2-6, 2014. (Poster)
5. **M. Kunrugsa**, K.H.P. Tung, A.J. Danner, S. Panyakeow, S. Ratanathammaphan, *Fabrication of GaSb quantum rings on GaAs (001) by droplet epitaxy*. 18th International Conference on Molecular Beam Epitaxy, Arizona, United States of America, September 7-12, 2014. (Poster)
6. **M. Kunrugsa**, S. Panyakeow, S. Ratanathammaphan, *Type-II GaSb/GaAs nanostructures grown by droplet epitaxy with various Ga amounts*. 4th Thailand International Nanotechnology Conference, Pathumthani, Thailand, November 26-28, 2014. (Poster)
7. **M. Kunrugsa**, S. Panyakeow, S. Ratanathammaphan, *Gallium antimonide ring-with-dot structures grown by droplet epitaxy*. 18th European Molecular Beam Epitaxy Workshop, Canazei, Italy, March 15-18, 2015. (Poster)
8. **M. Kunrugsa**, S. Panyakeow, S. Ratanathammaphan, *Effect of growth parameters on GaSb/GaAs nanostructures grown by droplet epitaxy*. RGJ-Ph.D. Congress XVI, Chonburi, Thailand, June 11-13, 2015. (Poster)

VITA

Maetee Kunrugsa was born in Bangkok, Thailand on May 2, 1989. He graduated from Ratwinit Bangkaeo School in 2006. At that time, he was granted the Royal Scholarships as a student with outstanding academic performance, and selected to join the Mathematical Olympiad Training Program by the Promotion of Academic Olympiad and Development of Science Education Foundation (POSN). He entered Chulalongkorn University in May 2007, and earned the Bachelor of Engineering (2nd Class Honours) in the field of Electrical Engineering in May 2011. Immediately, he continued his education in the Doctor of Philosophy Program in Electrical Engineering at Semiconductor Device Research Laboratory, Department of Electrical Engineering, Chulalongkorn University. He has been financially supported by Thailand Research Fund through the Royal Golden Jubilee Ph.D. Program (Grant no. PHD/0026/2554) since June 2012. His research interests cover the growth and characterization of self-assembled III-V semiconductor nanostructures, including their applications.